

NONLINEAR OPTICAL PROPERTIES OF CdTe  
AND LASER INDUCED GRATING IN  
Eu<sup>3+</sup> -DOPED SILICATE GLASSES

By

ABDULLATIF Y. HAMAD

Bachelor of Science

Oklahoma State University

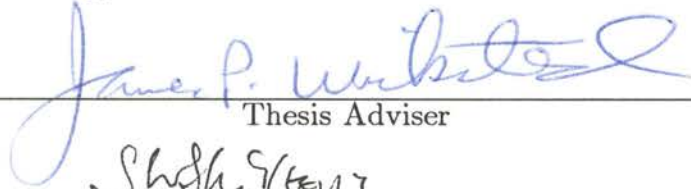
Stillwater, Oklahoma

1990

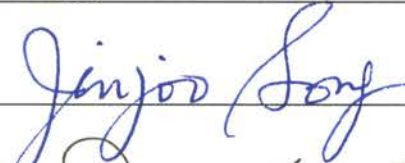
Submitted to the Faculty of the  
Graduate College of the  
Oklahoma State University  
in Partial fulfillment of  
the requirements for  
the Degree of  
DOCTOR OF PHILOSOPHY  
July, 1996

NONLINEAR OPTICAL PROPERTIES OF CdTe  
AND LASER INDUCED GRATING IN  
Eu<sup>3+</sup> -DOPED SILICATE GLASSES

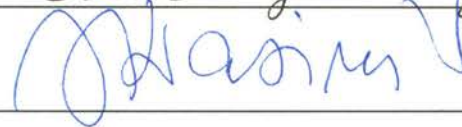
Thesis Approved:

  
\_\_\_\_\_  
Thesis Adviser

  
\_\_\_\_\_

  
\_\_\_\_\_

  
\_\_\_\_\_

  
\_\_\_\_\_

  
\_\_\_\_\_

Dean of the Graduate College

بِسْمِ اللَّهِ الرَّحْمَنِ الرَّحِيمِ

“Experience indicates that whoever writes a book today will say tomorrow:

Changing this page would make the book better; inserting this section would result in an improvement; moving this paragraph would be more effective; and dropping this line would enhance the quality of this piece of writing.

This is an evidence that human beings are not perfect and learning is an unending process.”

Al’Imad Al-Asfahani.

English translation (not literal)  
from the original Arabic saying.

Dedicated to My Parents

## ACKNOWLEDGMENTS

Completion of this dissertation was made possible by the contributing efforts of several people to whom I am deeply indebted. I wish to express my sincere appreciation to my thesis adviser Dr. J. P. Wicksted for giving me the opportunity to work with him. I am very grateful to him for his invaluable guidance, inspiration, friendship, and support throughout the Ph.D. program. I also would like to thank Carol Wicksted her continuous help and support.

I would like to sincerely thank my other thesis committee members Dr. S. McKeever, Dr. J. J. Song, Dr. D. Bandy, and Dr. J. Krasinski. I am very grateful to Dr. G. Dixon for many fruitful discussions. I also express my special appreciation to my friend, classmate, and lab partner S. Mian for many helpful discussions in research and course work.

I would like to thank Dr. J. J. Song and Center for Laser Research for providing us with equipments and space to do the four wave mixing experiments. I wish to thank Mr. G. Cantwell of Eagle-Picher Industries for providing the CdTe samples. The CdTe project was initially supported by the Defense Advanced research projects Agency Contract No. MDA972-89-K-0001 and the Oklahoma Center for the Advancement of Science and Technology Contract No. 4429. The  $\text{Eu}^{3+}$ -doped glasses project was supported by Radiation Monitoring Devices through a phase II USAF/SBIR.

I would like to give my special appreciation and gratitude to my parents. I thank them for the love and support they have given me over the years. I will

be always thankful for the values that they have instilled in me. I will always remember where home is, no matter where I am. I am also indebted to my brothers and sisters for their endless support, moral encouragement and understanding.

I would like to thank my wife, Tharwat, for being my best friend for the last 5 years. My daughter Bayan and my son Hamzah have brought and continue to bring great joy and happiness into my life. I greatly appreciate the strength, love and understanding (for the long hours spent in the lab and so little time spend with them) which they have given to me. I will try my best to make up for the lost time in the future.

Finally and most importantly, I am very grateful and thankful to Allah for his blessing and guidance. I pray to him that I may use my knowledge and education to benefit humanity.

## TABLE OF CONTENTS

Chapter	Page
I. INTRODUCTION .....	1
II. SPATIAL AND TEMPORAL BEAM RESHAPING EFFECTS USING BULK CdTe.....	5
1. Introduction .....	5
2. Experiment.....	7
3. Theoretical Model .....	12
(a) Propagation of the Beam Inside the Sample.....	12
(b) Propagation of the Beam Outside the Sample.....	17
4. Results and Discussion.....	18
5. Conclusion.....	31
III. TWO-PHOTON INDUCED OPTICAL SWITCHING USING A CdTe ETALON.....	34
1. Introduction .....	34
2. Experimental.....	35
3. Theory.....	38
4. Results .....	42
5. Discussion .....	50
6. Conclusion.....	55
IV. LASER INDUCED TRANSIENT AND PERMANENT GRATING IN Eu <sup>3+</sup> -DOPED SILICATE GLASSES .....	56
1. Introduction .....	56
2. Experimental Setup.....	57
3. Theory.....	60
(a) Plane-Wave Approximation.....	60
(b) Gaussian Beams .....	62
4. Results .....	71
(a) Results of the Theoretical Model.....	71
(b) Experimental Results .....	76
(i) The Effect of the Dual-Alkaline Ions.....	84
(ii) Sodium Enriched Eu <sup>3+</sup> -Doped Silicate Glasses.....	102
(iii) The dependence of the Grating on the write-beam wavelength.....	102
5. Discussion .....	109
(a) Effect of the Second Alkaline Modifier .....	112

Chapter	Page
(b) Sodium Enriched Samples .....	115
(c) Transient Grating .....	116
(d) Writing and Erasing the Grating .....	117
(e) Scattered Signal Saturation .....	118
V. SUMMARY AND FUTURE WORK.....	120
BIBLIOGRAPHY.....	123
APPENDIXES.....	128
A. DERIVATION OF EQUATION (II.1) .....	129
B. DERIVATION OF $I_{cr}$ .....	132
C. REFRACTIVE INDEX MEASUREMENTS USING A CCD .....	134
1. Introduction .....	134
2. Procedure .....	134
3. Discussion.....	136
4. Conclusion.....	137
D. PROGRAM FOR THE THEORY IN CHAPTER II .....	138
E. PROGRAM FOR THE THEORY IN CHAPTER III .....	147
F. PROGRAM FOR THE THEORY IN CHAPTER IV .....	153



## LIST OF TABLES

Table	Page
II.1. Characteristics of the CdTe samples.....	12
II.2. Experimental and theoretical values of the two-photon absorption coefficient for CdTe.....	29
IV.1. Experimental result for B16CS, B16SQ, B24CS, and B24CS using $P_w=28$ mW and $\theta_w=1.9^\circ$ .....	73
IV.2. Identity and Composition of the $\text{Eu}^{3+}$ -doped Silicate Glasses. All Samples contain 2.5 mol% $\text{Eu}_2\text{O}_3$ .....	80
IV.3. Some of the linear parameters for the samples used in the study. $L_S$ is the sample thickness, $n_w$ ( $n_r$ ) is the index of refraction, and $\alpha_w$ ( $\alpha_r$ ) is the linear absorption coefficient .....	80
IV.4. Calculated values of $(\eta/\Delta n^2)$ for $\lambda_e=465.8$ nm and $\lambda_p=632.8$ nm .....	88
IV.5. The maximum scattering efficiency and $\Delta n$ for the 16-family .....	95
IV.6. The transient scattering efficiency and $\Delta n$ for the 16-family .....	96
IV.7. The maximum scattering efficiency and $\Delta n$ for the 22-family .....	100
IV.8. The transient scattering efficiency and $\Delta n$ for the 22-family .....	101
IV.9. The maximum scattering efficiency and $\Delta n$ for B29 and B30.....	105
IV.10. Experimental result for B28 using $P_w=44$ mW and $\theta_w=2.5^\circ$ .....	108

## LIST OF FIGURES

Figure	Page
II.1. Experimental arrangement for measuring the transmitted (a) spatial profile and (b) temporal profile.....	8
II.2. The input temporal profile. The hollow circles are the experimental data and the solid line is the fit of Eq. (II.6) with $t_o=5$ ns, $t_1=8$ ns and $n_g=2$ .....	10
II.3. The input spatial profile. The hollow circles are the experimental data and the solid line is the fit of a Gaussian with $w_o=215$ $\mu$ m.....	11
II.4. The experimental transmitted spatial profiles, through a 1.36 mm AR coated sample, measured at 6 cm behind the sample are represented by the hollow circles.....	20
II.5. The experimental transmitted beam profiles, through a 1.36 mm AR coated sample, detected at 10 cm behind the sample are represented by the hollow circles.....	21
II.6. The experimental results of the transmitted temporal profiles using a 1.36 mm AR coated sample and input irradiance 18.4 MW/cm <sup>2</sup> are represented by the hollow circles.....	22
II.7. The experimental results of the transmitted temporal profiles using a 1.36 mm AR coated sample and input irradiance 32.2 MW/cm <sup>2</sup> are represented by the hollow circles.....	23
II.8. The temporal profiles of different points within the laser beam.....	25
II.9. The experimental results of the transmitted temporal profiles using a 1.5 mm 50% reflectivity wedge sample and input irradiance 10.5 MW/cm <sup>2</sup> are represented by the hollow circles. ....	26
II.10. (a) On-axis photogenerated carriers density at different point within the sample.....	32
III.1. Experimental setup for observing optical switching .....	36
III.2. Experimental and theoretical results for $I_o=14.8$ MW/cm <sup>2</sup> , $\phi_o=-0.1\pi$ and $F_F=1$ . .....	45

Figure	page
III.3. Experimental and theoretical results for $I_o=17.7$ MW/cm <sup>2</sup> , $\phi_o$ = $-0.1\pi$ and $F_F=1$ . .....	46
III.4. Experimental and theoretical results for $I_o=12$ MW/cm <sup>2</sup> , $\phi_o=$ $0.18\pi$ and $F_F=3$ . .....	48
III.5. Experimental and theoretical results for $I_o=15.4$ MW/cm <sup>2</sup> , $\phi_o$ = $0.18\pi$ and $F_F=3$ . .....	49
III.6. Experimental and theoretical results for $I_o=11.4$ MW/cm <sup>2</sup> , $\phi_o$ = $-0.24\pi$ and $F_F=2$ . .....	51
III.7. Experimental and theoretical results for $I_o=17.7$ MW/cm <sup>2</sup> , $\phi_o$ = $-0.24\pi$ and $F_F=2$ . .....	52
IV.1. The FWM experimental setup. ....	58
IV.2. The diagram shows two intersecting Gaussian beams to create a volume grating pattern. ....	62
IV.3. The interference intensity pattern of the two-crossed beams at different positions along the $z$ -direction. ....	65
IV.4. Theoretical ( lines) and experimental (dark circles) scattered efficiencies for B18 and B26 using different crossing angles. ....	74
IV.5. Scattered efficiency as a function of sample thickness. ....	75
IV.6. Contour plots of the diffracted beam for $w_w=w_r=0.01$ cm, $\lambda_w$ = $465.8$ nm, $n_w=1.57$ , $L_G=9$ mm, and $\theta_w=2^\circ$ (a) $L_S=1$ mm, ( $L_S \ll L_G$ ) $n_r=1.55$ , and $\lambda_r=632.8$ nm. ....	77
IV.7. (a) The probe beam and the diffracted beam when $L_S \ll L_G$ . ....	78
IV.8. Typical FWM scan using B29. ....	81
IV.9. The time evolution of the diffracted signal. ....	81
IV.10. Writing-erasing procedure during signal build-up using B24. ....	83
IV.11. The erasing rates during the signal build-up. ....	83
IV.12. (a) Transient signal decay with time constant 2.27 ms. (b) The fluorescence decay with time constant 2.3 ms. This data was taken using B16. ....	85

Figure	page
IV.13. This figure shows how the transient component of the signal depends on the evolution of the permanent grating (B24).....	86
IV.14. The scattered efficiency as a function of $P_w$ for different values of $\theta_w$ using B18. ....	87
IV.15. The maximum and the transient change in the index of refraction $\Delta n$ vs $P_w$ for B18.....	89
IV.16. Erasing rates using B18 for (a) different $P_w$ values and $\theta_w=2.5^\circ$ (b) different $\theta_w$ values and $P_w=44$ mW.....	90
IV.17. Signal build-up time as a function of $P_w$ for different $\theta_w$ values using B18. ....	93
IV.18. The ratio of the transient power to the maximum diffracted power vs $P_w$ at $\theta_w=2.5^\circ$ using B18. ....	93
IV.19. The change in the index of refraction $\Delta n$ for the samples of the 16-family. ....	94
IV.20. Erasing rates of the permanent grating for B16CS and B16SQ. ....	94
IV.21. (a) The diffracted efficiency as a function of $P_w$ for different $\theta_w$ values using B26. (b) The corresponding change in the index of refraction vs $P_w$ .....	97
IV.22. The change in the index of refraction for the samples of the 22-family.....	98
IV.23. The ratio of the transient power to the maximum diffracted power vs $P_w$ at $\theta_w=2.5^\circ$ using B26. ....	98
IV.24. The change in the index of refraction $\Delta n$ for the 16-family and the 22-family. ....	99
IV.25. (a) The diffracted efficiency as a function of $P_w$ for B29 and B30 at $\theta_w=1.9^\circ$ . (b) The corresponding change in the index of refraction vs $P_w$ .....	103
IV.26. (a) The decay of the permanent grating of B29 and B30 while both write-beams were blocked. (b) The decay of the permanent signal using the erasing procedure. ....	104
IV.27. The signal build-up time as a function of the write-beam wavelength using B28. ....	107

Figure	page
IV.28. The erasing rates as a function of write-beam wavelength using B28. The normalization was done by dividing the data in each curve by first data point. ....	107
IV.29. The scattered efficiency vs $\lambda_w$ for B28 using $\theta_w=2.5^\circ$ and $P_w=44$ mW .....	108
IV.30. Partial energy level diagram for $\text{Eu}^{3+}$ ion and the resonance transition to the $^5\text{D}_2$ level. ....	110
IV.31. Schematic two-dimensional representation of the structure of silicate glass including Na, Mg, and Eu ions.....	113
B.1. The maximum effective absorption coefficients due to TPA ( $\beta I_{max}$ ) and FCA ( $\sigma_{fc} N_{max}$ ) as a function of peak input irradiance. ....	133
C.1. Setup for measuring the refractive index using a CCD camera and laser beam profiler.....	135

# CHAPTER I

## INTRODUCTION

In the past decade a significant amount of research has been conducted in order to develop optical devices such as switches, and modulators which are important in optical computing and communications. Studying and understanding the nonlinear optical properties of materials is an important factor needed in the operation of such optical devices. Nonlinear effects such as laser beam reshaping, four-wave mixing (FWM), and laser-induced holographic grating are important phenomena that have potential roles in optical information processing.

The main purpose of this work was to study and understand some of the nonlinear properties of CdTe and a variety of  $\text{Eu}^{3+}$ -doped silicate glasses. Studies on CdTe were carried out via the pulse reshaping technique using nanosecond laser pulses in the near infrared. CdTe is a potential candidate to be used in optical information processes because it has large two-photon absorption and electrooptic coefficients, and is transparent in the infrared regime. It also has a relatively large nonlinear index of refraction when pumped with radiation of energy below that of the band gap (example,  $1.064 \mu\text{m}$ ). The  $\text{Eu}^{3+}$ -doped silicate glasses were investigated by using a cw FWM technique with wavelengths in the visible regime of the spectra. Doped-glasses are, generally, interesting optical materials to study because they can be made easily and inexpensively. Moreover, they can be produced with consistent properties and can be

fabricated in different shapes. These are some of the reasons that led researchers to investigate doped glasses as potential optical devices. Laser-induced gratings have been studied in different rare earth doped glasses [1-7]. However, this is the first time, to our knowledge, that the effect of dual alkaline modifiers and the role of their relative concentration on grating formation and the scattering efficiency have been investigated. Samples with single alkaline and dual alkaline ions behave differently when gratings are formed.

This work is the result of two main projects. The results of the CdTe study will be discussed in chapters II and III. Chapter IV will deal with the FWM results of the  $\text{Eu}^{3+}$ -doped silicate glasses. In chapter II the results of spatial and temporal changes in the laser profiles transmitted from CdTe crystals are presented. Reshaping effects of nanosecond pulses were theoretically and experimentally investigated using bulk CdTe. The experiments were performed using a  $1.064 \mu\text{m}$  Nd:YAG laser with pulse duration of 10 ns. We observed that the laser pulses emerging from the sample experienced temporal compression and modulation which were found to be dependent on the input irradiance, the distance from the exit surface of the sample, and the cross-sectional area detected. Self-defocusing and the formation of ring structures were also observed in the transmitted spatial profile and were found to be dependent on the input irradiance and the position of the detector from the sample. In our model we assumed that the free carriers generated by the two-photon absorption process were responsible for the induced nonlinear change in the index of refraction. As a result, the temporally and radially dependent phase shift encoded to the field that emerged from the sample was the cause of the reshaping effect. The results of our model, for both the spatial and the temporal profiles, are in

good agreement with the experimental results. Moreover, the nonlinear parameters deduced from the fitting are in good agreement with previous experimental and theoretical results.

Chapter III presents the first observation of two-photon induced optical switching using a CdTe etalon. We report the observation of optical switching, optical limiting, and pulse compression in a CdTe etalon at room temperature using 11 ns pulses at 1.064  $\mu\text{m}$  radiation. The switching was attributed to the nonlinear change in the index of refraction induced by two-photon absorption. The thermal effect was found to have a negligible contribution to the nonlinearity. The transmission of the etalon was studied as a function of its initial detuning and the input intensity. The switching times were found to be in the range of 1.5 – 3.7 ns. A theoretical model was developed in the plane-wave approximation assuming both nonlinear absorption and refraction and was found to be in good agreement with the experimental results.

In chapter IV, the results of cw FWM experiments performed on a variety of  $\text{Eu}^{3+}$ -doped silicate glasses are presented. The laser-induced grating was found to have both transient and permanent components. The permanent grating was attributed to a structural change in the local environment of the  $\text{Eu}^{3+}$  ion. The transient component of the grating was attributed to a population grating controlled by the interaction of the excited states of the  $\text{Eu}^{3+}$  ions and the environment. We developed a model from which the nonlinear change in the index of refraction can be determined using the experimental value of the scattered efficiency. This model calculates the scattered efficiency of a Gaussian probe beam from a volume grating formed by two intersecting Gaussian write beams. The effects of the alkaline cations and their relative concentration on



the scattered efficiency were investigated. The role of the excess amount of  $\text{Na}_2\text{O}$  on the scattered power was also studied. The grating formation, the scattered efficiency, the signal build-up time, and the grating erasing rate were studied as a function of write-beam power, crossing angle, and write-beam wavelength.

## CHAPTER II

### SPATIAL AND TEMPORAL BEAM RESHAPING EFFECTS

#### USING BULK CdTe

##### 1. Introduction

The study of the effects of nonlinear properties of semiconductors on transmitted laser beams is important for many applications. Optical bistability and optical limiting are two examples [8-10]. When an intense laser beam passes through a nonlinear medium it induces a nonlinear change in the index of refraction ( $\Delta n$ ). If the intensity pattern of the laser beam is not uniform (for example, the beam has temporal and spatial Gaussian profiles) then  $\Delta n$  is a function of the radial distance and time. Therefore, for an optically thin medium, a radially and temporally dependent phase shift will then be encoded to the transmitted beam. As a result, beam reshaping effects such as self-focusing or self-defocusing, ring structure formation, pulse compression and pulse modulation might occur depending on the input intensity and the sign of  $\Delta n$ . Self-defocusing in semiconductors was first observed in InSb by Weaire *et al.* [11]. They found that the effect of the sample was to encode a radially dependent phase shift to the transmitted beam. Since then many authors reported the observation of self-defocusing in different semiconductors [12-15] while optical pulse modulation has been reported by Eichler *et al.* [16,17]. Self-defocusing in CdTe

using picosecond pulses of the fundamental of the Nd:YAG laser was reported by Van Stryland *et al* [18].

In this chapter the experimental observation and the theoretical results of self-defocusing and ring structure effects using CdTe crystals at room temperature are presented. In addition, the results of laser pulse compression and modulation will be reported. The nonlinear effects are due to the photoexcited free carriers generated via two-photon absorption (TPA) of nanosecond laser pulses at  $1.064 \mu\text{m}$ . The pulse reshaping effects are investigated as a function of the input irradiance and the distance from the exit plane of the sample. Furthermore, we show that the temporal profile results are dependent on the detected cross sectional area of the transmitted light. The theory developed to explain these effects utilizes the nonlinear wave equation in one dimension along with the carrier density rate equation to propagate the laser beam inside the CdTe sample. The laser beam is then propagated to the detector using diffraction theory. We also present a comparison between the value of the nonlinear refraction coefficient (caused by the free carriers) calculated using the band-filling model developed by Auston *et al.* [19] and that obtained experimentally using our model. By fitting the theory to the experimental results we determine the values of the two-photon absorption coefficient, the free carrier absorption cross-section, and the recombination lifetime of the free carriers. Moreover, the magnitude and the sign of the nonlinear refraction coefficient ( $\sigma_r$ ) have also been determined.

## 2. Experiment

The experimental setup for observing spatial and temporal profile reshaping effects is shown in Figure II.1. We performed the experiments using the fundamental ( $\lambda=1.064 \mu\text{m}$ ) of the injection seeded Nd:YAG laser with pulse duration of about 10 ns (full width at half maximum) and a repetition rate of 10 Hz. However, most of the measurements have been obtained using single shot laser pulses. The spatial profile transmitted from the CdTe crystal was detected in the near field at two different distances (6 cm and 10 cm from the exit surface of the sample) using a charge-coupled device (CCD) camera with an active imaging area of 8.8 mm by 6.6 mm. The camera was coupled to a spiricon LBA-100 laser beam profiler. Neutral density filters in front of the camera were used to attenuate the beam intensity.

The temporal profile of both the incident and the transmitted pulses were detected by two ET2010 silicon photodetectors with rise time  $< 1$  nanosecond. Another photodetector (ET200) with rise time  $< 500$  picosecond was also used to verify the time-dependent results. The detectors were placed at 10 cm and 20 cm away from the exit plane of the sample. A pinhole of  $100 \mu\text{m}$  diameter was used directly in front of the detector to select a small area of the beam. The detector has an active area of  $0.25 \text{ mm}^2$  which guarantees that all the light transmitted from the pinhole will be detected. Both the input and the output pulses were monitored on a Tektronix 2440 digital oscilloscope for comparison. Since CdTe was known to exhibit second-harmonic generation at  $1.064 \mu\text{m}$  picosecond pulses excitation [20], an interference filter was used after the sample to pass the infrared laser light only. The energy of the input pulses was controlled by an

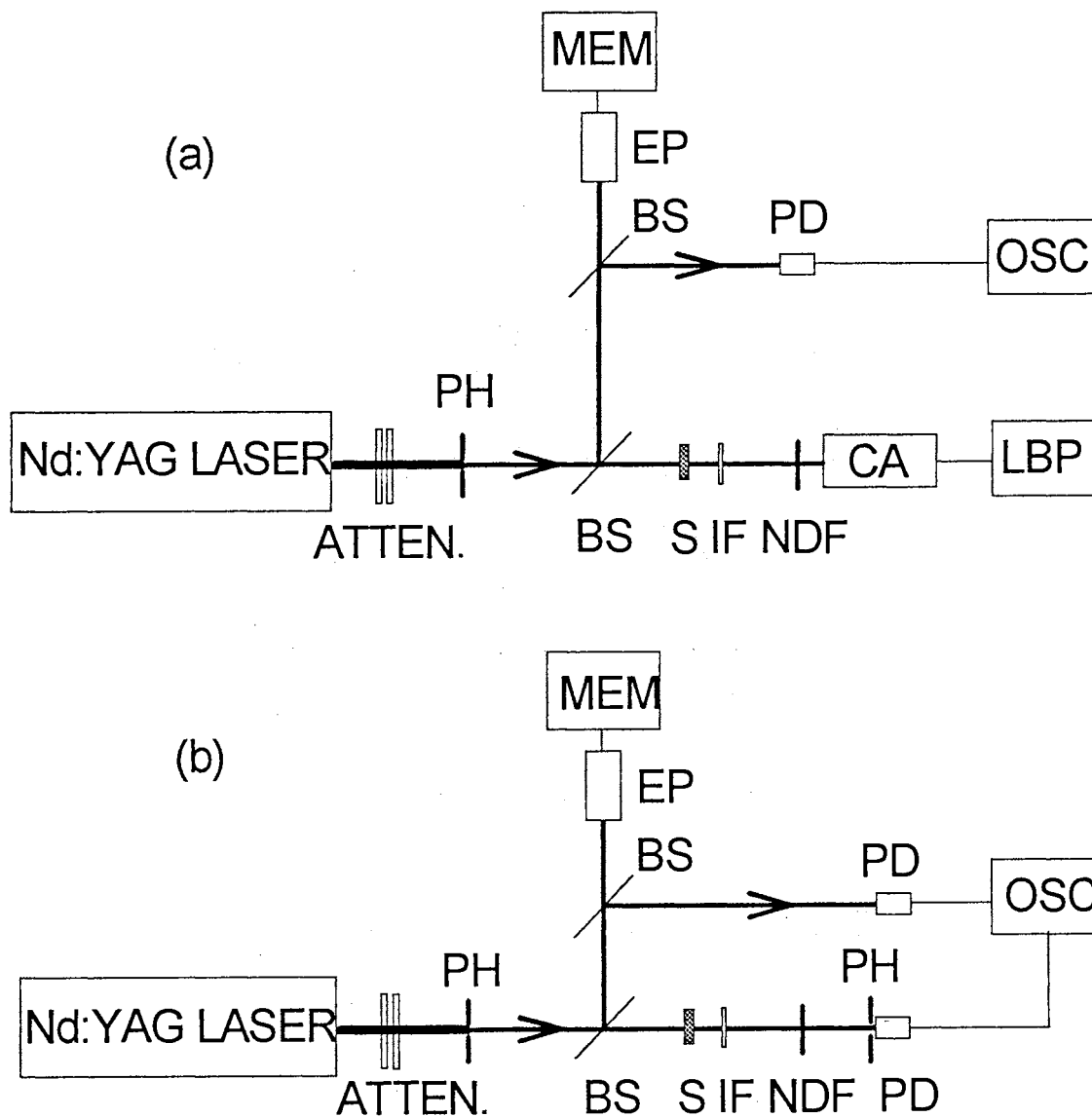


Figure II.1. Experimental arrangement for measuring the transmitted (a) spatial profile and (b) temporal profile. The symbols are : ATTEN.- attenuator, PH- pinhole, BS- beam splitter, EP- energy probe, MEM- Molelectron energy meter, PD- photodetector, S- sample, IF- interference filter, NDF- neutral density filters, OSC- oscilloscope, LBP- laser beam profiler, CA- camera.

attenuator placed before the 600  $\mu\text{m}$  pinhole and detected by a Molectron energy probe coupled to a Molectron energy meter. The total input energies used ranges between 0.01 mJ to 0.3 mJ per pulse.

The temporal profile of the laser beam is nearly Gaussian-shaped and can be fitted accurately to a superposition of Gaussians as will be shown in the theory section (see Figure II.2). In order to get a clean and a small size spatial profile (without focusing), the laser beam of 8 mm diameter was allowed to pass through a pinhole of 600  $\mu\text{m}$  diameter. As is always the case, the transmission of the 600  $\mu\text{m}$  pinhole has a diffraction pattern in which the secondary peaks are very small compared to the main peak (Airy disc) which can be fitted to a Gaussian. The main peak of the beam transmitted through the pinhole at the entrance surface of the sample has about 85% of the total energy of the incident beam. Figure II.3 shows the input spatial profile and the Gaussian fit with beam radius  $w_0=0.215$  mm ( half width at  $1/e^2$  of the maximum).

Undoped CdTe samples of both n-type and p-type with dimensions 5 mm  $\times$  5 mm  $\times$  1.36 mm with both sides polished to within 0.25 microns were used. The parallelism of these samples is better than 10 seconds of arc. The samples contained an anti-reflection coating (reflectivity at  $\lambda=1.064$   $\mu\text{m}$  is  $< 0.25\%$ ) on one side to prevent Fabry-Perot effects. The input laser beam was incident upon the uncoated surface which has a 23% reflectivity. The characteristics of these samples are listed in Table II.1. A sample of 1.5 mm thickness with 50% reflectivity on both sides and a 0.5 degree wedge angle was also used in order to observe pulse reshaping at 20 cm away from the exit surface of the crystal.

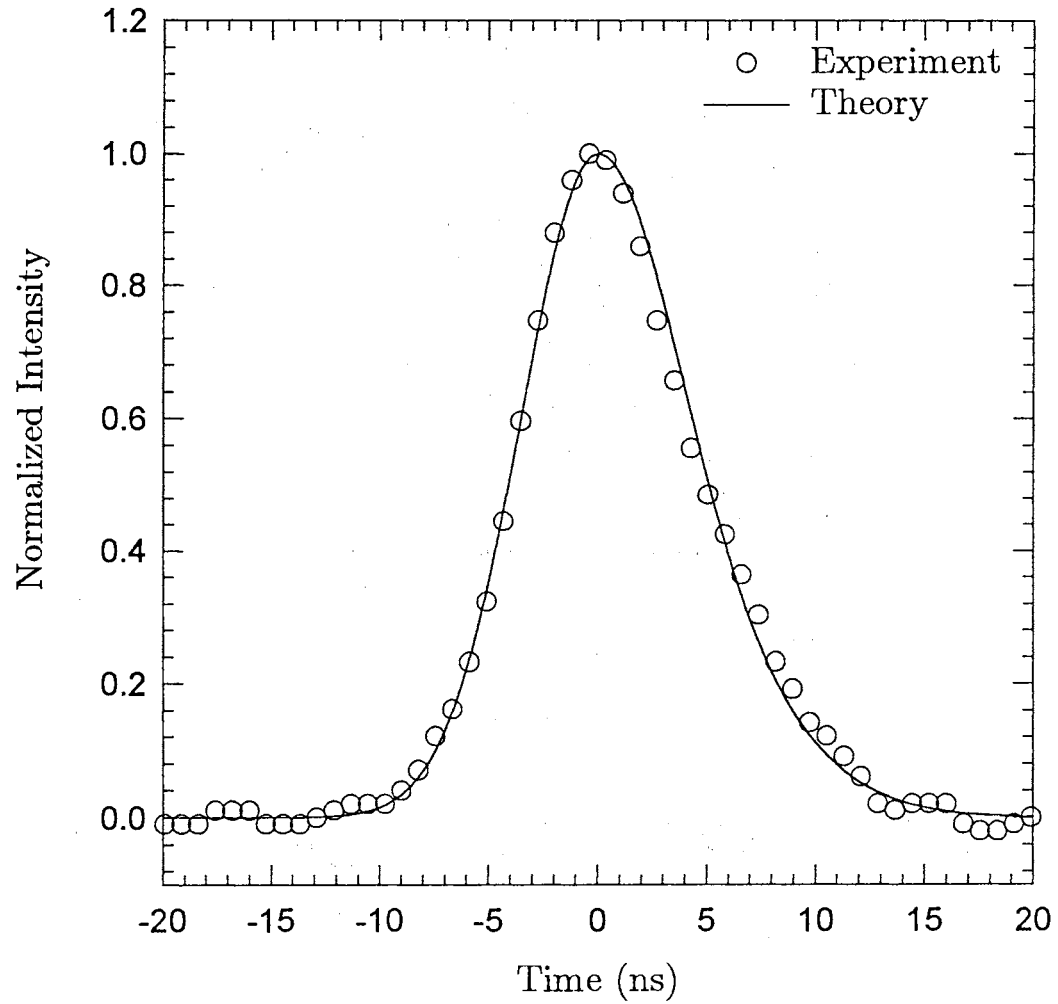


Figure II.2. The input temporal profile. The hollow circles are the experimental data and the solid line is the fit of Eq. (II.6) with  $t_0=5$  ns,  $t_1=8$  ns and  $n_g=2$

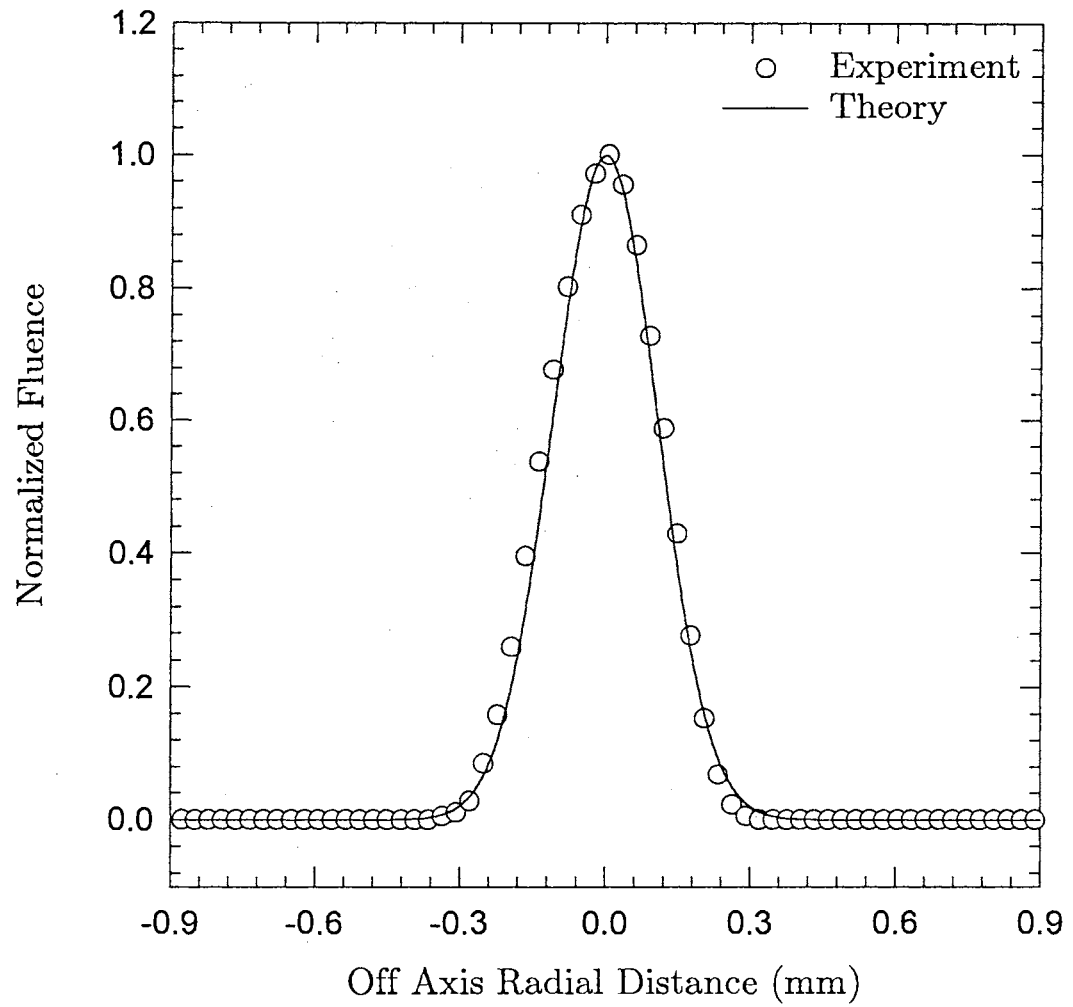


Figure II.3. The input spatial profile. The hollow circles are the experimental data and the solid line is the fit of a Gaussian with  $w_0=215 \mu\text{m}$ .



Table II.1. Characteristics of the CdTe samples.

Sample	Type	Orientation	Resistivity ( $\Omega.cm$ )	Mobility ( $cm^2/V.s$ )	Growing Method
4B	n	(111)	972	450	Bridgman
17B	p	(110)	24.1	60.8	SPVT

By using this sample, we demonstrated that pulse reshaping is dominated by the phase encoding effect and not by the Fabry-Perot effect. All samples were positioned at 14 cm after the 600  $\mu m$  pinhole.

### 3. Theoretical Model

#### (a) Propagation of the Beam Inside the Sample

In order to find the spatial and temporal profiles at a distance  $z'$  behind the sample, we need to solve the nonlinear wave equations within the sample then propagate the transmitted fields in free space using diffraction theory, in particular, the Huygens-Fresnel integral. Since the confocal parameter of the beam is larger than the thickness of the sample (external self-action) [21], we can neglect the transverse Laplacian in the wave equation for the propagation inside the nonlinear medium. Then, the nonlinear wave equation within the sample can be written as (see appendix A).

$$\frac{\partial E}{\partial z} = \left( -\frac{\sigma\mu_0 c_0}{2n_0} + i\frac{\omega|E|^2}{4n_0 c_0} \chi^{(3)} \right) E, \quad (\text{II.1})$$

where  $n_o$  is the index of refraction,  $c_o$  is the speed of light in free space,  $\mu_o$  is the permeability of free space,  $\omega$  is the optical frequency in radians/second,  $\chi^{(3)}$  is the third-order nonlinear susceptibility and  $\sigma$  is the conductivity of the medium given by

$$\sigma = n_o \sqrt{\frac{\epsilon_o}{\mu_o}} (\alpha_o + \alpha_{fc}) + i \frac{Ne^2}{\omega m_{eh}}. \quad (\text{II.2})$$

Here  $\alpha_o$  and  $\alpha_{fc}$  are the linear and free carrier absorption coefficients respectively,  $N$  is the density of the photogenerated carriers (PGC) and  $m_{eh}$  is the reduced electron-hole effective mass given by the relation  $m_{eh} = (m_e m_h / m_e + m_h)$ . Here  $m_e$  and  $m_h$  are the electron and the hole effective masses, respectively.  $\alpha_{fc}$  is equal to  $\sigma_{fc} N$ , where  $\sigma_{fc}$  is the free carrier absorption cross section which is, in general, dependent on the laser pulse duration [22].

By substituting  $E = E_o e^{i\phi}$  and  $I = (n_o c_o \epsilon_o / 2) E_o^2$  in Eq. (II.1), we can express the irradiance at distance  $z$  within the sample by:

$$\frac{\partial I(z, r, t)}{\partial z} = -\alpha_o I(z, r, t) - \beta I^2(z, r, t) - \sigma_{fc} N(z, r, t) I(z, r, t) \quad (\text{II.3})$$

and the phase by

$$\frac{\partial \phi(z, r, t)}{\partial z} = k_o \Delta n(z, r, t) = k_o [\gamma I(z, r, t) + \sigma_r N(z, r, t)], \quad (\text{II.4})$$

where  $\beta$  is the two photon absorption (TPA) coefficient given by  $\beta = (\omega / n_o^2 c_o^2 \epsilon_o) \chi_I^{(3)}$ ,  $\chi_I^{(3)}$  is the imaginary part of  $\chi^{(3)}$ ,  $k_o$  is the wave vector in free space,  $\sigma_r$  is the change in the index of refraction per unit PGC density and  $\gamma$  is the part of the nonlinear index due to the bound electrons given in terms of  $n_2$  by the relation  $\gamma (\text{cm}^2/\text{W}) = (4\pi \times 10^{-3} / c_o n_o) n_2 (\text{esu})$ .  $n_2$  is related to the real part of the third-order nonlinear susceptibility by  $n_2 = (2\pi / n_o) \chi_R^{(3)}$ . The at-

tenuation of the irradiance in the right hand-side of Eq. (II.3) is due to linear absorption, TPA and absorption by the PGC, respectively. In our experiment, TPA and the absorption due to the PGC are important at all input intensities we have used (see appendix B). In general, the first term of Eq. (II.4) is dominant at lower irradiance at which the number of carriers is small such that  $\sigma_r N \ll \gamma I$ . However, the second term dominates at very high irradiance at which the density of the PGC is very large. For the range of intensities used in our experiment, the nonlinear refraction due to the free carriers is much larger than that due to the bound electrons. Therefore, we will be considering only the second term of Eq. (II.4).

We assume that the laser beam is Gaussian in its spatial profile and nearly-Gaussian in its temporal profile given at the entrance plane ( $z = 0$ ) of the sample by:

$$I(0, r, t) = I_o \exp\left(-2\left(\frac{r}{w_o}\right)^2\right) \Psi(t), \quad (\text{II.5})$$

where  $w_o$  is the  $1/e^2$  radius at  $z = 0$  and  $\Psi(t)$  is a function which describes the temporal profile given by:

$$\Psi(t) = \begin{cases} \exp\left(-\left(\frac{t}{t_0}\right)^2\right), & t < 0 \\ \frac{1}{n_g} \left[ \exp\left(-\left(\frac{t}{t_0}\right)^2\right) + (n_g - 1) \exp\left(-\left(\frac{t}{t_1}\right)^2\right) \right], & t \geq 0 \end{cases} \quad (\text{II.6})$$

For convenience, we assumed that the peak of the pulse is at  $t = 0$ . The leading part of the pulse can be described by  $\Psi(t)$  for  $t < 0$  while the trailing part of the pulse is described by  $\Psi(t)$  for  $t \geq 0$ .  $n_g$  is an integer representing the number of

Gaussians involved in fitting the trailing part of the pulse and equals 2.  $t_o$  and  $t_1$  are 1/e half width of the corresponding Gaussian temporal profile. By fitting the leading edge of the pulse, we find  $t_o$  while  $t_1$  is obtained by fitting the trailing edge of the pulse. In Eq. (II.5),  $I_o$  is the peak irradiance,  $I(o, o, o)$ , given by

$$I_o = \frac{4n_g \mathcal{E}_{total}}{\sqrt{\pi}[(n_g + 1)t_o + (n_g - 1)t_1](\pi w_o^2)}, \quad (\text{II.7})$$

where  $\mathcal{E}_{total}$  is the total input energy of the laser beam at the entrance plane of the sample.

The photogenerated carriers concentration,  $N(z, r, t)$ , is given by

$$\frac{\partial N(z, r, t)}{\partial t} = \frac{\beta I^2(z, r, t)}{2\hbar\omega} - \frac{N(z, r, t) - N_o}{\tau}, \quad (\text{II.8})$$

where  $\tau$  is the recombination lifetime of the carriers and  $N_o$  is the free carrier density without illumination. In the above equation, we considered the dominant mechanism of excitation to be two-photon absorption. Diffusion has been neglected in Eq. (II.8) since the carrier diffusion length ( $\sqrt{D_a \tau} < 2 \mu\text{m}$ ) is much smaller than the beam spot size at the sample position (where  $D_a$  is the ambipolar diffusion coefficient). The first term of Eq. (II.8) indicates the generation of the free carriers while the second term represents the decay of carriers via the recombination process. In general, the recombination of the carriers can be radiative, nonradiative or a combination of both. Radiative and nonradiative recombination lifetimes are generally dependent on the carrier density. Recently, Taheri *et al.* [23] found that, for CdTe,  $\tau$  can be considered independent of the carrier density for  $N \sim 10^{17} \text{ cm}^{-3}$ . In our experiment the maximum  $N$  was estimated to be on the order of  $10^{17} \text{ cm}^{-3}$  as will be verified in the discussion section.

In order to find the transmitted irradiance and the phase shift at the exit plane of the sample, we have to solve Eq. (II.3), (II.8), and (II.4) numerically. The sample thickness is divided into  $n$  equally-spaced layers. The concentration of the PGC,  $N(z,r,t)$ , is assumed to be constant in each layer but different from one layer to another and the transmitted irradiance of a layer is an input irradiance to the next one. The index  $j$  is an integer representing the layer number. Then, Eq. (II.3) can be integrated to give,

$$I_j(r,t) = \frac{I_{j-1}(r,t) \exp\{-[\alpha_o + \sigma_{fc}N_j(r,t)]l\}}{1 + \frac{\beta I_{j-1}(r,t)}{\alpha_o + \sigma_{fc}N_j(r,t)} (1 + \exp\{-[\alpha_o + \sigma_{fc}N_j(r,t)]l\})}, \quad (\text{II.9})$$

where  $l$  is the thickness of the slice and  $j = 1, 2, 3, \dots, n$ . The input irradiance to the first slice is  $I_0(r,t) = (1 - R)I(0, r, t)$  and the transmitted irradiance at  $z = L$  is  $I_{out}(L, r, t) = (1 - R)I_{j=n}(r, t)$ , where  $L$  and  $R$  are the thickness and the surface reflectivity of the sample, respectively. By considering  $I_0(r,t)$  to be the input irradiance for the first layer, the solution of Eq. (II.8) gives  $N_1(r,t)$  which can be used in Eq. (II.9) to find  $I_1(r,t)$  and this in turn can be used in Eq. (II.8), as an input irradiance to the second layer, to find  $N_2(r,t)$ . We repeat this process until we find  $N_n(r,t)$  and  $I_n(r,t)$ . Eq. (II.8) is solved numerically by using the Runge-Kutta method [24]. The phase shift,  $\phi(L, r, t)$ , can be easily found by integrating Eq. (II.4), which gives

$$\phi(L, r, t) = \phi(0, r, t) + k_o \int_0^L [\gamma I(z, r, t) + \sigma_r N(z, r, t)] dz \quad (\text{II.10})$$

where  $\phi(0, r, t)$  is the phase of the electric field at the entrance plane of the sample given by

$$\phi(0, r, t) = \frac{k_o r^2}{2R(z=0)} \quad (\text{II.11})$$

This phase is responsible for wavefront bending at  $z = 0$ . It represents the deviation of the phase at a point off-axis in the entrance plane of the sample from that at the on-axis point.  $k_o$  is the wave vector in free space and  $R(z = 0)$  is the wavefront radius of curvature which equals 17.5 cm.

(b) Propagation of the Beam outside the Sample

By knowing  $I_{out}(L, r, t)$  and  $\phi(L, r, t)$ , we can find the electric field at any point in space using the Huygens-Fresnel diffraction integral [25]. The electric field at the detector plane is then given by

$$E_{det}\left(z', r', t + \frac{z'}{c_o}\right) = i \frac{2\pi}{\lambda z'} \exp\left(-i \frac{\pi r'^2}{\lambda z'}\right) \int_0^\infty E_{out}(L, r, t) \times \exp\left(-i \frac{\pi r^2}{\lambda z'}\right) J_o\left(\frac{2\pi r' r}{\lambda z'}\right) r dr, \quad (\text{II.12})$$

where  $z'$  is the distance between the detector and the exit surface of the sample,  $\lambda$  is the laser wavelength in free space,  $r'$  is the radial distance,  $J_o$  is the zeroth order Bessel function, and  $E_{out}(L, r, t)$  is the electric field at the exit plane of the crystal given by

$$E_{out}(L, r, t) = \left(\frac{2}{\epsilon_o c_o}\right)^{1/2} \sqrt{I_{out}(L, r, t) \exp[-i\phi(L, r, t)]}. \quad (\text{II.13})$$

To find the spatial profile at certain distance behind the sample, we simply have to find the fluence, an experimentally measured quantity, which is given by

$$F_{det}(z', r') = \frac{\epsilon_o c_o}{2} \int_{-\infty}^{+\infty} \left| E_{det}\left(z', r', t + \frac{z'}{c_o}\right) \right|^2 dt \quad (\text{II.14})$$

At  $z'$ , the temporal profile of a cross sectional area symmetric with respect to the beam axis is the time dependent power given by

$$P_{\text{det}}\left(z', t + \frac{z'}{c_o}\right) = \pi \varepsilon_o c_o \int_0^{r_a} \left| E_{\text{det}}\left(z', r', t + \frac{z'}{c_o}\right) \right|^2 r' dr', \quad (\text{II.15})$$

where  $r_a$  is the pinhole radius.

In evaluating Eq. II.12, the zeroth order Bessel function,  $J_o(x)$ , was approximated by [26]

$$J_o(x) \cong \sqrt{\frac{2}{\pi x}} \sin\left(x - \frac{\pi}{4}\right) \quad (\text{II.16})$$

for  $x > 5$  and ,

$$\begin{aligned} J_o(x) \cong 1 - \frac{x^2}{2^2(1!)^2} + \frac{x^4}{2^4(2!)^2} - \frac{x^6}{2^6(3!)^2} + \frac{x^8}{2^8(4!)^2} - \frac{x^{10}}{2^{10}(5!)^2} \\ + \frac{x^{12}}{2^{12}(6!)^2} - \frac{x^{14}}{2^{14}(7!)^2} + \frac{x^{16}}{2^{16}(8!)^2} - \frac{x^{18}}{2^{18}(9!)^2} + \frac{x^{20}}{2^{20}(10!)^2} \end{aligned} \quad (\text{II.17})$$

for  $0 \leq x \leq 5$ . In the above expressions  $x = (2\pi r' r / \lambda z')$ .

#### 4. Results and Discussion

Experimentally, we investigated the spatial and temporal profiles changes as a function of the input irradiance and the distance from the exit surface of the sample. For an input irradiance above  $4.5 \text{ MW/cm}^2$ , the transmitted spatial and temporal profiles show effects which are irradiance-dependent. We observed that the broadening of the beam increased as the input irradiance increased. Figure II.4 shows the experimental and the theoretical [from Eq. (II.14)] spatial profiles at  $z' = 6 \text{ cm}$  behind the sample for different input intensities. The spatial profile continued defocusing until  $I_o = 11 \text{ MW/cm}^2$  when the beam re-

sembled a top hat beam profile. When the irradiance increased above 11 MW/cm<sup>2</sup>, a dip started to appear in the central region of the beam. This dip became deeper as the input irradiance increased. At  $I_o=20.7$  MW/cm<sup>2</sup>, a small peak appeared in the center of the beam.

The transmitted spatial profile at  $z' = 10$  cm is shown in Figure II.5. Again the beam became broader as the input intensity increased. However, in this case the beam structure is different from the previous case. At  $I_o = 12.1$  MW/cm<sup>2</sup>, the beam profile is not a top-hat profile but is similar to a broadened Gaussian profile. When  $I_o = 15.5$  MW/cm<sup>2</sup>, the beam profile is almost flat but has a small peak in the center. The spatial profile has a three peak structure when  $I_o=24.1$  MW/cm<sup>2</sup>, instead of one peak as in the input beam profile.

We monitored the temporal profile using a 100  $\mu$ m pinhole placed at different distances behind the crystal. The pinhole was positioned such that its center coincides with that of the beam. We observed that the temporal profile experienced compression as the input irradiance increased. For the same input power, the amount of compression decreases as the distance from the sample increases. At  $I_o=18.4$  MW/cm<sup>2</sup>, the full width at half maximum, as seen in Figure II.6, is about half of that of the input pulse (see Figure II.2). When  $I_o=24$  MW/cm<sup>2</sup> a peak starts to appear in the trailing edge of the pulse. Figure II.7 shows the transmitted pulses at 32.2 MW/cm<sup>2</sup> and the theoretical fit for two different distances from the sample. Notice that the bottom of the valley between these two peaks occurs at higher intensities as  $z'$  increases. We noticed that the compression and modulation of the temporal profile decreases as the detection area is increased from 100 microns to 600 microns. In fact, when all the light was collected by the detector, the temporal profile showed neither



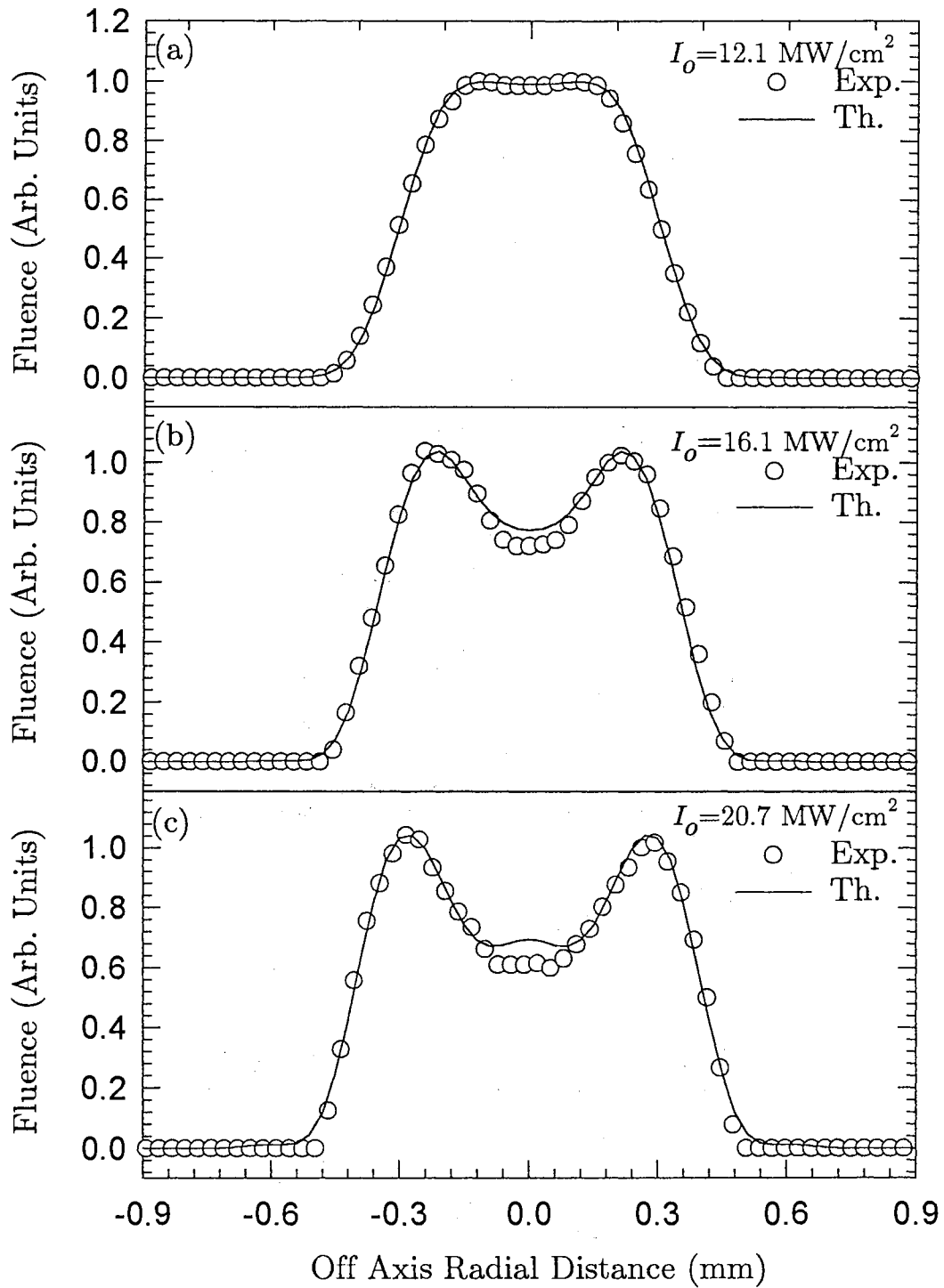


Figure II.4. The experimental transmitted spatial profiles, through a 1.36 mm AR coated sample, measured at 6 cm behind the sample are represented by the hollow circles. The solid lines are the numerical solution of Eq. (II.14) using the following values for the parameters:  $\alpha_o = 0.3 \text{ cm}^{-1}$ ,  $\beta = 22 \text{ cm}^2/\text{GW}$ ,  $\sigma_e = 25 \times 10^{-18} \text{ cm}^2$ ,  $\tau = 12 \text{ ns}$  and  $\sigma_r = -6 \times 10^{-21} \text{ cm}^3$ . The plots show the defocusing effect for three different input irradiances; (a)  $12.1 \text{ MW/cm}^2$  (b)  $16.1 \text{ MW/cm}^2$  (c)  $20.7 \text{ MW/cm}^2$ .

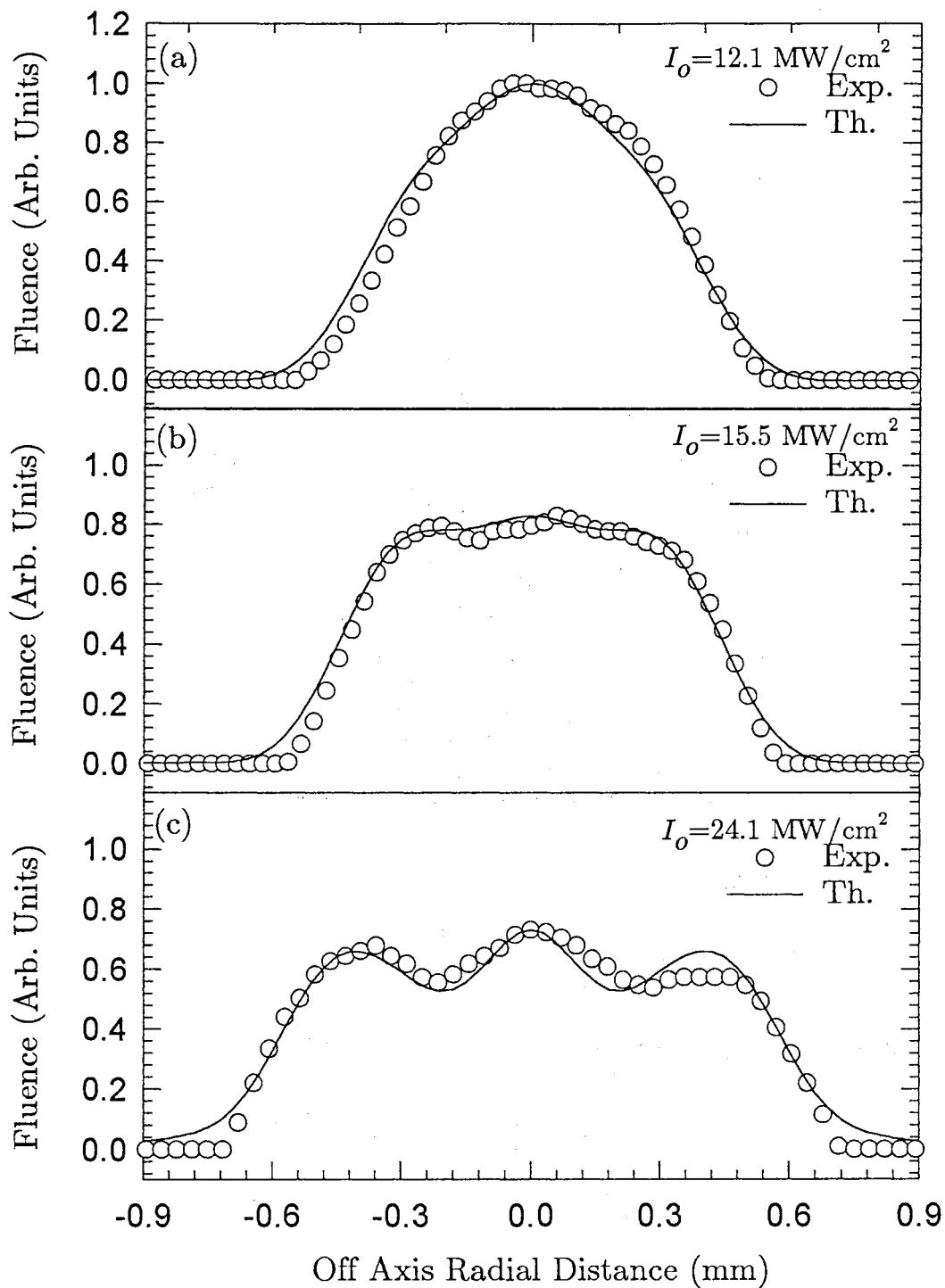


Figure II.5. The experimental transmitted beam profiles, through a 1.36 mm AR coated sample, detected at 10 cm behind the sample are represented by the hollow circles. The solid lines are the theoretical spatial profiles using Eq. (II.14) and the same set of parameters as in Figure II.4. The plots show the defocusing and the ring structure effects for three different input irradiances; (a)  $12.1 \text{ MW/cm}^2$  (b)  $15.5 \text{ MW/cm}^2$  (c)  $24.1 \text{ MW/cm}^2$ .

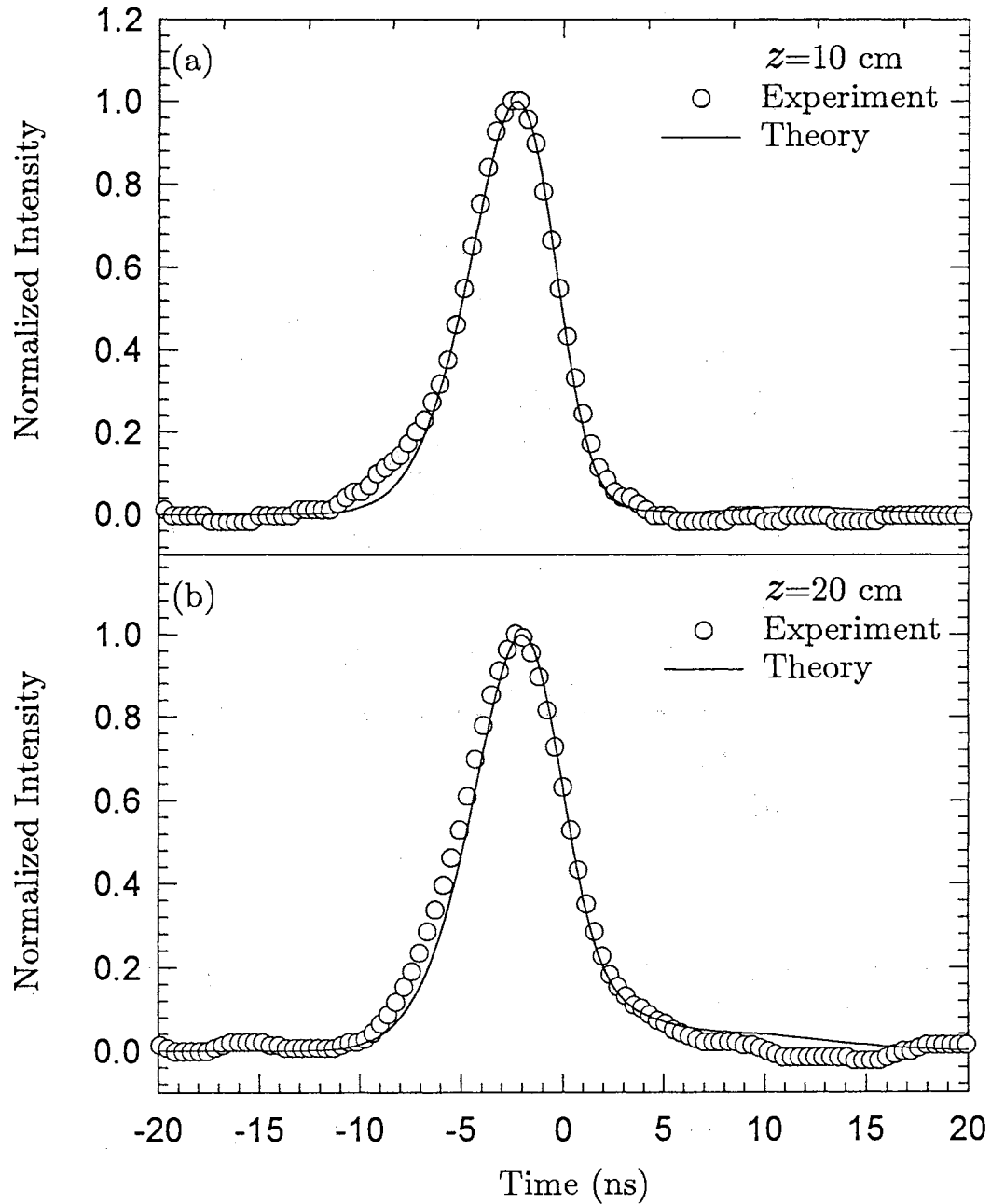


Figure II.6. The experimental results of the transmitted temporal profiles using a 1.36 mm AR coated sample and input irradiance  $18.4 \text{ MW/cm}^2$  are represented by the hollow circles. The solid lines are the corresponding theoretical results using Eq. (II.15) and the same set of parameters as in Figure II.4. The data was taken at (a) 10 cm and (b) 20 cm from the exit plane of the CdTe sample. The data show the pulse compression effect. The pulse has been reduced from 10 ns to 5 ns (FWHM).

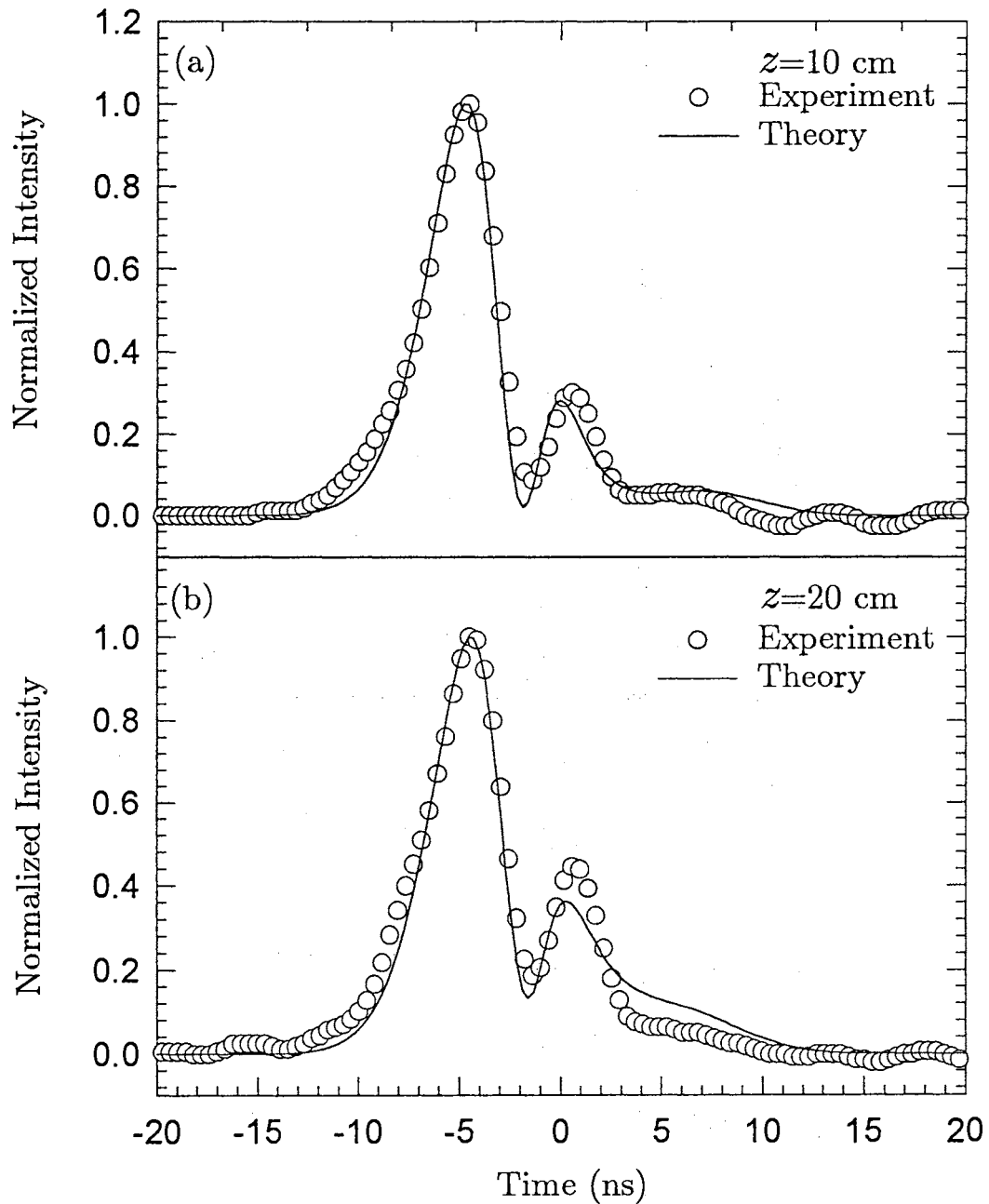


Figure II.7. The experimental results of the transmitted temporal profiles using a 1.36 mm AR coated sample and input irradiance  $32.2 \text{ MW/cm}^2$  are represented by the hollow circles. The solid lines are the numerical simulation using Eq. (II.15) and the same set of parameters as in Figure II.4. The data was taken at (a) 10 cm and (b) 20 cm from the exit plane of the CdTe sample. Notice the additional structure in the trailing edge of the pulse. These results show the pulse modulation effect.

compression nor modulation which is predicted by the theory when Eq. (II.15) was integrated over the size of the beam. To explain this, let us see what happens to the temporal profiles of different points (on-axis and off-axis points) within the beam. The temporal profiles of points on-axis and in the vicinity of the center will experience the maximum compression and modulation since the change in the index of refraction in this region is very large. As a result, the amount of compression and modulation decreases as we move toward the edge of the beam. Moreover, the points near the center of the beam will experience more attenuation than those away from the center. In other words, the temporal profiles for points away from the center will experience less compression and modulation, see Figure II.8. So, when we collect the whole beam, we average over all the temporal profiles of these points which will lead to an attenuated temporal profile with no observed compression or modulation.

To further demonstrate that the reshaping effect is due to phase encoding and not the Fabry-Perot effect, we used a wedge sample for which we were able to, physically, separate the transmitted beams. However, the beams within the sample are spatially overlapped since the sample is thin and the wedge angle is very small. We monitored the first three transmitted beams at  $z' = 20$  cm for different input irradiances. The first transmitted beam passes through the sample once; the second beam passes through the sample three times while the third beam passes through the sample five times. Again we used the  $100 \mu\text{m}$  pinhole directly before the photodetector. The compression was observed to increase for beams that traveled several times through the sample. Figure II.9 shows the temporal pulses which were transmitted and the theoretical fit when the input irradiance was  $10.5 \text{ MW/cm}^2$ . We noticed that the first beam

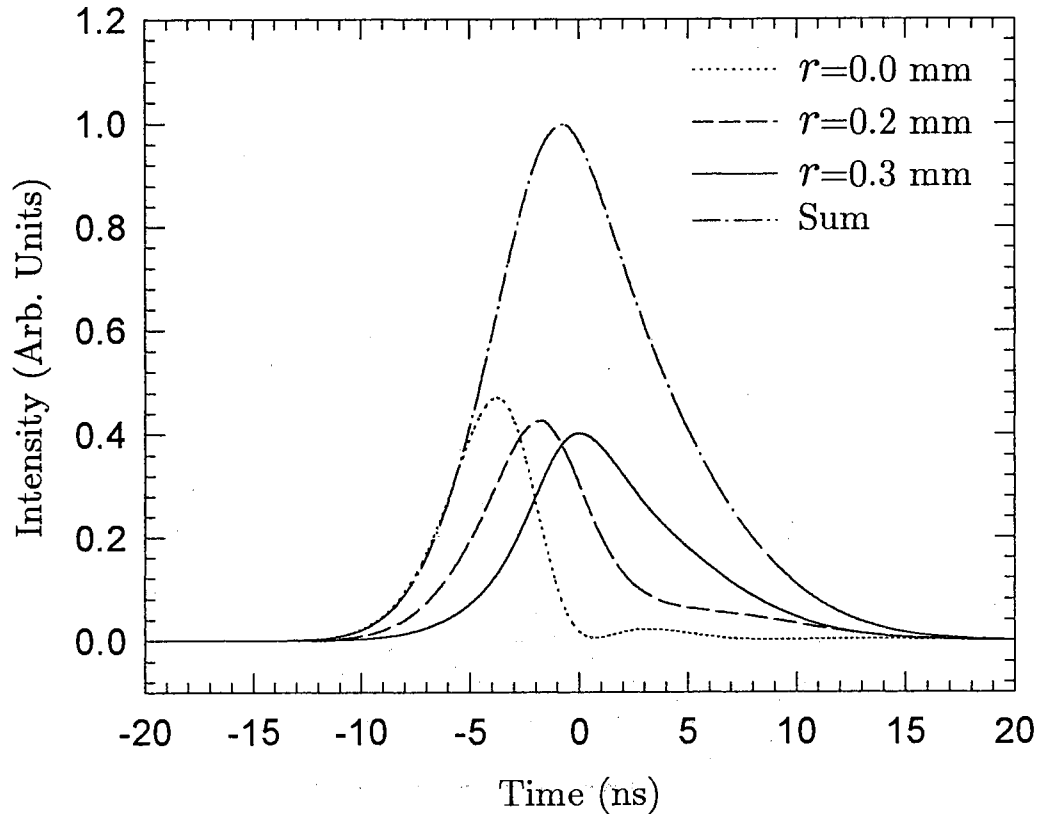


Figure II.8. The temporal profiles of different points within the laser beam. The Figure shows how compression and modulation decrease for points away from the center of the beam. It also demonstrates how compression and modulation reduce considerably by adding the temporal profiles of these points. This result was calculated using our model.

experienced some compression; the second beam experienced more compression and the third beam experienced modulation and more compression. In modeling these results, we assumed that the TPA process took place in the first pass (after the first pass there is not enough intensity to cause appreciable TPA). Hence, the successive multireflections will cause negligible change in the index of refraction compared to that induced by the first pass. This means that the main difference between the beam with one pass and those with many passes is

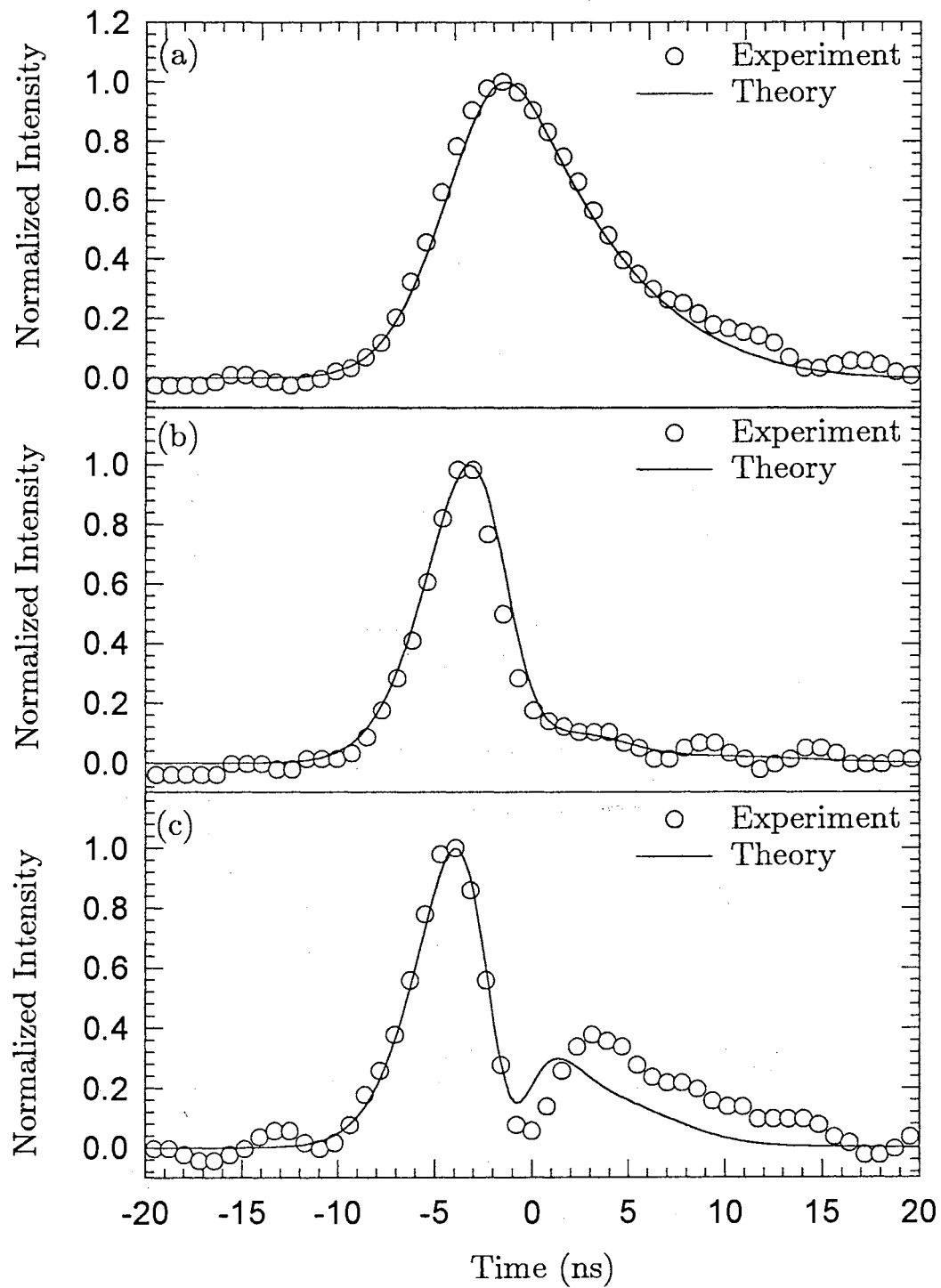


Figure II.9. The experimental results of the transmitted temporal profiles using a 1.5 mm 50% reflectivity wedge sample and input irradiance  $10.5 \text{ MW/cm}^2$  are represented by the hollow circles. The solid lines are the numerical simulation using Eq. (II.15) and the same set of parameters as in Figure II.4. The transmitted signal was measured after (a) one pass, (b) three passes and (c) five passes through the CdTe crystal. The plots show pulse compression and modulation. The data was taken at 20 cm from the exit plane of the sample.

that the beam with multiple passes will experience a larger phase shift since it effectively propagates through a longer nonlinear medium, and as a result the second and the third beams experience more compression and modulation. With this assumption, the model seems to predict the experimental results accurately. Therefore, pulse reshaping using a wedge crystal might be good for some application where we need to choose different temporal pulse shapes using one crystal and one input irradiance.

Self-defocusing is a nonlinear phenomenon which occurs when the sample acts as a negative lens. If the change in the refractive index is negative, i.e. it decreases with the input intensity, then the phase fronts in the center of the beam will propagate faster than those off-axis. This will cause the phase fronts of the beam to bend outwards and this in turn will result in self-defocusing. In our experiment the potential mechanisms that could lead to the nonlinear change in the index of refraction are electron-hole plasma generation and thermal heating. For CdTe, the refractive index increases with temperature [27]. Therefore, if the thermal effect is dominant we should observe self-focusing instead of self-defocusing. However, the experimental results indicate clearly that we have self-defocusing effect. It turns out that the induced change in the index of refraction is due to the PGC created by the TPA process. Based on the work done by Auston *et al.* [19], the change in the index of refraction due to the free carriers is given by  $\Delta n = \sigma_r N$ , where  $\sigma_r$  is expressed as

$$\sigma_r(\text{cm}^3) = -\frac{10^6 \hbar^2}{2n_o \epsilon_o m_{eh} E_p^2} \left( \frac{E_g^2}{E_g^2 - E_p^2} \right), \quad (\text{II.18})$$



where  $E_p$  and  $E_g$  are the energies, in eV units, for the incident photon and the band gap, respectively. The rest of the parameters in the above equation are in SI units. Eq. (II.18) indicates that the change in the index of refraction is negative for  $E_p < E_g$  which means that the medium will act as a diverging lens. By using  $E_g=1.44$  eV,  $E_p=1.17$  eV, and  $n_o=2.84$  in the above equation, we find  $\sigma_r = -6.2 \times 10^{-21} \text{ cm}^3$  which is very close to the result ( $\sigma_r = -6.0 \times 10^{-21} \text{ cm}^3$ ) obtained by fitting of the experimental temporal and spatial profiles. This indicates that the change in the nonlinear refraction is due mainly to the electron-hole plasma generated by the TPA process.

There have been several values of the TPA coefficient reported for CdTe. Table II.2 shows some of these experimental and theoretical values. The experimental values of  $\beta$  were determined by using nanosecond [28,29] and picosecond [18] pulses. In most of these experiments the  $\beta$  value was found by fitting the transmitted energy of a single pump beam or by using the z-scan technique [30]. Recently, Taheri *et al.* [23] measured the TPA coefficient using a pump-probe technique. The advantage of this method is that one can separately find the TPA coefficient and the free carrier absorption cross-section since the probe beam is weak enough not to cause any TPA. Our measured value of the TPA coefficient ( $\beta=22 \text{ cm/GW}$ ) agrees well with the recently reported experimental values [18, 23, 30] and the parabolic band structure model [19, 31].

Our value for the free carrier absorption cross section ( $\sigma_{fc}=25 \times 10^{-18} \text{ cm}^2$ ) agrees well with the value reported by reference [23] ( $\sigma_{fc}=20 \times 10^{-18} \text{ cm}^2$ ). From the fitting, we found that  $\tau=12$  ns which was in the range ( $12 \pm 9$  ns) given by reference [32] and larger than the value reported by reference [23] ( $\tau = 5$  ns). At  $32.2 \text{ MW/cm}^2$ , we estimate [from Eq. (II.8)] that the maximum on-axis

Table II.2. Experimental and theoretical values of the two-photon absorption coefficient for CdTe.

$\beta_{\text{experiment}}$ (cm/GW)	Reference	$\beta_{\text{Theory}}$ (cm/GW)	Reference
22	Present work	7	36
22	18	18	37
20	23	25.1	18
25	33	34	38
26	30	37	39
130	29	200	40
170	34		
200	35		

carrier density achieved in our experiment is  $N = 1.6 \times 10^{17} \text{ cm}^{-3}$ . For such a carrier density we can consider  $\tau$  in Eq. (8) to be independent of  $N$  [23]. The behavior of the photogenerated carriers density at different locations inside the sample is shown in Figure II.10(a). The Figure shows clearly that  $N(t)$  is not following the pulse shape. This kind of behavior is, mainly, due to the effectiveness and competition among three factors namely, TPA, FCA, and free carrier recombination. Effective pumping of free carriers to the conduction band will not start till the pulse has certain intensity. This means that in the beginning of the pulse  $N$  is very small. When the intensity of the pulse reaches about  $8 \text{ MW/cm}^2$  the effective pumping will start to take place. As time evolves the intensity of the pulse increases and the number of free carriers increases as well. Since the recombination life time of the carriers is comparable to the pulse duration this gives the free carriers the chance to cumulate, at least during the rising part of the pulse. However, because of this large number of carriers, that already in the conduction band, the pulse intensity will experience severe attenuation due to the FCA. This in turn reduces the effective intensity available to excite carriers to the conduction band. The recombination of these carriers will start to take place at some time during the trailing part of the signal. The decay of the free carriers and the decrease in the pulse intensity along with large FCA will cause the number of the free carriers to decrease.

The maximum change in the refractive index at  $I_o = 32.2 \text{ MW/cm}^2$  is estimated to be  $-0.001$  (using  $\Delta n(z, r, t) = [\gamma I(z, r, t) + \sigma_r N(z, r, t)]$ ) which will have a negligible effect on the macroscopic refractive index ( $n_o$ ). However, this introduced an appreciable change in the phase equal to  $-8$  radians, which was equivalent to  $1.3$  wavelengths. We have seen that even for values of  $\Delta\phi$  as

small as -1.3 radians (at 12.1 MW/cm<sup>2</sup>), the self-defocusing effect was pronounced. The behavior of  $\Delta n(t)$  is similar to that of  $N(t)$ . Figure II.10(b) shows the on-axis  $\Delta n(t)$  for different input irradiances.

The pulse reshaping effect seems to be a good method for determining some of the nonlinear properties of CdTe. However, to get accurate values for the nonlinear parameters one should not rely on the experimental results obtained at a certain distance from the sample using a specific laser intensity. We found that it was easy to fit, for example, the spatial profile at some distance for a certain input intensity by choosing a set of values for the nonlinear parameters. However, by using this set of parameters it is not guaranteed that the model will predict the spatial or the temporal profile for different conditions, (i.e., for different distances from the sample and different input intensities). Rather, one has to consider the results of the pulse reshaping at different input intensities and different distances behind the sample. We found that the best way to determine the nonlinear parameters is to fit simultaneously two of the experimental results at two different distances and input intensities. By using this method, we obtained the set of parameters ( $\alpha_o=0.3 \text{ cm}^{-1}$ ,  $\beta=22 \text{ cm}^2/\text{GW}$ ,  $\sigma_{fc}=25 \times 10^{-18} \text{ cm}^2$ ,  $\tau=12 \text{ ns}$  and  $\sigma_r=-6 \times 10^{-21} \text{ cm}^3$ ) which seems to produce good fits for the temporal and the spatial profiles at different input intensities and distances behind the sample. Moreover, these values are in good agreement with the most recent results in the literature.

## 5. Conclusion

We have reported experimental and theoretical results of self-defocusing and pulse compression of nanosecond pulses emerging from CdTe crystals. The

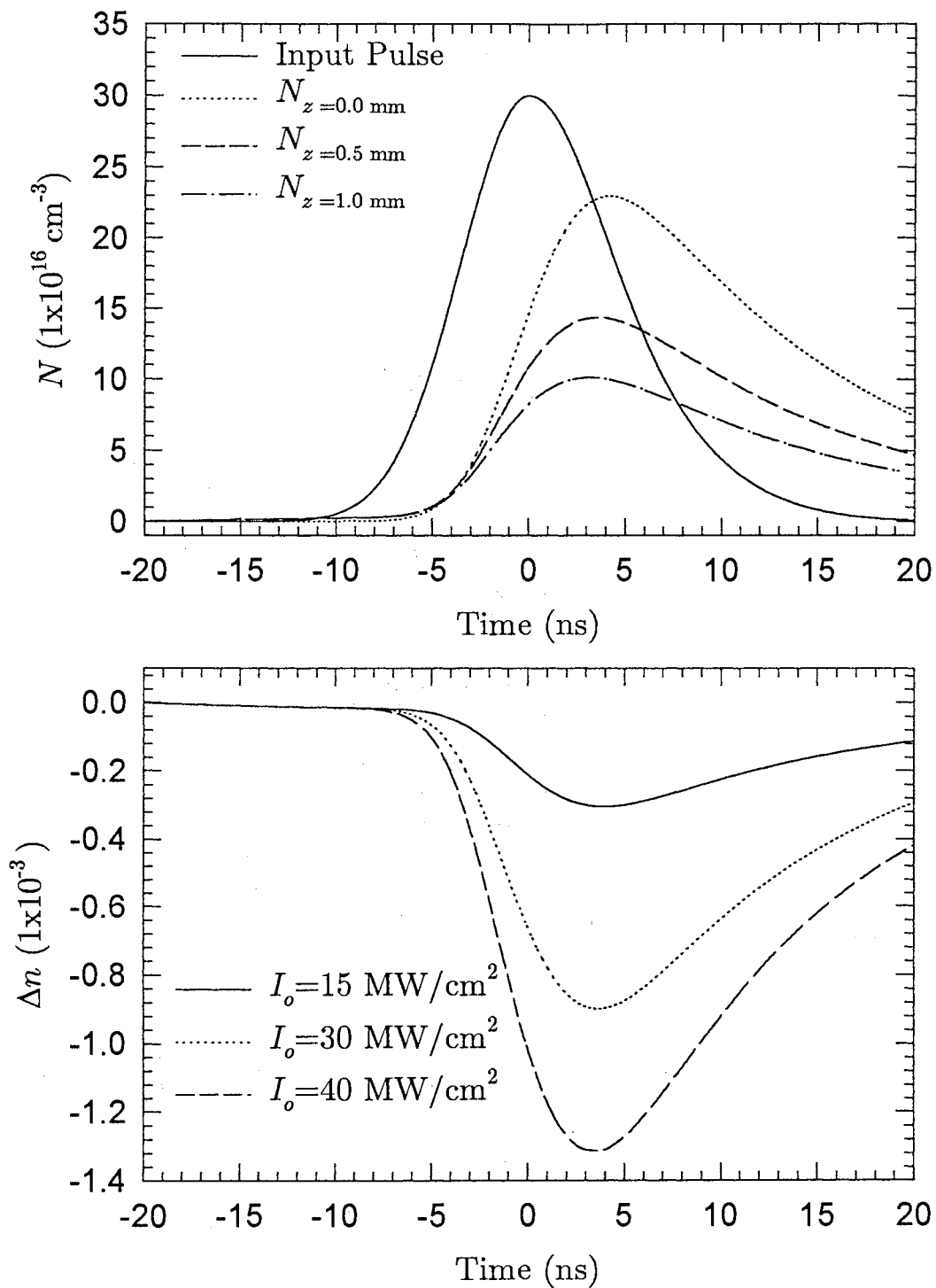


Figure II.10. (a) On-axis photogenerated carriers density at different point within the sample. The temporal profile of the  $30 \text{ MW/cm}^2$  input pulse is shown in order to compare it with the behavior of  $N(t)$ . (b) The time dependent nonlinear change in the index of refraction for different values of the peak irradiance.

nonlinear refraction was due to the free carriers generated by the two-photon absorption process. Good agreement is obtained between the theoretical and the experimental results. The values of the nonlinear parameters deduced from fitting the experimental results were found to agree well with the existing theories and the recent experimental values reported in the literature. Finally, we found that the effect of the sample is to encode a radially and temporally dependent phase shift which causes the reshaping as the pulse evolves in space and time.

CHAPTER III  
TWO-PHOTON INDUCED OPTICAL SWITCHING  
USING A CdTe ETALON

1. Introduction

Since the first observation of optical bistability (OB) by Gibbs and co-workers [41], a significant number of studies have been conducted [8,42]. The interest in this field stems from the potential applications to all-optical switching, optical computing, and communication [8]. The investigation of optical switching (OS) in semiconductors is important because they have large nonlinear and fast relaxation processes. Semiconductors also possess a variety of nonlinear mechanisms that can change the index of refraction and the absorption coefficient. Since the initial observations of OB by Miller *et al.*[43] and Gibbs *et al.*[44] many authors have reported the observation of OB in various semiconductors [45-50]. Two-photon induced OB in CdHgTe [45] and InSb [47] has been reported. In the latter two studies, the Fabry-Perot etalon was utilized to observe the OB. Also, optical limiting and pulse compression have been studied in HgCdTe [51] and ZnSe [52], respectively.

We have found only one reported study of OB in CdTe. The cause of the bistable switching was due to increasing absorption [53]. The photon energies employed in that study were in the vicinity of the CdTe band gap and the dominant nonlinear process was through single-photon absorption. In studying

the two-photon-induced OB in InSb and CdHgTe, the laser radiation used was  $10.6 \mu\text{m}$  since these semiconductors have narrow band-gaps. In contrast, CdTe has a wide band-gap which requires radiation in the near infrared in order for the two-photon process to take place. In optical communications, the wavelengths of interest are in the near infrared regime [54]. This suggests that optical devices based on CdTe might find applications in optical communications.

In this chapter, we report for the first time (to our knowledge) the observation of OS in a CdTe etalon induced by a two-photon absorption process using 11 ns pulses at  $1.064 \mu\text{m}$ . We also observed optical limiting and pulse compression. The origin of the nonlinearity was due to the free carriers generated by the two-photon absorption process. These carriers induced a nonlinear change in the index of refraction that controlled the transmission of the etalon. In modeling the experimental results we assumed a plane-wave approximation. The transmitted intensity of the CdTe etalon was studied as a function of the input intensity and the initial detuning of the etalon. The role of thermal heating on the results was also investigated.

## 2. Experimental Setup

The experimental setup is shown in Figure III.1. The experiments were performed using the fundamental wavelength ( $\lambda = 1.064 \mu\text{m}$ ) of an injection seeded Nd:YAG laser with pulse duration of about 11 ns (full width at half maximum). In order to improve the quality of the spatial profile, the laser beam of 8 mm diameter was allowed to pass through a pinhole of  $600 \mu\text{m}$  in diameter. The transmission of the  $600 \mu\text{m}$  pinhole had a diffraction pattern in



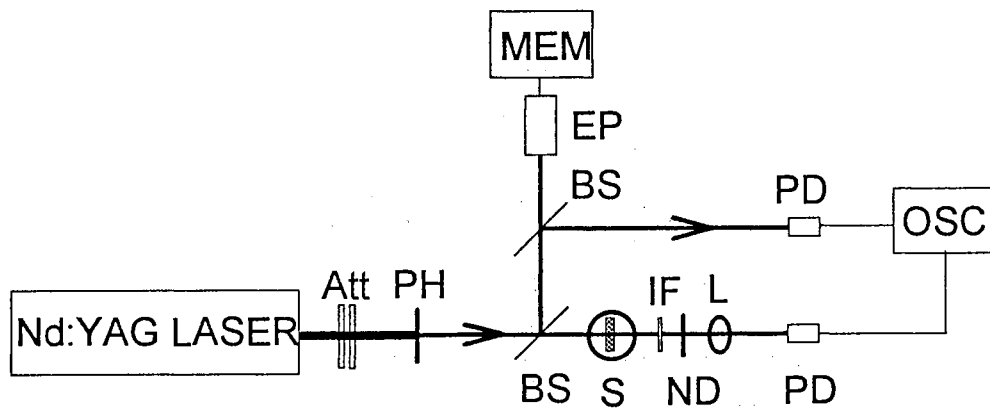


Figure III.1. Experimental setup for observing optical switching: Att- attenuator, PH- pinhole, BS- beam splitter, EP- energy probe, MEM- Molelectron energy meter, PD- photodetector, S- sample fixed to a rotatable mount, IF- interference filter, ND- neutral density filters, L- lens, OSC- oscilloscope.

which the secondary peaks were very small compared to the main peak (Airy disc) which can be fitted to a Gaussian. This main peak had about 85% of the total energy of the incident beam at the entrance surface of the sample. After passing through the pinhole, the laser beam was split such that the transmitted portion of the beam was the input signal beam and the reflected portion was the reference beam. The reference beam was split in order to enable us to monitor the input energy and the input temporal profile.

A second pinhole of  $100\ \mu\text{m}$  diameter was attached to the rear surface of the sample so that a plane-wave approximation would be applicable in our model. This pinhole was positioned such that its center coincided with the center of the input laser beam. When the spot size ( $w_o$ ) of the laser beam is much larger than the radius ( $a$ ) of the pinhole then the illumination confined within the pinhole area can be approximated by a plane-wave. In mathematical terms, if  $\delta_a = \exp(-(a/w_o)^2) = 1$ , [55] then the illumination is a plane-wave. For our experiment,  $w_o = 300\ \mu\text{m}$  and  $\delta_a = 0.97$ , therefore, the plane-wave approximation is justified. The diffraction from the  $100\ \mu\text{m}$  pinhole had no effect on the results since all the transmitted laser light was focused onto a photodetector.

We used a CdTe etalon of 1.356 mm thickness with 23% reflectivity on both sides and a parallelism better than 10 seconds of arc. The sample was fixed to a rotatable mount in order to control the initial detuning of the etalon. The temporal profile of both the incident and the transmitted pulses were detected by two ET2000 photodetectors with a rise time  $< 500$  picosecond. Both the input and the output pulses were monitored on a Tektronix 2440 digital oscilloscope for comparison purposes. Since CdTe was known to exhibit second-harmonic generation at  $1.064\ \mu\text{m}$  picosecond pulses excitation [20], an interfer-

ence filter was used after the sample to pass the infrared laser light only. The energy of the input pulses was controlled by an attenuator placed before the 600  $\mu\text{m}$  pinhole and detected by a Molectron energy probe coupled to a Molectron energy meter.

### 3. Theory

When studying the response of a Fabry-Perot etalon, it is important to know the relationship among three time constants: The characteristic time of the input intensity  $\tau_p$ , i.e., the laser pulse duration, the medium response time,  $\tau_m$ , which is the recombination life-time of the free-carriers in semiconductors and the cavity round trip time,  $\tau_c$ . It is necessary to have  $\tau_p > \tau_c$  for the transmitted pulses to interfere. In fact, if  $\tau_p \gg M\tau_c$  then the transmission of the Fabry-Perot etalon can be described completely by the classical formula (Airy function). The number of the transmitted beams that contribute to the interference pattern is approximated by twice the finesse ( $M = 2F$ ) [56] of the etalon. The importance and the relation between  $\tau_c$  and  $\tau_m$  will be discussed in the following paragraph when we talk about the nonlinear change in the index of refraction.

At 1064 nm, CdTe is a two-photon absorber. As a result, the main mechanism of carrier excitation is due to two-photon absorption (TPA). However, the intensity attenuation is mainly caused by both TPA and free-carrier absorption (FCA). Here, the free carriers are those generated by the TPA process. Consider that TPA occurs only on the first pass through the sample (since the intensities of the reflected beams are weak so that TPA is negligible compared to that in the first pass) while FCA occurs all the time after they are generated. This means that the free-carriers are created in the first pass only.

These photogenerated carriers will induce a nonlinear change in the index of refraction,  $\Delta n(t)$ , proportional to the carrier density,  $N(t)$ , given by

$$\Delta n(t) = \sigma_r N(t). \quad (\text{III.1})$$

The coefficient  $\sigma_r$  is the change in the index of refraction per unit photogenerated carrier density. This change in the index of refraction described in Eq. (III.1) is due to the intensity of the initial laser beam. The successive reflections (multireflections) will be able to experience this change in the index of refraction if and only if the medium response time is much larger than the cavity round trip time,  $\tau_m \gg \tau_c$ .

In deriving a formula for the transmission of the etalon, we follow the classical derivation of a plane Fabry-Perot etalon. This is valid since both the pulse duration and the recombination lifetime of the free carriers are much larger than the cavity round trip time. Consider  $E_o$  to be the amplitude of the incident electric field and  $E_{c1}$  the field amplitude at  $z=L$  after the first pass. In our case the field reflection and transmission coefficients ( $r'$  and  $t'$ , respectively) are the same for both surfaces of the etalon. Define  $\phi_o$  to be the initial detuning of the cavity which is given by

$$\phi_o = \frac{4\pi}{\lambda} L \sqrt{n_o^2 - \text{Sin}^2(\theta_i)}. \quad (\text{III.2})$$

The time-dependent phase difference between two successively transmitted beams caused by the nonlinear change of the refractive index due to the light-matter interaction in the first pass is given by

$$\phi(t) = \frac{4\pi L}{\lambda} \Delta \bar{n}(t) \quad (\text{III.3})$$

where  $\lambda$  is the laser wavelength in free space. In the last two equations  $L$  is the length of the etalon,  $n_o$  is the linear index of refraction,  $\theta_i$  is the angle of incidence relative to the normal of the sample front surface, and  $\Delta \bar{n}(t)$  is the average time-dependent change in the index of refraction given by

$$\Delta \bar{n}(t) = \frac{\sigma_r}{L} \int_0^L N(z, t) dz, \quad (\text{III.4})$$

where  $N(z, t)$  is the free carrier density as a function of time and distance within the sample. Therefore, the total phase difference between two successively transmitted beams is  $\Delta\phi(t) = \phi(t) + \phi_o$  [57].

By considering the above conditions, it is straight forward to show that the transmitted field of the etalon is given by

$$\begin{aligned} E_t &= E_{c1} t' e^{-i\omega t} \left( 1 + r'^2 e^{-\alpha L} e^{-i(\Delta\phi)} + r'^4 e^{-2\alpha L} e^{-i2(\Delta\phi)} + r'^6 e^{-3\alpha L} e^{-i3(\Delta\phi)} + \dots \right) \\ &= E_{c1} t' e^{-i\omega t} \left( \frac{1}{1 - r'^2 e^{-\alpha L} e^{-i(\Delta\phi)}} \right) \end{aligned} \quad (\text{III.5})$$

where  $E_{c1}$  is the electric field amplitude after the first pass through the sample. In the above equation  $\alpha = \alpha_o + \alpha_{fc}$ , where  $\alpha_o$  is the residual linear absorption coefficient and  $\alpha_{fc}$  is the free carrier absorption coefficient given by  $\sigma_{fc} \bar{N}(t)$ . Here  $\sigma_{fc}$  is the free carrier absorption cross-section. Multiply Eq. (III.5) by its complex conjugate and use the relation  $\cos(\theta) = 1 - 2\sin^2(\theta/2)$ , we obtain the transmitted intensity to be,

$$I_t(t) = \frac{(1 - R)}{(1 - R_\alpha)^2} \cdot \frac{I_{c1}(t)}{1 + (2F / \pi)^2 \text{Sin}^2[\Delta\phi(t) / 2]} \quad (\text{III.6})$$

where  $I_{c1}(t)$  is the cavity intensity at  $z = L$  after the first pass,  $R = r'^2$  is the power reflection coefficient of the sample surfaces, and  $R_\alpha = R \exp(-\alpha L)$  is the effective reflection coefficient.  $F$  is the total finesse of the etalon given by

$F = F_R F_F / (F_R^2 + F_F^2)^{1/2}$  [56] where  $F_R$  is the reflectivity finesse and  $F_F$  is the surface flatness finesse. The reflectivity finesse is defined as  $\pi(R_\alpha)^{1/2} / (1 - R_\alpha)$  and  $F_F$  is equal to  $S/2$  where  $S$  is the fractional wavelength deviation from planeness across the sample surface. The maximum  $F$  in our experiment is about 2.

The laser beam is Gaussian in its spatial profile and nearly-Gaussian in its temporal profile given at the entrance plane ( $z=0$ ) of the sample by Eq. II.5. Because the plane-wave approximation results from the 100  $\mu\text{m}$  pinhole at the rear surface of the CdTe etalon, the radial dependence in Eq. (II.5) is no longer considered. The rate equation of the photogenerated carrier density is then given by

$$\frac{\partial N(z, t)}{\partial t} = \frac{\beta I^2(z, t)}{2\hbar\omega} - \frac{N(z, t) - N_o}{\tau_m}, \quad (\text{III.7})$$

where  $\beta$  is the two-photon absorption coefficient and  $N_o$  is the free carrier density without illumination.

Since the confocal parameter of the beam is larger than the thickness of the sample (external self-action) [21], we can neglect the transverse Laplacian in the wave equation for the propagation inside the nonlinear medium. As a result, we get a nonlinear wave equation in one dimension from which we obtain the irradiance at a distance  $z$  inside the sample to be

$$\frac{\partial I(z, t)}{\partial z} = -\alpha_o I(z, t) - \beta I^2(z, t) - \sigma_{fc} N(z, t) I(z, t). \quad (\text{III.8})$$

$\sigma_{fc}$  is, in general, dependent on the laser pulse duration [22]. The attenuation of the irradiance in the right hand-side of Eq. (III.8) is due to linear absorption, TPA and FCA, respectively.

In order to find  $I_{c1}(t)$  for Eq. (III.6) and  $\Delta\bar{n}(t)$  for Eq. (III.4), we have to solve Eqs. (III.7) and (III.8) numerically. To do this, we divide the sample thickness into  $n$  equally-spaced layers. We also assume that the concentration of the photogenerated carrier density,  $N(z_j, t) = N_j(t)$ , is constant in each layer but different from one layer to another and the transmitted irradiance of a layer is an input irradiance for the next one. The index  $j$  is an integer representing the layer number. Then Eq. (III.8) can be integrated to give,

$$I_j(t) = \frac{I_{j-1}(t) \exp(-\alpha_j l)}{1 + \frac{\beta I_{j-1}(t)}{\alpha_j} (1 + \exp(-\alpha_j l))}, \quad (\text{III.9})$$

where  $\alpha_j = \alpha_0 + \sigma_{fc} N_j(t)$ ,  $l$  is the thickness of the slice and  $j = 1, 2, 3, \dots, n$ . The input irradiance at the first slice is  $I_0(t) = (1 - R)I(0, t)$  and the transmitted irradiance at  $z=L$  is  $I_{c1}(t) = I_{j=n}(t)$ . By considering  $I_0(t)$  to be the input irradiance for the first layer then the solution of Eq. (III.7) gives  $N_1(t)$  which can be used in Eq. (III.9) to find  $I_1(t)$  and this in turn can be used in Eq. (III.8), as an input irradiance to the second layer, to find  $N_2(t)$ . We repeat this process until we find  $N_n(t)$  and  $I_n(t)$ . Eq. (III.7) is solved numerically by using Runge-Kutta method [24]. After finding  $I_{c1}(t)$  and  $\Delta\bar{n}(t)$ , Eq. (III.6) can be used to predict the transmitted intensity of the etalon.

#### 4. Results

In this section, we present the response of the CdTe etalon. At low power, in the linear regime, the transmitted and the reference signals were detected such that they were overlapped (in-phase). This was done to make sure

that any shift in the peak of the transmitted pulse was due to the induced non-linear change in the medium.

We were able to demonstrate optical switching, pulse compression, and optical limiting by changing the input intensity and the initial detuning of the etalon. The hysteresis loops of the output intensity versus the input intensity were found to rotate either clockwise or counterclockwise depending on the input intensity and the initial detuning. The experimental and theoretical results were done for different input intensities and different initial detuning of the CdTe etalon. The latter was achieved by rotating the etalon. The values of  $\theta_i$  were in the range of 0 - 2.3 degrees. For different  $\theta_i$ 's it was necessary to translate the sample such that the center of the laser beam coincides with that of the 100  $\mu\text{m}$  pinhole attached to the rear surface of the CdTe etalon. This means that the incident laser beam was hitting different spots on the front surface of the sample. Although the samples were polished to  $\lambda/4$  which would normally result in a flatness finesse ( $F_F$ ) of 2, visual inspection indicated the presence of imperfections which varied across the sample surface. This suggests that the  $F_F$  might vary slightly across the sample surface. Therefore, we allowed  $F_F$  to slightly vary from 1 to 3 for different values of the angle of incidence.  $F_F$  was the only adjustable parameter in fitting the experimental results.

The results shown in Figure III.2 correspond to  $\phi_o = -0.1\pi$  and a peak input intensity of 14.8 MW/cm<sup>2</sup>. Figure III.2(a) shows the temporal profile of the input intensity (dotted line), and the corresponding experimental (hollow circles) and theoretical (solid line) transmitted intensities. Both, the input and output pulses are normalized to the peak of the input pulse, i.e., divided by the peak intensity of the input pulse. Notice that the top of the output pulse is flat, an



indication of an optical limiting action. The hysteresis loop, Figure III.2(b), shows the limiting action in both the leading and the trailing parts of the pulse. Figure III.2(c) shows the transmission of the etalon as a function of time. From this Figure, we can deduce the switching time needed by the etalon to go from a low to a high transmission state and vice versa. Initially, at low power, the etalon has a high transmission of 0.82 then as the input power increases the transmission starts to decrease till it reaches a minimum transmission of about 0.6 then the transmission goes up to 0.83. Following Fidorra *et al.* [46] we define the switching-down time  $\tau_{\downarrow}$  and the switching-up time  $\tau_{\uparrow}$  to be the times needed by the etalon to go from 10% to 90% of the step. From Figure III.2(c)  $\tau_{\downarrow}$  is 3.7 nanoseconds and  $\tau_{\uparrow}$  is 3.6 nanoseconds. All switching times are accurate to two significant figures.

In Figure III.3 we show the results for  $I_o=17.7 \text{ MW/cm}^2$  and  $\phi_o=-0.1\pi$ . Figure III.3(a) shows switching in the leading part of the transmitted pulse. The peak of the transmitted pulse is now shifted to the right relative to the peak of the reference pulse. The switching intensity is about  $14.9 \text{ MW/cm}^2$ . The output intensity is almost flat for the range of the input intensity from  $12.4 \text{ MW/cm}^2$  to  $16.3 \text{ MW/cm}^2$  [see Figure III.3(b)]. The hysteresis loop shows optical switching. In that Figure, the output suddenly increases for input intensities larger than  $16.3 \text{ MW/cm}^2$ . However, when the input intensity of the trailing pulse reaches  $16.3 \text{ MW/cm}^2$  again, the output intensity starts to decrease. The switching times,  $\tau_{\downarrow}$  and  $\tau_{\uparrow}$ , from Figure III.3(c) are the same and are equal to 2.6 nanoseconds.

For  $\phi_o=0.18\pi$  and  $I_o=12 \text{ MW/cm}^2$ , the temporal profile of the transmitted pulse experienced compression as shown in Figure III.4(a). The input pulse

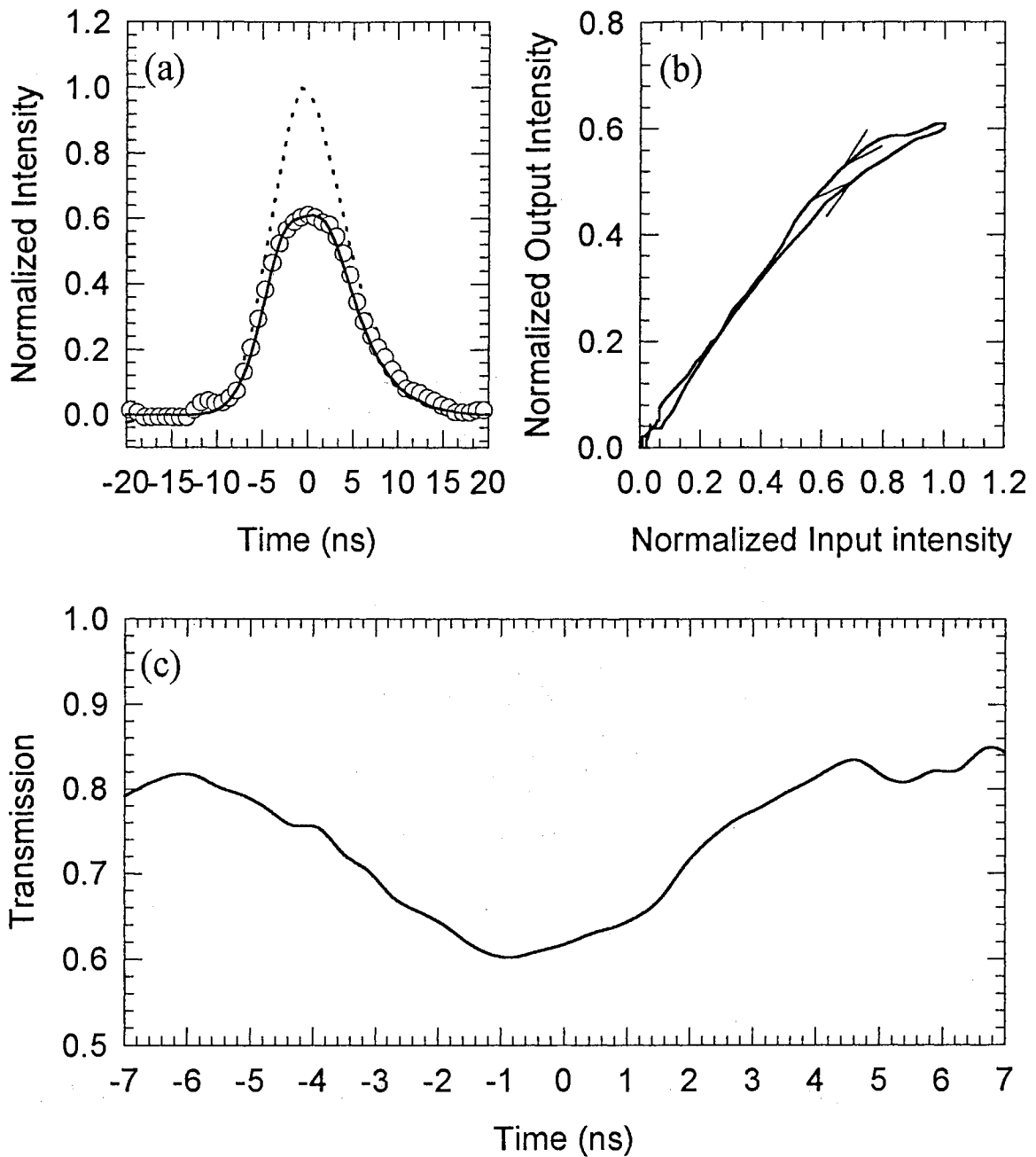


Figure III.2. Experimental and theoretical results for  $I_o=14.8 \text{ MW/cm}^2$ ,  $\phi_o=-0.1\pi$  and  $F_F=1$ . The results show an optical limiting action. (a) The input (dotted line) and output intensities as a function of time. Open circles are the experimental transmitted temporal profile and the solid line is the theoretical result obtained from Eq. (III.7) using the following values for the parameters:  $n_g=2$ ,  $t_o=5 \text{ ns}$ ,  $t_1=8.8 \text{ ns}$ ,  $n_o=2.84$ ,  $\alpha_o=0.3 \text{ cm}^{-1}$ ,  $\beta=22 \text{ cm/GW}$ ,  $\sigma_{fc}=25\times 10^{-18} \text{ cm}^2$ ,  $\tau=12 \text{ ns}$ ,  $N_o=3\times 10^{14} \text{ cm}^{-3}$ , and  $\sigma_r=-6\times 10^{-21} \text{ cm}^3$ . (b) The corresponding hysteresis loop. (c) The ratio of the output to input intensities as a function of time. The switching times are  $\tau_{\downarrow}=3.7 \text{ ns}$  and  $\tau_{\uparrow}=3.6 \text{ ns}$ .

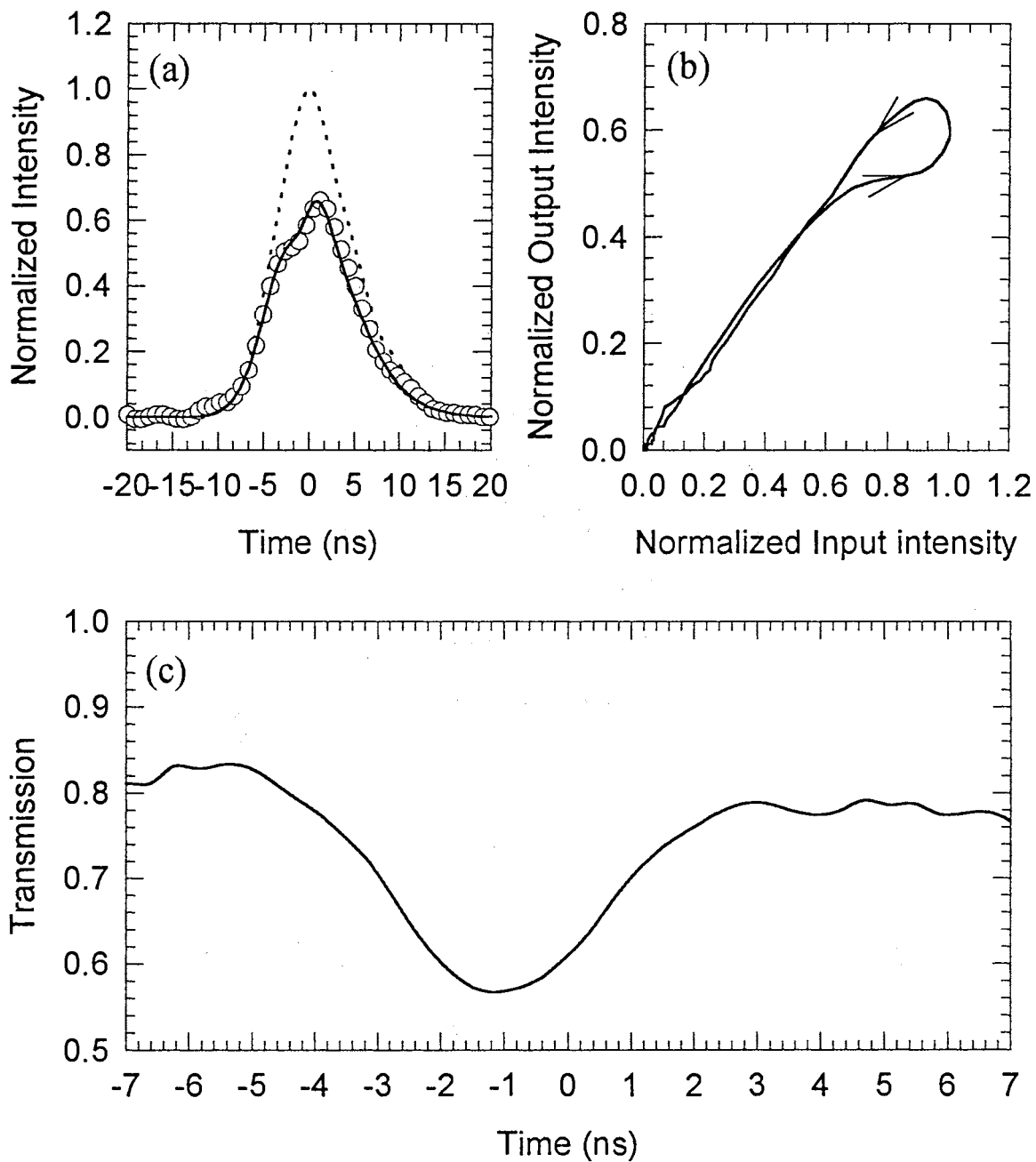


Figure III.3. Experimental and theoretical results for  $I_o=17.7 \text{ MW/cm}^2$ ,  $\phi_o=-0.1\pi$  and  $F_F=1$ . The remaining parameters are the same as in Figure 2. From (c) the switching times are  $\tau_{\downarrow}=2.6 \text{ ns}$  and  $\tau_{\uparrow}=2.6 \text{ ns}$ .

has a duration of about 11 nanoseconds (FWHM) while the emerging pulse has a duration time of about 6.7 nanoseconds (FWHM). The hysteresis loop of the input-output relation is shown in Figure III.4(b). In Figure III.4(c) the etalon initially has a transmission of about 0.6; then when the input intensity becomes  $6.7 \text{ MW/cm}^2$  the transmission increases to 0.8 followed by a switch-down to 0.4. The switching times are  $\tau_{\uparrow} = 1.5 \text{ ns}$  and  $\tau_{\downarrow} = 2.2 \text{ ns}$ . Figure III.5 shows the results for  $I_o = 15.4 \text{ MW/cm}^2$  and  $\phi_o = 0.18\pi$ . The input and output temporal profiles are shown in Figure III.5(a). Notice the switching in the trailing part of the pulse. The corresponding hysteresis loop in Figure III.5(b) shows optical switching. When the input intensity of the leading edge of the pulse is about  $14 \text{ MW/cm}^2$  the output intensity starts decreasing. However, when the input intensity of the trailing part of the signal reaches  $14 \text{ MW/cm}^2$  the etalon switches to a state of almost constant output for the range of input intensities from  $14 \text{ MW/cm}^2$  to  $10.8 \text{ MW/cm}^2$ . For an input intensity less than  $10.8 \text{ MW/cm}^2$  the output intensity starts decreasing. From Figure III.5(c)  $\tau_{\uparrow} = 1.6 \text{ ns}$  and  $\tau_{\downarrow} = 2.2 \text{ ns}$ . Initially the etalon transmission is 0.64; then it increases to maximum transmission of 0.79 followed by a transmission minimum of 0.35. Figure III.6 shows the results for  $\phi_o = -0.24\pi$  and  $I_o = 11.4 \text{ MW/cm}^2$ . The result of Figure III.6(a) is similar to the that of Figure III.2(a); the top of the output pulse is flat for a certain range of input intensities. However, in this case the limiting action starts to appear when the input pulse reaches its maximum. The hysteresis loop in Figure III.6(b) shows that the output intensity increases linearly until the input pulse reaches  $I_o$ . The etalon then switches to a state where the output intensity is constant while the input intensity is decreasing. When the input intensity of the trailing part of the pulse is  $8.4 \text{ MW/cm}^2$ , the output intensity

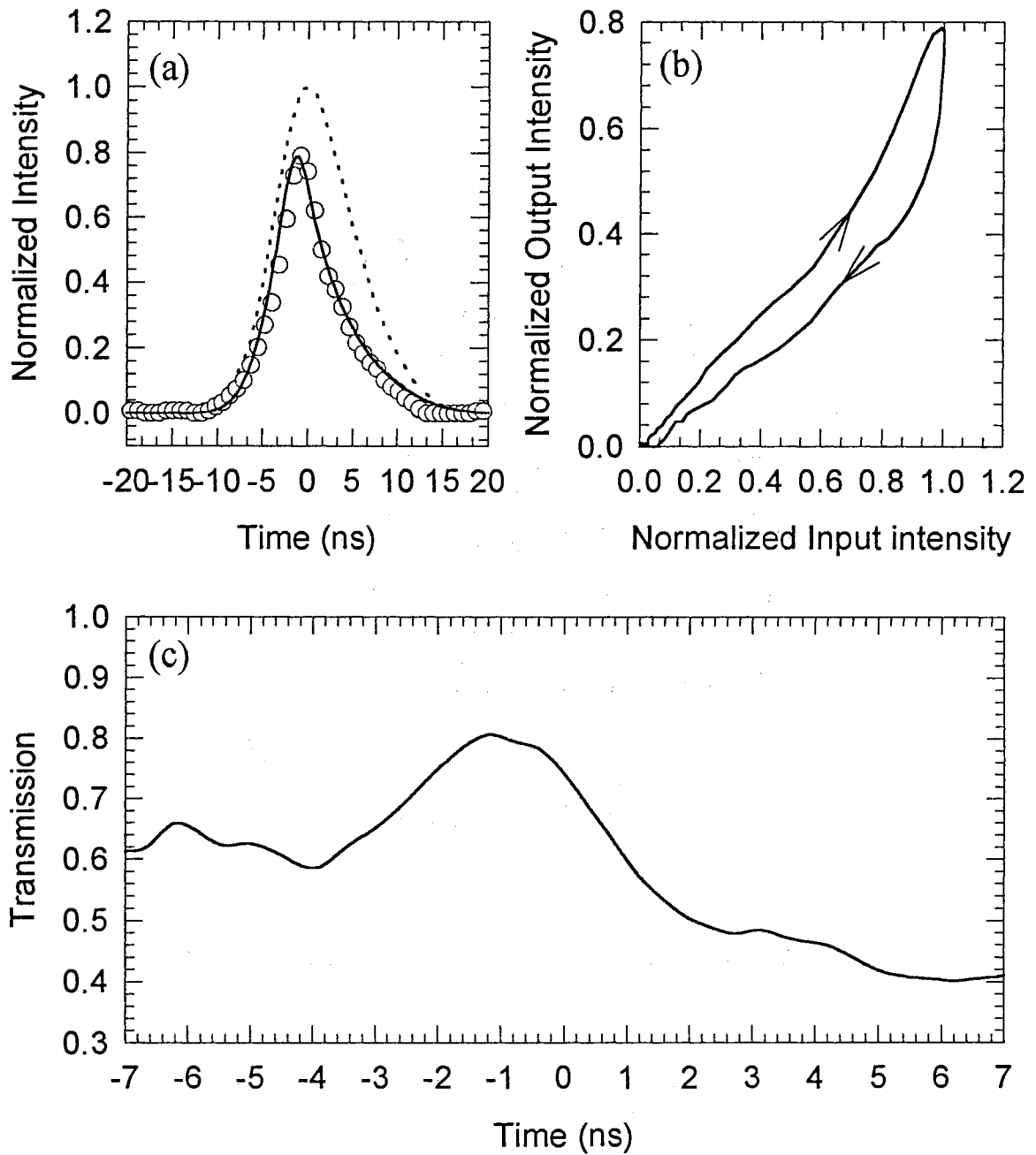


Figure III.4. Experimental and theoretical results for  $I_o=12 \text{ MW/cm}^2$ ,  $\phi_o=0.18\pi$  and  $F_F=3$ . The remaining parameters are the same as in Figure 2. Notice the pulse compression in (a). The switching times are  $\tau_\uparrow=1.5 \text{ ns}$  and  $\tau_\downarrow=2.2 \text{ ns}$ .

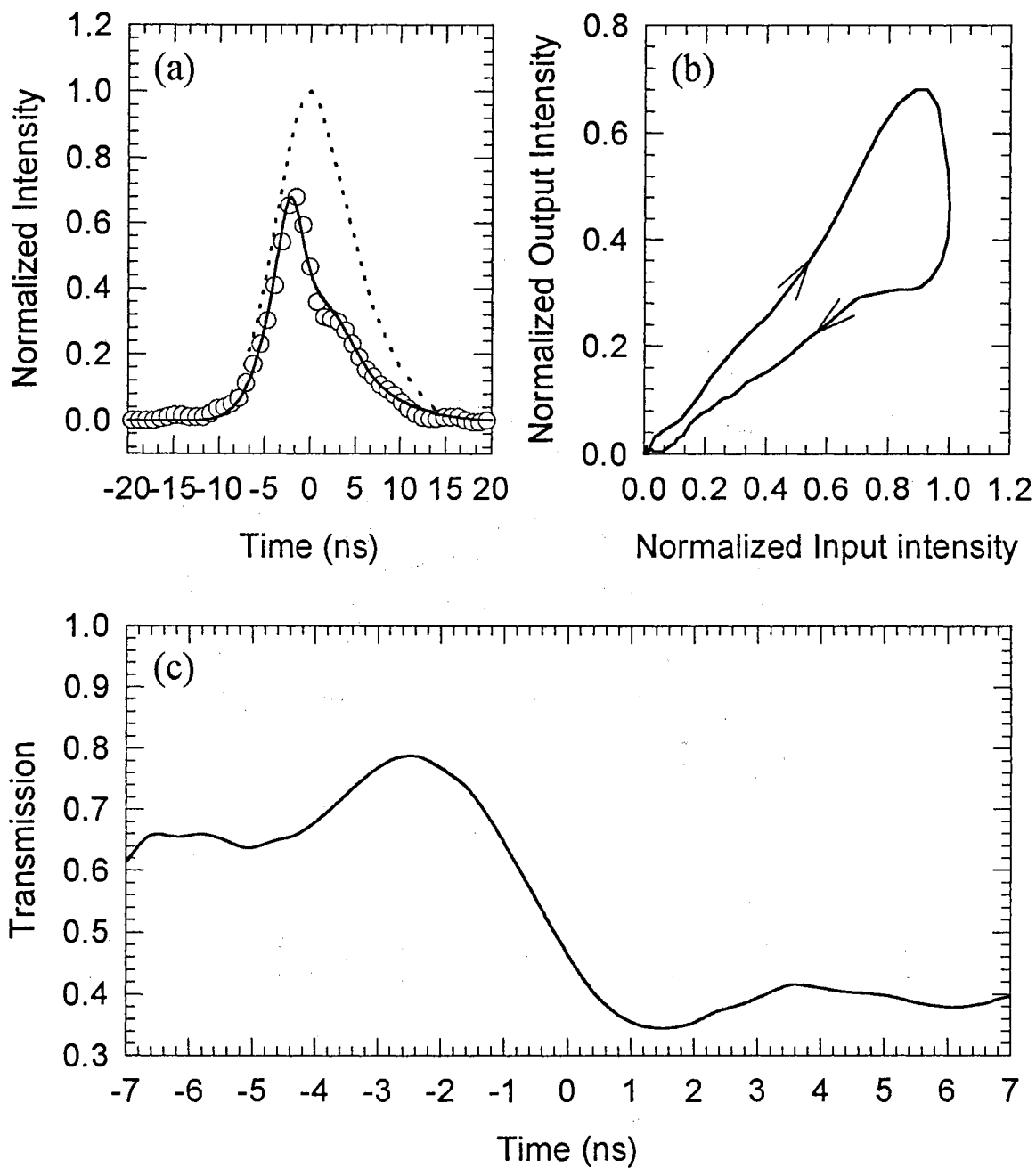


Figure III.5. Experimental and theoretical results for  $I_o=15.4$  MW/cm<sup>2</sup>,  $\phi_o=0.18\pi$  and  $F_F=3$ . The remaining parameters are the same as in Figure III.2. Notice the switching in the hysteresis loop. The switching times are  $\tau_{\uparrow}=1.6$  ns and  $\tau_{\downarrow}=2.2$  ns.

decreases linearly to zero. For the leading part of the signal, the etalon transmission is 0.5. The etalon then switches to a higher transmission of about 0.74 with a switching-up time of 2.8 ns. The transmission as a function of time shown in Figure III.6(c) resembles the step function behavior where the transmission is in one of two output states. Using the same initial detuning of Figure III.6 and  $I_0=17.7 \text{ MW/cm}^2$ , the results shown in Figure III.7 are obtained. The output temporal profile of Figure III.7(a) shows switching in the leading part of the pulse. The corresponding hysteresis loop indicates that the output intensity is almost constant for the range of the input intensities from  $10.6 \text{ MW/cm}^2$  to  $13.8 \text{ MW/cm}^2$  in the leading part of the pulse. When the input intensity of the trailing part of the signal is about  $17 \text{ MW/cm}^2$ , the output intensity starts to decrease. This Figure also shows optical switching. The transmission as a function of time, Figure III.7(c), shows that the transmission is low at the beginning and at the end of the pulse. At low input intensity the transmission is low, about 0.54. It then decreases to 0.47 with switching-down of  $\tau_{\downarrow}=1 \text{ ns}$  followed by switching-up of  $\tau_{\uparrow}=2 \text{ ns}$  after which the etalon transmission becomes 0.74. The etalon then switches down to 0.44 with  $\tau_{\downarrow} = 2.9 \text{ ns}$  and remains in this state.

## 5. Discussion

We attribute the cause of the switching to the nonlinear change in the index of refraction induced by the free carriers generated via the two-photon absorption process. The nonlinear refraction coefficient,  $\sigma_r$ , in Eq. (III.1) can be estimated by using one of two different band-filling theories. The first is based on the work done by Auston *et al.*[19] and the second is the dynamic Moss-

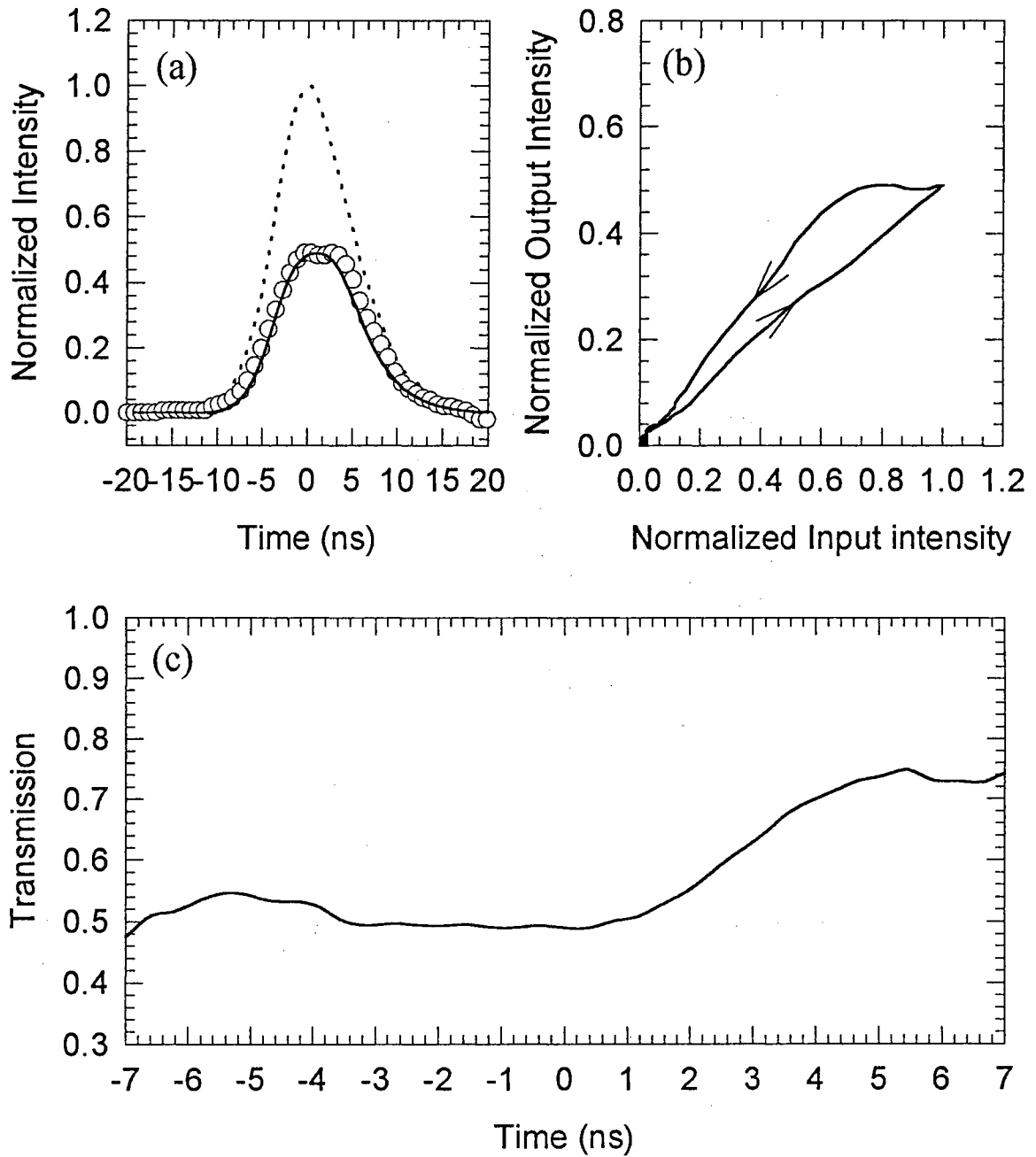


Figure III.6. Experimental and theoretical results for  $I_0=11.4 \text{ MW/cm}^2$ ,  $\phi_0=-0.24\pi$  and  $F_F=2$ . The remaining parameters are the same as in Figure III.2. Again a limiting action is shown in (a) for range of intensities different than those of Figure III.2. The hysteresis loop shows switching in the trailing part of the pulse. Under these conditions there is only switching from a low transmission to a high transmission state with  $\tau_{\uparrow}=2.8 \text{ ns}$ .



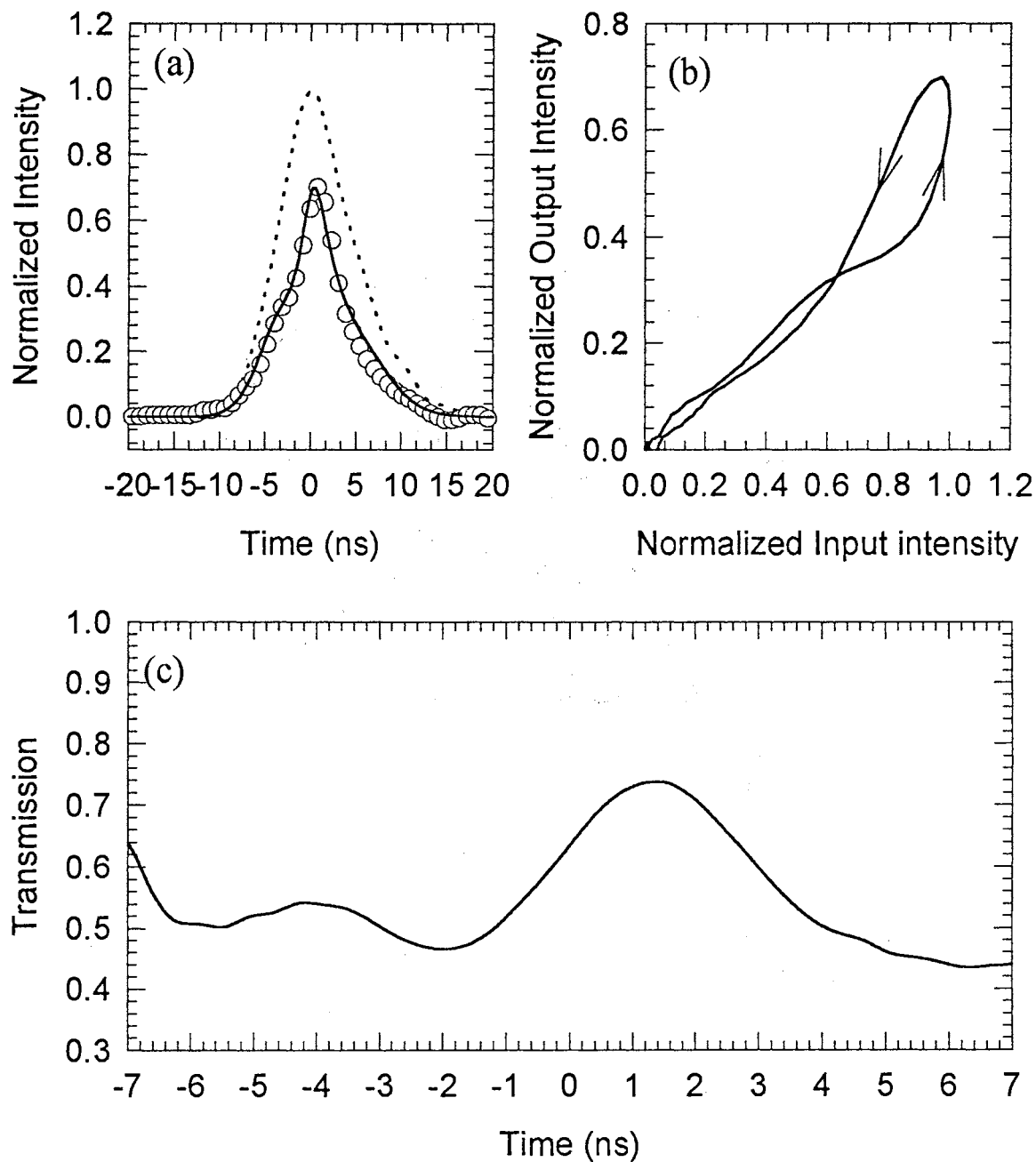


Figure III.7 Experimental and theoretical results for  $I_0=17.7$  MW/cm<sup>2</sup>,  $\phi_0=-0.24\pi$  and  $F_F=2$ . The remaining parameters are the same as in Figure III.2. In this case the hysteresis loop shows clear switching in the leading part of the single. The switching times are  $\tau_\uparrow=2$  ns and  $\tau_\downarrow=2.9$  ns.

Burstein model (DMBM) [31]. Based on the work done by Auston *et al.*, the change in the index of refraction due to the free carriers is given by  $\Delta n = \sigma_r N$ , where  $\sigma_r$  is given by Eq. II.18. In the discussion part of chapter II, we found  $\sigma_r = -6.2 \times 10^{-21} \text{ cm}^3$  which is very close to the result ( $\sigma_r = -6.0 \times 10^{-21} \text{ cm}^3$ ) obtained by fitting of the experimental results. This indicates that the change in the nonlinear refraction is due mainly to the electron-hole plasma generated by the TPA process. Said *et al.* [30] has modified the work done by Wherrett *et al.* [31] to be valid for the case of two-photon absorption. He found that both models gave the same value for  $\sigma_r$ .

The values of the parameters used in fitting the experimental results of the present work are the same values obtained earlier by us [58]. They are:  $n_o = 2.84$ ,  $\alpha_o = 0.3 \text{ cm}^{-1}$ ,  $\beta = 22 \text{ cm/GW}$ ,  $\sigma_{fc} = 25 \times 10^{-18} \text{ cm}^2$ ,  $\tau = 12 \text{ ns}$ , and  $\sigma_r = -6 \times 10^{-21} \text{ cm}^3$ . This seems to suggest that these values for the nonlinear parameters of CdTe at  $\lambda = 1.064 \text{ }\mu\text{m}$  are accurate. In our previous study (chapter II), we were able to predict the experimental results for different input intensities and different distances from the exit plane of the sample for both the spatial and temporal profiles. Similarly, in the present study, we are able to fit the experimental results of the transmitted temporal profiles for different input intensities and different initial detunings of the etalon. Moreover, the values of these nonlinear parameters are in good agreement with the most recent results in the literature [30, 23].

Another potential mechanism that could change the index of refraction is thermal heating. We estimate the nonlinear change due to thermal effects to be two orders of magnitude smaller than the change induced by the free carriers. To do this we assume a steady state condition for which the temperature any-

where inside the sample is the same. Of course, this assumption will overestimate the value of the change in the index of refraction. Following the same method used in reference [59] we find that for two-photon absorption the maximum change in the index of refraction caused by thermal heating is given by

$$\Delta n_{\max} \cong \frac{3}{8} \frac{\beta \tau_p I_o^2}{\rho C_v} \frac{dn}{dT}, \quad (\text{III.10})$$

where  $I_o$  is the peak input intensity,  $\beta = 22 \text{ cm/GW}$  is the two-photon absorption coefficient,  $\tau_p = 11 \text{ ns}$  is the pulse duration, and  $\rho$  and  $C_v$  are the density and specific heat of CdTe with the values  $5.852 \text{ g/cm}^3$  and  $0.044 \text{ cal/g } ^\circ\text{C}$ , respectively. Using the above equation with  $I_o = 20 \text{ MW/cm}^2$  and  $dn/dT = 11.75 \times 10^{-5} \text{ } ^\circ\text{C}^{-1}$  [27], we obtain  $\Delta n_{\max} = + 4 \times 10^{-6}$ . However, by using Eq. (III.4) with the value of  $\sigma_r$  given above, the maximum change in the index of refraction for  $I_o = 20 \text{ MW/cm}^2$  is  $-5 \times 10^{-4}$ . Again, the value obtained using Eq. (III.10) is larger than what it might be, even though it is much smaller than the change induced by the free photogenerated carriers. Moreover, this thermally induced change is positive while the result from Eq. (III.4) is negative. In our previous study [58] of the spatial and temporal profiles reshaping of nanosecond pulses emerging from CdTe samples, we showed that the dominant contribution to the change in the index of refraction was due to the free carriers generated via two-photon absorption. The spatial profile experienced self-defocusing, a clear indication of the negative change in the index of refraction. Moreover, in the present work the input intensities used were smaller than those used when we studied the reshaping effects.

## 6. Conclusion

The observation of all-optical switching in CdTe etalon at room temperature using nanosecond pulses at  $1.064 \mu\text{m}$  was reported. The input intensity required to achieve the switching was found to be dependent on the initial detuning of the etalon. Under different conditions, we were able to observe optical limiting action and pulse compression from the CdTe etalon. A model was developed whereby the origin of the nonlinearity was due to the free carriers generated by the two-photon absorption process. These carriers were found to induce a nonlinear change in the index of refraction that controlled the transmission of the etalon. Good agreement between the theoretical and the experimental results was found.

## CHAPTER IV

### LASER INDUCED TRANSIENT AND PERMANENT GRATING IN $\text{Eu}^{3+}$ -DOPED SILICATE GLASSES

#### 1. Introduction

Photoinduced permanent and transient refractive index gratings in rare-earth-doped ( $\text{Eu}^{3+}$ ,  $\text{Pr}^{3+}$ ) silicate, phosphate, and germanate glasses have been reported [1-7,60]. These gratings were formed and detected using the nondegenerate four-wave mixing technique. The transient component of the grating was attributed to a population grating while the permanent component was explained by a two-level system model based on a thermally induced change in the local environment of the rare-earth ions [4]. It has been proposed that the non-radiative relaxation of the excited state of the rare-earth ions create several high energy phonons resulting in a structural modification at the rare-earth ions sites. The results of Broer *et al.* [61,62] showed that the model mentioned above is not complete and that it does not explain their results. Broer *et al.* reported that all the  $\text{Pr}^{3+}$  -doped samples that they studied showed neither a transient nor a permanent grating. Moreover, some of the  $\text{Eu}^{3+}$  -doped samples exhibit only transient gratings. These results showed that the two-level system model is not complete and perhaps some other mechanism is responsible for creating the permanent grating in these glasses. For more details one can refer to Ref. [61].

In this chapter we report the FWM results in several of  $\text{Eu}^{3+}$ -doped silicate glasses. Some of these glasses contain dual alkaline modifiers (B16, B18, B20, B22, B24, and B26) and others are  $\text{Na}_2\text{O}$  enriched (B29, and B30). The scattered efficiency of these samples will be compared to determine the role of the divalent alkaline network modifiers and the effect of their relative concentrations on the grating formation. We use the results of the  $\text{Na}_2\text{O}$  enriched samples to understand the effect of the concentration of  $\text{Na}^+$  on the permanent grating formation. Also, the results describing the effect of the write-beams wavelength will be reported and discussed. A theoretical model was developed in order to determine the induced change in the index of refraction. This model considers the diffraction of a Gaussian probe beam from a volume grating formed by two intersecting Gaussian beams.

## 2. Experimental Setup

The experimental setup is shown in Figure IV.1. Nondegenerate FWM was used to measure the scattered efficiencies resulting from laser-induced gratings (LIG) in several  $\text{Eu}^{3+}$ -doped silicate glasses. LIG in these samples were formed by allowing two laser beams (write-beams) to intersect inside the sample with a crossing angle  $2\theta_w$ . The values of  $\theta_w$  that we used were  $1.9^\circ$ ,  $2.5^\circ$ , and  $3.25^\circ$  (measured in air). All experiments were performed using the output of cw Argon laser operating in the TEM<sub>00</sub> mode. The Gaussian profile of the beam was confirmed by using a laser beam profiler. The  $\text{Eu}^{3+}$  ions were excited to the  $^5\text{D}_2$  level by the 465.8 nm laser line of the Argon laser. The write-beams were obtained by splitting the main laser output beam into two beams. By using two mirrors these beams were redirected to cross each other at the location of the

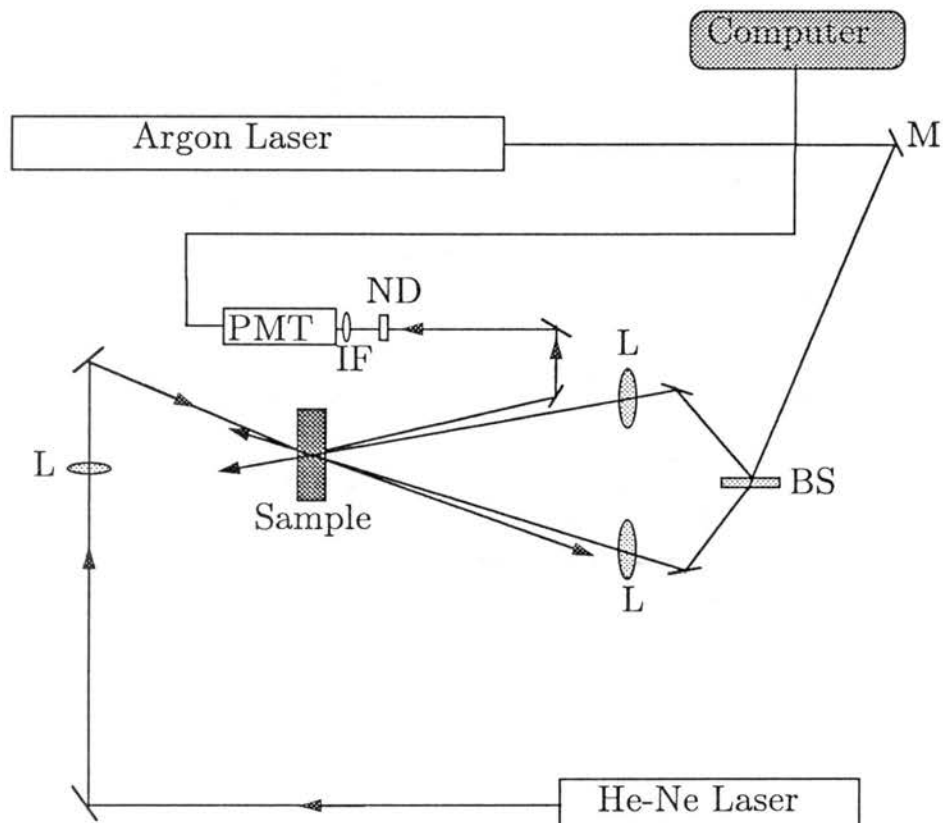


Figure IV.1. The FWM experimental setup. The symbols are: M- mirror, L- lens, PMT- photomultiplier tube, ND- neutral density filter, IF- interference filter, and BS- beam splitter.

sample. The optical path lengths of the write-beams are equal to within the coherence length of the laser. The write-beams were focused using two lenses each of which had a 50 cm focal length. The spot size of each beam was  $w_w=100 \mu\text{m}$  that corresponds to a Rayleigh range of 6.7 cm (in air). The total power of the write-beams was in the range 8 mW to 60 mW. In order to form a grating perpendicular to the front and back surfaces of the sample, the reflection of each write-beam should be antiparallel to the incident direction of the other. For this purpose the sample was placed on a mount that could be rotated and tilted.

To determine the existence of the LIG, we used the output of a He-Ne laser operating at 632.8 nm. We will refer to this beam as the read (probe) beam. The read-beam wavelength was selected to be different than that of the write-beams in order to make the detection of the scattered signal easier. The read-beam was counter propagating along one of the write-beams (see Figure IV.1) with a small angle between them ( $\theta_r-\theta_w$ ). The probe beam was focused such that its spot size at the position of the sample was about  $100 \mu\text{m}$ . In order to get the maximum scattering efficiency, the read beam was incident on the sample surface with an angle  $\theta_r$  so that the Bragg condition was satisfied.  $\theta_r$  is defined relative to the normal of the sample surface. The power of the read beam at the sample surface was 4.3 mW.

The scattered signal (beam) was detected by a Hamamatsu R1547 photomultiplier tube (PMT) coupled to a personal computer. An interference filter at 632.8 nm was placed directly in front of the PMT to prevent any stray Argon light and sample fluorescence from being detected with the diffracted signal. In order to get absolute values for the power of the scattered beam, we calibrated



the output of the PMT voltage using different neutral density filters and a known power of the He-Ne laser. This calibration gave us a relation between the laser power detected by the PMT and its output voltage. By measuring the PMT output voltage we were able to obtain the scattered power in absolute units.

### 3. Theory

#### (a) Plane Wave Approximation

When a plane wave is incident on a uniform grating the diffracted efficiency is given by [63].

$$\eta = \exp\left(\frac{\alpha_r L}{\cos(\theta_r)}\right) \left\{ \left[ \sin\left(\frac{\pi L \Delta n}{\lambda_r \cos(\theta_r)}\right) \right]^2 + \left[ \sinh\left(\frac{\pi L \Delta \alpha}{4 \cos(\theta_r)}\right) \right]^2 \right\}. \quad (\text{IV.1})$$

Here  $L$  is the grating thickness,  $\alpha_r$  is the absorption coefficient of the read wave (probe wave), and  $\theta_r$  is the angle between the read beam and the normal to the grating surface. In the above equation  $\Delta n$  and  $\Delta \alpha$  are the average nonlinear changes in the index of refraction and the absorption coefficient, respectively.

Experimentally, plane waves can be achieved by expanding the laser beam and then selecting the central part of the beam using an aperture. However, a considerable amount of laser power will be lost. In most cases, the resultant weak plane wave cannot be used experimentally. In practice, we use (most of the time) Gaussian laser beams in performing experiments that involve light-matter interactions. For such cases the above result can be applied only if the following conditions are satisfied [63].

- 1) The width of the interaction region must be large compared to the spatial period of the grating,  $\Lambda$ , ( $w_w \gg \Lambda$ ). This limits the degree of focusing of the write-beams.
- 2) The grating thickness (the overlap length of the write-beams) must be larger than the sample thickness,  $d$ . i.e.,  $[2w_w/\tan(\theta_w)] \gg d$  where  $\theta_w$  is the crossing angle. When  $[2w_w/\tan(\theta_w)] \gg d$ , the grating volume within the sample is uniform like that generated by two-plane waves.
- 3) The attenuation due to the absorption of the write-beams,  $\alpha_w$ , must be very small. i.e.,  $\alpha_w d \ll 1$ . This also affects the uniformity of the grating inside the sample. If the absorption of the write-beams is not negligible then the grating will not be uniform at different points throughout the sample.
- 4) The read-beam spot size should be much larger than that of the write-beam. i.e.,  $w_r \gg w_w$ . This is a necessary condition for the read-beam to satisfy the plane wave approximation. When  $w_r \gg w_w$ , the central portion of the read-beam will interact with the grating volume. This indicates that most of the read-beam power will not be used in the scattering process.

However, when we study the grating formation and the scattering efficiency, we encounter experimental conditions that will not satisfy the above conditions. In such cases we cannot use the plane wave approximation formula to analyze the experimental results. This suggests that we should develop a model for the scattered efficiency that takes into consideration the real nature of the laser beam. In the following section we deal with the grating formation and the scattering efficiency for the case of Gaussian beams.

## (b) Gaussian Beams

We investigate the scattering efficiency of a Gaussian probe beam (read-beam) from a weak volume grating formed by two-crossed Gaussian beams (write-beams). The analysis will be carried out for small crossing angles,  $2\theta \ll 1$  radian. In our analysis we consider the case where the center of the volume grating is at the origin of the coordinate system and is located in the middle of the medium (see Figure IV.2).

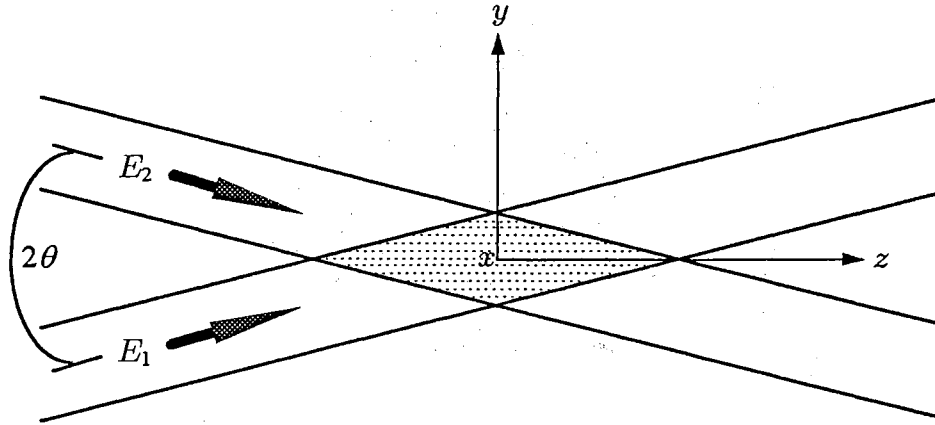


Figure IV.2. The diagram shows two intersecting Gaussian beams which create a volume grating pattern. The  $x$ -direction is pointing into the page. Each beam makes an angle  $\theta$  with the  $z$ -axis in the  $y$ - $z$  plane.

In general we write the electric field of a Gaussian beam in the  $q$ -parameter formalism as

$$E = E_0 \frac{q_0}{q(z')} \exp \left[ -ik \left( \frac{\rho^2}{2q(z')} \right) - i(kz' - \omega t) \right], \quad (\text{IV.2})$$

where  $E_0$  is the field amplitude,  $\rho^2 = x'^2 + y'^2$ ,  $q(z') = q_0 + z'$ ,  $q_0 = i\pi w_0^2 / \lambda$ , and  $w_0$  is the beam spot size. The prime coordinates represent the coordinate system of each individual beam. For a beam propagating at a small angle,  $\theta$ ,

with respect to the  $z$ -axis in the  $y$ - $z$  plane, we have the following transformation of the coordinate system

$$x' \rightarrow x, \quad y' \rightarrow y - y \frac{\theta^2}{2} - z\theta, \quad \text{and} \quad z' \rightarrow z - z \frac{\theta^2}{2} + y\theta. \quad (\text{IV.3})$$

In the above equation, we used the approximations  $\sin(\theta) \approx \theta$ , and  $\cos(\theta) \approx 1 - (\theta^2/2)$ . By substituting Eq. (IV.3) into the electric field expression of Eq. (IV.2) and using the approximation  $y \ll z$  and  $\theta \ll 1$ , we obtain

$$E = E_o \frac{q_o}{q(z)} \exp \left[ -ik \left( \frac{x^2 + (y - z\theta)^2}{2q(z)} + y\theta - z \frac{\theta^2}{2} \right) - i(kz - \omega t) \right]. \quad (\text{IV.4})$$

If the length of the overlap region between the two interacting Gaussian beams ( $l_{int} \approx w_o/\theta$ ) is smaller than the Rayleigh range ( $\pi w_o^2/\lambda$ ) then we can assume  $q(z) \approx q_o$  which leads to the following result for the electric field.

$$E = E_o \exp \left[ -\frac{x^2 + (y - z\theta)^2}{w_o^2} - ik \left( y\theta - z \frac{\theta^2}{2} \right) - i\phi \right], \quad (\text{IV.5})$$

where  $\phi = kz - \omega t$ . Define  $E_1$  and  $E_2$  to be the electric fields of the two write-beams which make an angle  $\theta_w$  and  $-\theta_w$  with the  $z$ -axis, respectively. Then from Eq. (IV.5), we obtain

$$E_1 = E_{1o} \exp \left[ -\frac{x^2 + (y - z\theta_w)^2}{w_{1w}^2} - ik \left( y\theta_w - z \frac{\theta_w^2}{2} \right) - i\phi \right] \quad (\text{IV.6})$$

and

$$E_2 = E_{2o} \exp \left[ -\frac{x^2 + (y + z\theta_w)^2}{w_{2w}^2} + ik \left( y\theta_w + z \frac{\theta_w^2}{2} \right) - i\phi \right] \quad (\text{IV.7})$$

Assume that  $E_{1o} = E_{2o} = E_o$  and  $w_{1w} = w_{2w} = w_w$  then the intensity of the grating pattern of the two Gaussian beams is

$$I(x, y, z) = \frac{1}{4}(E_1 + E_2)(E_1^* + E_2^*) \quad (\text{IV.8})$$

which yields the following result

$$I(x, y, z) = \frac{I_o}{2} \left[ \cos(2ky\theta_w) + \cosh(4yz\theta_w / w_w^2) \right] \exp\left(-2 \frac{\rho^2 + z^2\theta_w^2}{w_w^2}\right). \quad (\text{IV.9})$$

Here  $I_o$  is the peak intensity. In the above equation, the cosine term is responsible for the modulation (oscillation) of the intensity pattern as  $y$  is varied. The cosine-hyperbolic term controls the superposition (degree of overlap) of the two intersecting beams in the  $z$ -direction. The exponential term represents a Gaussian envelop in three-dimension. The second term in the exponential causes the intensity to decrease as the absolute value of  $z$  increases. In other words, this term attenuates the intensity of the fringe pattern in the  $z$ -direction. Notice that the maximum value of  $I(x, y, z)$  is at the origin and that the interference pattern is symmetric about the origin. Figure IV.3 shows typical results of the intensity pattern in the  $yz$  plane as described by Eq. (IV.9). From the cosine term, we find that the spacing of the fringes is  $\Lambda = \lambda/2\theta_w$  which is usually given by  $\Lambda = \lambda/2\sin(\theta_w)$  [63] if the small angle approximation is not considered.

We are interested in finding the scattered efficiency of the probe beam (read-beam) that makes an angle  $\theta_r$  with respect to the  $-z$ -axis when incident upon the volume grating. The scattered (diffracted) beam makes an angle  $\theta_r$  with the  $z$ -axis. For this case one of the four terms in Eq. (IV.8) contributes to the scattering efficiency. In fact, the term of interest is  $E_1 E_2^*$  which has a phase variation  $\exp(-i2k_w y \theta_w)$  that satisfies the Bragg condition. The phase variations of the incident and the scattered beams are  $\exp(ik_r y \theta_r)$  and  $\exp(-ik_r y \theta_r)$ , respectively. In the last three expressions we used the subscripts  $w$  and  $r$  with  $k$  to

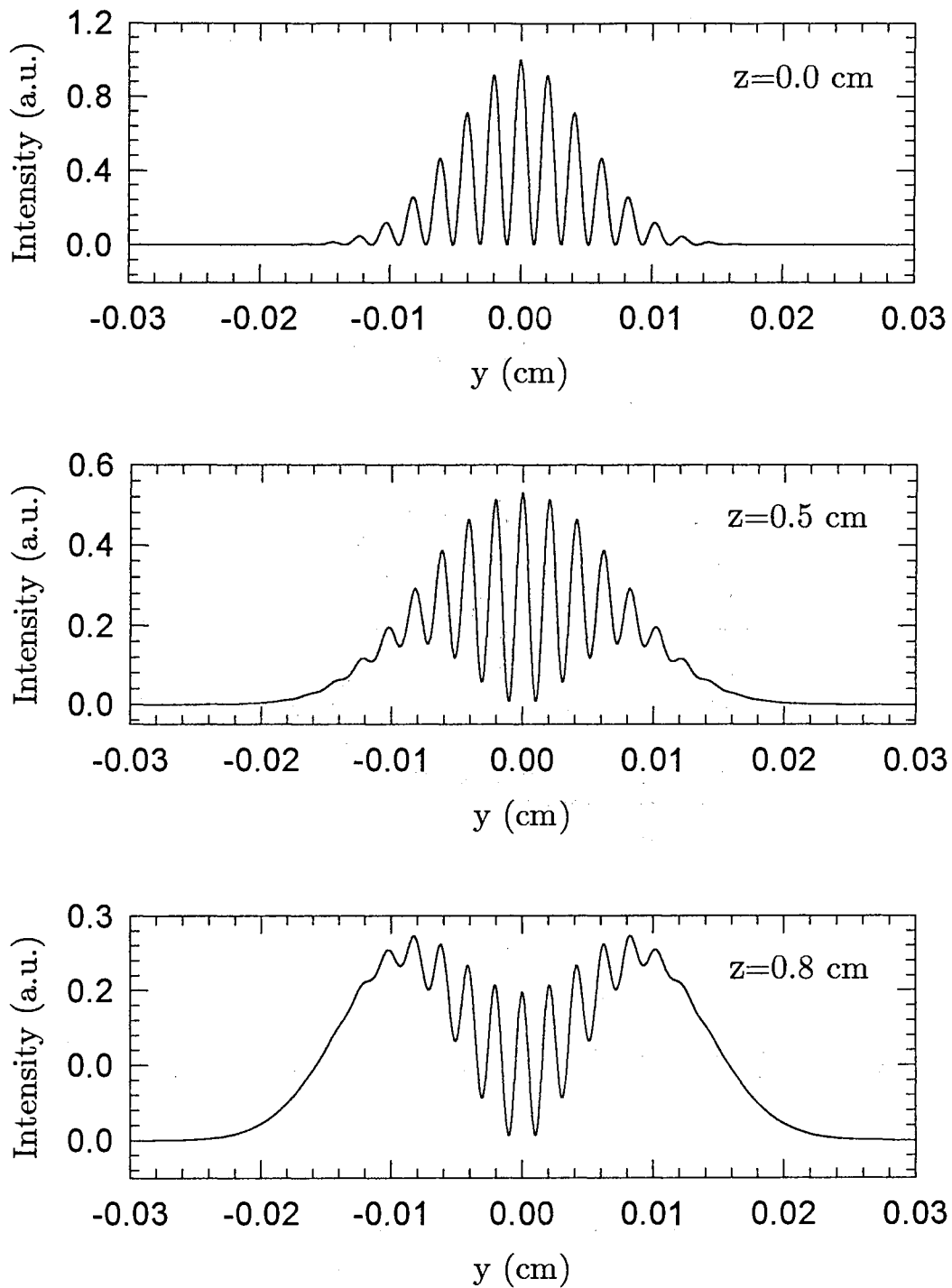


Figure IV.3. The interference intensity pattern of the two-crossed beams at different positions along the  $z$ -direction.  $w_w=0.01$  cm,  $\theta_w=1^\circ$  (in air), and  $x=0$ .

differentiate between the write-beam wavelength and that of the read-beam. From these expressions we find that  $k_w \theta_w = k_r \theta_r$  which is the Bragg condition allowing the diffraction to take place. This conclusion will be clear from the results below. Let us define the normalized modulated intensity pattern of interest as  $M(x,y,z) = (1/4 |E_o|^2) E_1 E_2^*$  which can be expressed as

$$M(x, y, z) = \frac{1}{4} \exp\left(-2 \frac{x^2 + y^2 + z^2 \theta_w^2}{w_w^2} - i2k_w y \theta_w\right) \quad (\text{IV.10})$$

Equation (IV.10) shows that the envelop of the grating pattern is a three-dimensional Gaussian distribution.

Consider that the grating created by the write-beams is a purely real, phase grating, then we write the index of refraction of the medium as

$$n(x, y, z) = n_o + \frac{1}{2} n_o \chi_m M(x, y, z) = n_o + \Delta n_m M(x, y, z) \quad (\text{IV.11})$$

where  $n_o$  is the linear index of refraction,  $\chi_m$  is the maximum nonlinear change in the dielectric constant, and  $\Delta n_m$  is the maximum change in the nonlinear index of refraction given by  $\Delta n_m = (1/2) n_o \chi_m$ . The nonlinear polarization as a result of the read-beam impinging on the grating volume in the  $-\theta_r$  direction is given by

$$P(x, y, z) = \frac{2\varepsilon \Delta n_m}{n_o} M(x, y, z) E_r(x, y, z). \quad (\text{IV.12})$$

In the above equation  $\varepsilon$  is the permittivity of the medium and  $E_r(x,y,z)$  is the electric field of the read-beam which has the same mathematical form of Eq. (IV.7). Because of absorption the function  $M(x,y,z)$  will not be symmetric on both sides of the origin and as a result the modulation at two identical points to

the right and to the left of the origin will not be the same. Therefore, it is necessary to include the absorption of the write-beams in the expression of  $M(x,y,z)$ . This means that  $M(x,y,z)$  should be multiplied by  $\exp\{-\alpha_w[z + (L/2)]\}$ . Also, to include the absorption of the read-beam we multiply  $E_r(x,y,z)$  by  $\exp\{-(\alpha_r/2)[z - y\theta_r + (L/2)]\}$ . In the last two expressions  $L$  is the sample thickness and  $\alpha_w$  and  $\alpha_r$  are the linear absorption coefficients of the read-beam and the write-beams, respectively. The polarization then can be written as

$$P(x,y,z) = \frac{\Delta n_m \varepsilon E_{r0}}{2n_o} \exp\left(\frac{-\alpha L}{2}\right) \exp\left(-2\frac{\rho^2 + z^2\theta_w^2}{w_w^2} - \frac{x^2 + (y + z\theta_r)^2}{w_r^2}\right) \times \exp\left(-\alpha z + \frac{\alpha_r\theta_r y}{2}\right) \exp\left(-i(2k_w\theta_w - k_r\theta_r)y + i\frac{k_r\theta_r^2 z}{2} - i\phi\right) \quad (\text{IV.13})$$

In the above equation  $\alpha = \alpha_w + \alpha_r/2$ . From the expression  $\exp[-i(2k_w\theta_w - k_r\theta_r)y]$  it is clear that the scattered beam should be in the  $\theta_r$  direction in order for the phase matching condition of Bragg scattering to be satisfied. Then  $k_w\theta_w = k_r\theta_r$  is the Bragg condition for the scattering to take place as mentioned before. This means that the Bragg scattered beam makes an angle  $\theta_r$  with the positive  $z$ -axis.

In order to find the scattered electric field  $E_s(x,y,z)$ , we use the paraxial wave equation with  $P(x,y,z)$  as a source term. Then the nonlinear wave equation in the medium reads

$$\nabla_T^2 E_s(x,y,z) - i2k_r \frac{\partial E_s(x,y,z)}{\partial z} = -\omega_r^2 \mu P(x,y,z). \quad (\text{IV.14})$$

$\nabla_T^2$  represents the transverse Laplacian given by  $\nabla_T^2 = \partial^2 / \partial x^2 + \partial^2 / \partial y^2$  in rectangular coordinates.  $\omega_r$  is the angular frequency of the read-beam and  $\mu$  is



the permeability of the medium. In arriving at Eq. (IV.14) we used the slowly-varying-amplitude approximation i.e., we assume that the variation of  $E_s(x,y,z)$  with  $z$  occurs only over distances much larger than an optical wavelength. Because of the complexity of  $P(x,y,z)$ , Eq. (IV.14) can be solved by either direct use of numerical methods or by the use of Green's-function integral which in turn can be solved either analytically or numerically depending on the exact form of  $P(x,y,z)$  and the limits of the integral. By using the Green's-function integral method, the solution of Eq. (IV.14) can be expressed as

$$E_s(x, y, z) = -\omega_r^2 \mu \iiint P(x', y', z') G(\vec{r}', \vec{r}) dx' dy' dz' \quad (\text{IV.15})$$

where  $G(\vec{r}', \vec{r})$  is the Green's-function which is a solution to the homogeneous paraxial Helmholtz wave equation  $(\partial^2 / \partial x^2) + (\partial^2 / \partial y^2) - i2k_r(\partial / \partial z) = 0$ . It is very well known that one of the solutions for this equation is the paraboloidal wave

$$U(x, y, z) = \frac{1}{z} \exp\left(ik_r \frac{x^2 + y^2}{2z}\right) \quad (\text{IV.16})$$

which is the paraxial approximation of the spherical wave. Therefore,  $G(\vec{r}', \vec{r})$  can be written as

$$G(\vec{r}', \vec{r}) = \frac{1}{4\pi(z' - z)} \exp\left(i \frac{\pi}{\lambda_r} \frac{(x' - x)^2 + (y' - y)^2}{(z' - z)}\right) \quad (\text{IV.17})$$

If we ignore the absorption due to both the write- and the read-beams then one can find a closed form for  $E_s(x,y,z)$  by taking the limit as  $z \rightarrow \infty$  after which the three integrals can be evaluated as infinite Gaussian integrals. Of course, this case can be applied only when the volume grating is completely contained within the medium. This has been done for the case where the sample thickness is

larger than the volume grating length ( $2w_w/\theta_w$ ) [64]. However, experimentally we often investigate samples that only contain part of the volume grating. In such a case, we should integrate over  $z'$  from  $-L/2$  to  $L/2$ . In practice the absorption of both the write- and the read-beams should be included in order to fairly compare the scattering efficiencies of samples with different thicknesses. Even in this case the integrals over  $x'$  and  $y'$  still can be evaluated  $-\infty$  to  $\infty$  from which a closed form results. However, the integral over  $z'$  has to be evaluated numerically since the limits of the integral are  $-L/2$  and  $L/2$ . In order to solve Eq. (IV.15), we need to rewrite it in the following form

$$E_s(x, y, z) = \frac{-\omega_r^2 \mu \varepsilon \Delta n_m E_{r0} e^{-(aL/2)}}{8\pi n_r} \int_{-L/2}^{L/2} F(x, y, z, z') dz' \quad (\text{IV.18})$$

where

$$F(x, y, z, z') = F_{x'}(x, z, z') F_{y'}(y, z, z') \frac{1}{z' - z} \times \exp\left(-\frac{2z'^2 \theta_w^2}{w_w^2} - \frac{z'^2 \theta_r^2}{w_r^2} - \alpha z' + i \frac{k_r}{2} z' \theta_r^2\right) \quad (\text{IV.19})$$

In Eq. (IV.19)  $F_{x'}(x, z, z')$  and  $F_{y'}(y, z, z')$  represent the integrals over  $x'$  and  $y'$ , respectively. Below we give the results of these integrals.

$$F_{x'}(x, z, z') = e^{ibx^2} \int_{-\infty}^{+\infty} \exp[-(a - ib)x'^2 - i2bx'x'] dx' \quad (\text{IV.20})$$

$$= e^{ibx^2} \sqrt{\frac{\pi}{a - ib}} \exp\left(\frac{-b^2 x^2}{a - ib}\right) = \sqrt{\frac{\pi}{a - ib}} e^{(-A_2 + iA_3)}$$

where  $a = (2/w_w^2) + (1/w_r^2)$ ,  $b = [\pi/\lambda_r(z' - z)]$ ,  $A_2 = (ab^2 x^2/A_1)$ ,  $A_3 = (ba^2 x^2/A_1)$ , and  $A_1 = a^2 + b^2$ .

$$\begin{aligned}
F_{y'}(y, z, z') &= e^{iby^2} \int_{-\infty}^{+\infty} \exp[-(a-ib)y'^2 + (d+ic)y'] dy' \\
&= e^{iby^2} \sqrt{\frac{\pi}{a-ib}} \exp\left[\frac{(d+ic)^2}{4(a-ib)}\right] = \sqrt{\frac{\pi}{a-ib}} e^{(B_2+iB_1)}
\end{aligned} \tag{IV.21}$$

Here  $d=[(\alpha_r\theta_r/2)-(2\theta_r z'/w_r^2)]$ ,  $c=(k_r\theta_r-2k_w\theta_w-2by)$ ,  $B_1=by^2+\{2acd+[b(d^2-c^2)/4A_1]\}$ , and  $B_2=\{[a(d^2-c^2)-2bcd]/4A_1\}$ . If we combine Eqs.(19) and (20) we obtain

$$F_x, F_{y'} = \frac{\pi}{A_1} (a+ib) \exp[B_2 - A_2 + i(B_1 + A_3)] \tag{IV.22}$$

Then by using Eqs. (IV.18), (IV.19), and (IV.22), the scattered field can be written as

$$E_s(x, y, z) = \frac{-\omega_r^2 \mu \varepsilon \Delta n_m E_{r0} e^{-(aL/2)}}{8n_r} (\mathcal{E}_R + i\mathcal{E}_I) \tag{IV.23}$$

where  $\mathcal{E}_R$  and  $\mathcal{E}_I$  are the real and the imaginary parts of the integration over  $z'$  given by

$$\mathcal{E}_R = \int_{-L/2}^{L/2} \frac{(a \cos(S_3) - b \sin(S_3))}{A_1(z' - z)} e^{S_2} dz' \tag{IV.24}$$

and

$$\mathcal{E}_I = \int_{-L/2}^{L/2} \frac{(b \cos(S_3) + a \sin(S_3))}{A_1(z' - z)} e^{S_2} dz' \tag{IV.25}$$

$S_2$  and  $S_3$  in the last two equations are given by  $S_2=B_2-A_2-Sz'^2-\alpha z'$  and  $S_3=B_1+A_3+S_1z'$ , where  $S=[2(\theta_w/w_w)^2-(\theta_r/w_r)^2]$  and  $S_1=(1/2)kr\theta_r^2$ . Now, we should be able to get a value for the scattered field by methods of numerical evaluation of Eqs. (IV.24) and (IV.25). But our aim is to find the scattering efficiency of the grating. To do so we need to find the scattered power which is defined as

$$P_s = \frac{1}{2} \sqrt{\frac{\varepsilon}{\mu}} \int_{-\infty}^{+\infty} \int_{-\infty}^{+\infty} E_s E_s^* dx dy \tag{IV.26}$$

Because the incident power of the read-beam is  $P_r = (\pi w_r^2 E_{r0}^2 / 4 \sqrt{\mu / \epsilon})$  the scattering efficiency of the grating is given by

$$\eta = \frac{P_s}{P_r} = \frac{2}{\pi w_r^2 E_{r0}^2} \int_{-\infty}^{+\infty} \int_{-\infty}^{+\infty} E_s E_s^* dx dy \quad (\text{IV.27})$$

From Eqs. (IV.27) and (IV.23) and by using  $\mu\epsilon = (2\pi/\lambda_r \omega_r)^2$ , the final expression of the scattering efficiency of the volume grating is

$$\eta = \frac{\pi^3}{2} \left( \frac{\Delta n_m e^{-\alpha L/2}}{n_r w_r \lambda_r^2} \right)^2 \iint (\mathcal{E}_R^2 + \mathcal{E}_I^2) dx dy. \quad (\text{IV.28})$$

It is important to note that  $\eta$  is not simply proportional to  $1/w_r^2$  or  $1/\lambda_r^4$  since the function inside the integral does not explicitly show the  $w_r$  and  $\lambda_r$  dependence.

In order to determine  $\Delta n_m$  all we need to know is the experimental value for  $\eta$ . By using the above result one can find how the efficiency of the grating is changing as a function of sample thickness, write-beam crossing angle, read-beam wavelength, and the ratio of the read-beam spot size to that of the write-beam.

#### 4. Results

##### (a) Results of the Theoretical Model

By using the theory developed in the previous section, one can determine how the scattered efficiency will behave as a function of the crossing angle, the sample thickness, and the read beam wave length. Most of the time we are in-

terested in classifying samples according to their scattering efficiency. However, this task becomes difficult if the thicknesses of these samples are different. In such case we cannot compare these samples by direct comparison of their efficiencies; rather we need to find the nonlinear change in the index of refraction, for each sample, which is another mechanism in comparing samples. In this section, we show some theoretical results using the theory of the previous section in addition to experimental verification of the theory. Two samples of the same composition will give different values for the efficiency if they have different thicknesses. However, the corresponding change in the index of refraction,  $\Delta n$ , should be the same in both samples. This can be used as a tool to check the prediction of the theory. For this purpose, we measured the scattered efficiency of four samples that have different thicknesses. Samples B16CS and B16SQ have the same composition (the compositions are listed in Table IV.2) as do samples B24CS and B24SQ, although different from that of the first set.  $\Delta n$  for these samples are shown in Table IV.1. As we expect the change in the index of refraction induced in each pair is very much the same. Also, for each sample that we have studied we found that  $\Delta n$  is basically the same regardless of the crossing angle. This is to be expected, because the value of  $\Delta n$  that we are calculating is the maximum value at the center of the crossing beams and at the center of the grating. This result is further evidence that the model is predicting the results accurately. To continue checking the theoretical model, we calculated the scattered efficiency as a function of  $\theta_w$  for different samples. The theoretical results and the corresponding experimental ones are shown in Figure IV.4. It is clear that the results are in very good agreement.

Table IV.1. Experimental result for B16CS, B16SQ, B24CS, and B24CS using  $P_w=28$  mW and  $\theta_w=1.9^\circ$ .

Sample	$L_S$ (mm)	$\eta$ ( $\times 10^{-6}$ )	$(\eta/\Delta n^2)$ ( $\times 10^{+6}$ )	$\Delta n$ ( $\times 10^{-6}$ )
B16CS	6.52	8.14	2.33	1.87
B16SQ	1.62	2.49	0.72	1.86
B24CS	7.24	65.8	1.88	5.92
B24SQ	4.18	64.0	1.92	5.78

From our model we can predict how the efficiency varies as a function of sample thickness. Figure IV.5 shows the results for two cases. In one case the absorption is zero and the other case the absorption is not zero. Notice that the model predicts the  $L_S^2$  dependence of the efficiency for sample thicknesses ( $L_S$ ) much smaller than the grating thickness ( $L_G$ ). This kind of result is predicted by the plane wave approximation [Eq. (IV.1)] for the scattered efficiency. For the case where the absorption is zero the scattered efficiency increases linearly then it starts to saturate as  $L_S$  becomes comparable to  $L_G$  and it becomes constant for  $L_S > L_G$  as expected. However, for the case where the absorption is considered, the efficiency increases until  $L_S$  reaches a critical value after which the efficiency starts to decrease. The value of  $L_S$  depends on the absorption coefficient and the grating thickness. This clearly shows that the model can be used to estimate the optimum sample thickness required to give the maximum scattered efficiency.

The intensity profile of the scattered beam can be predicted using our model. For  $w_w = w_r$  and  $\lambda_w \neq \lambda_r$  we found that the scattered beam could have

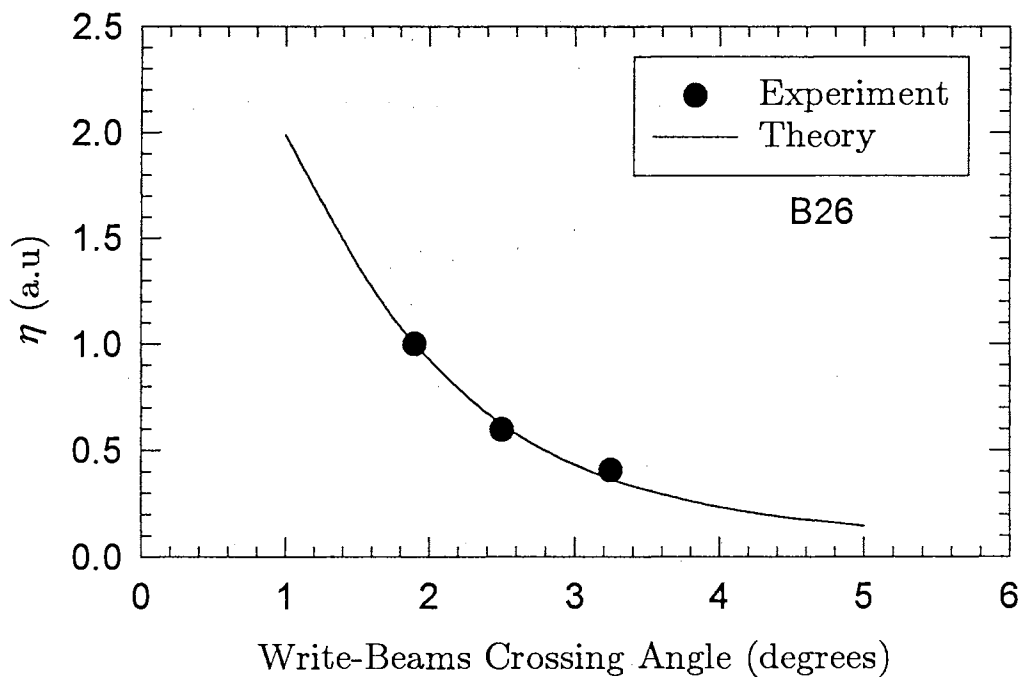
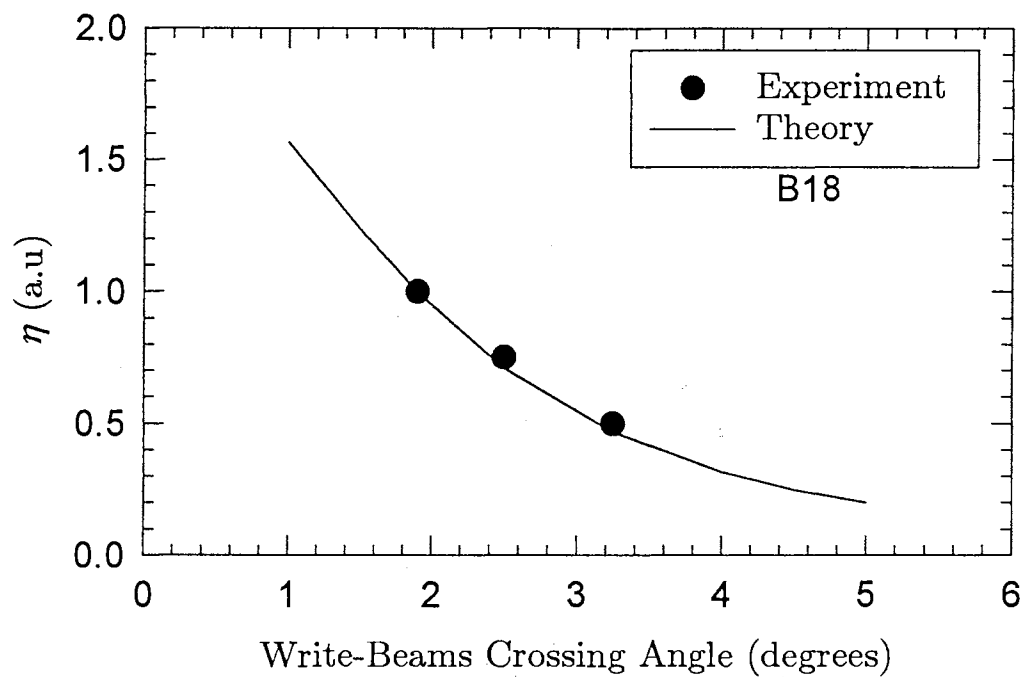


Figure IV.4. Theoretical ( lines) and experimental (dark circles) scattered efficiencies for B18 and B26 using different crossing angles. The normalization was done by dividing the results by the value of  $\eta$  at  $\theta_w=1.9^\circ$ .

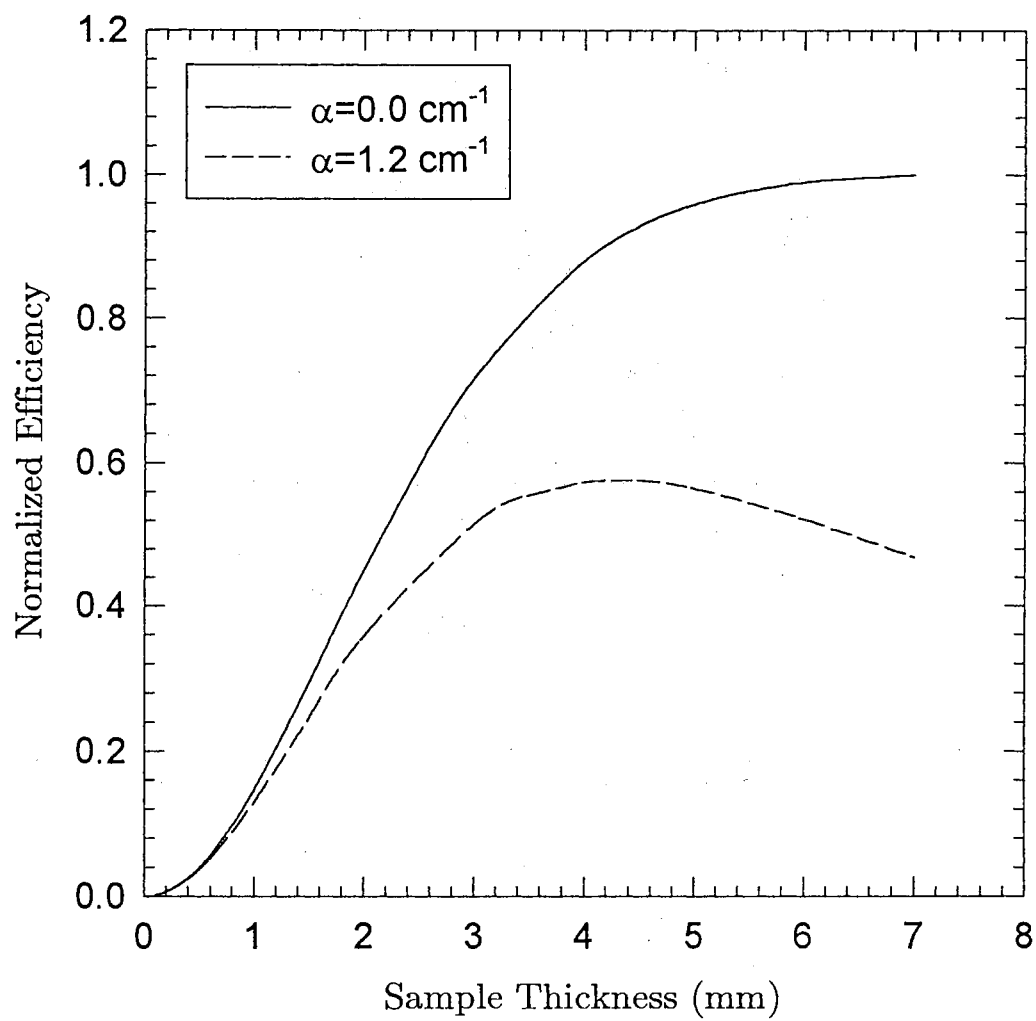


Figure IV.5. Scattered efficiency as a function of sample thickness. The following parameters were used in getting these results:  $w_w = w_r = 0.01 \text{ cm}$ ,  $n_w = 1.57$ ,  $n_r = 1.55$ , and  $\theta_w = 1.9^\circ$ .



either a circular or an elliptic Gaussian profile depending on the relative values of  $L_S$  and  $L_G$ . For samples with  $L_S \ll L_G$  the scattered beam profile was found to be the same as that of the incident beam. Basically if the incident beam is circular Gaussian the diffracted beam will be a circular Gaussian as well. If  $L_S$  is comparable or larger than  $L_G$  the scattered beam will have an elliptic Gaussian profile. In fact, this is what we observed experimentally because  $L_S$  is comparable to  $L_G$  for most of the samples that were studied. For degenerate FWM ( $\lambda_w = \lambda_r$ ) our model shows that the scattered beam profile is independent of the relative values of  $L_S$  and  $L_G$  as far as  $w_w = w_r$ . Figure IV.6 shows the contour plots corresponding to the scattered beam profiles for different conditions. The diagrams shown in Figure IV.7 help understanding the results of the diffracted beam profile. For the case where  $L_S \ll L_G$ , all the diffracted energy stays within the boundary of the beam while the read-beam interacts with the grating region, see Figure IV.7(a). When  $L_S$  is comparable to  $L_G$ , the diffracted energy from the input end of the grating region will walk out of the read-beam before it (the read-beam) completes its interaction with the grating region. The difference in the diameter of the read-beam and the diffracted beam in the  $y$ -direction is  $\Delta y$ , see Figure IV.7(b). This difference is what causes the diffracted beam to have the elliptic profile. The degenerate FWM case is shown in Figure IV.7(c). The scattered energy stays within the boundaries of the probe beam regardless of the thickness of the sample.

#### (b) Experimental Results

To study the LIG, we performed different measurements using a variety of glass samples and different experimental conditions. The identity of the

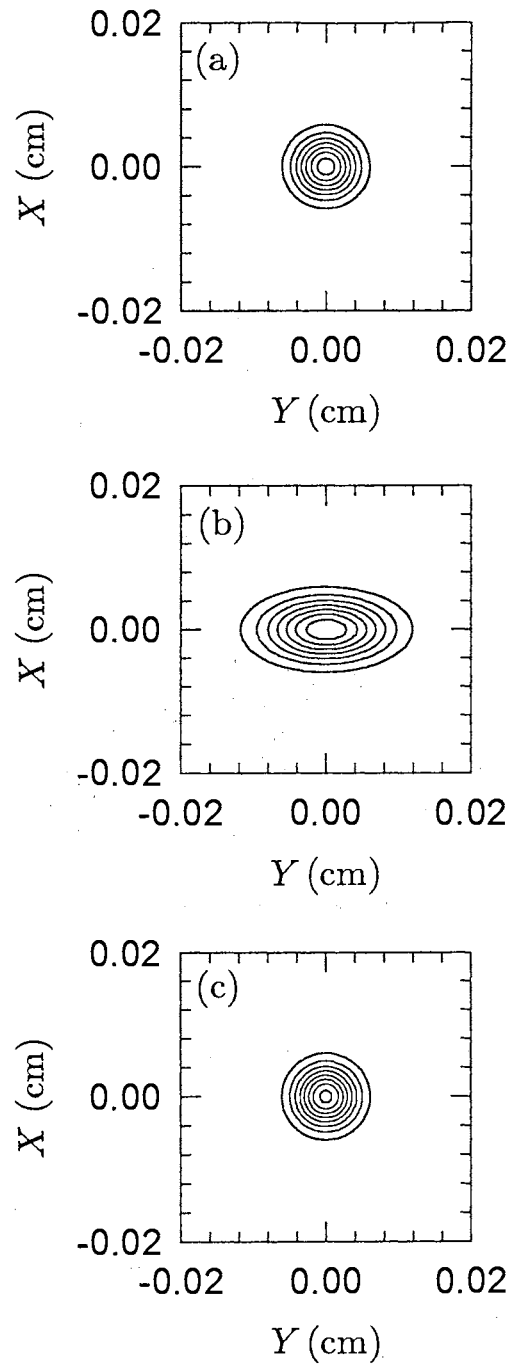


Figure IV.6. Contour plots of the diffracted beam for  $w_w=w_r=0.01$  cm,  $\lambda_w=465.8$  nm,  $n_w=1.57$ ,  $L_G=9$  mm, and  $\theta_w=2^\circ$  (a)  $L_S=1$  mm, ( $L_S \ll L_G$ )  $n_r=1.55$ , and  $\lambda_r=632.8$  nm. (b)  $L_S=10$  mm,  $n_r=1.55$ , and  $\lambda_r=632.8$  nm (c)  $L_S=10$  mm,  $n_r=1.57$ , and  $\lambda_r=465.8$  nm.

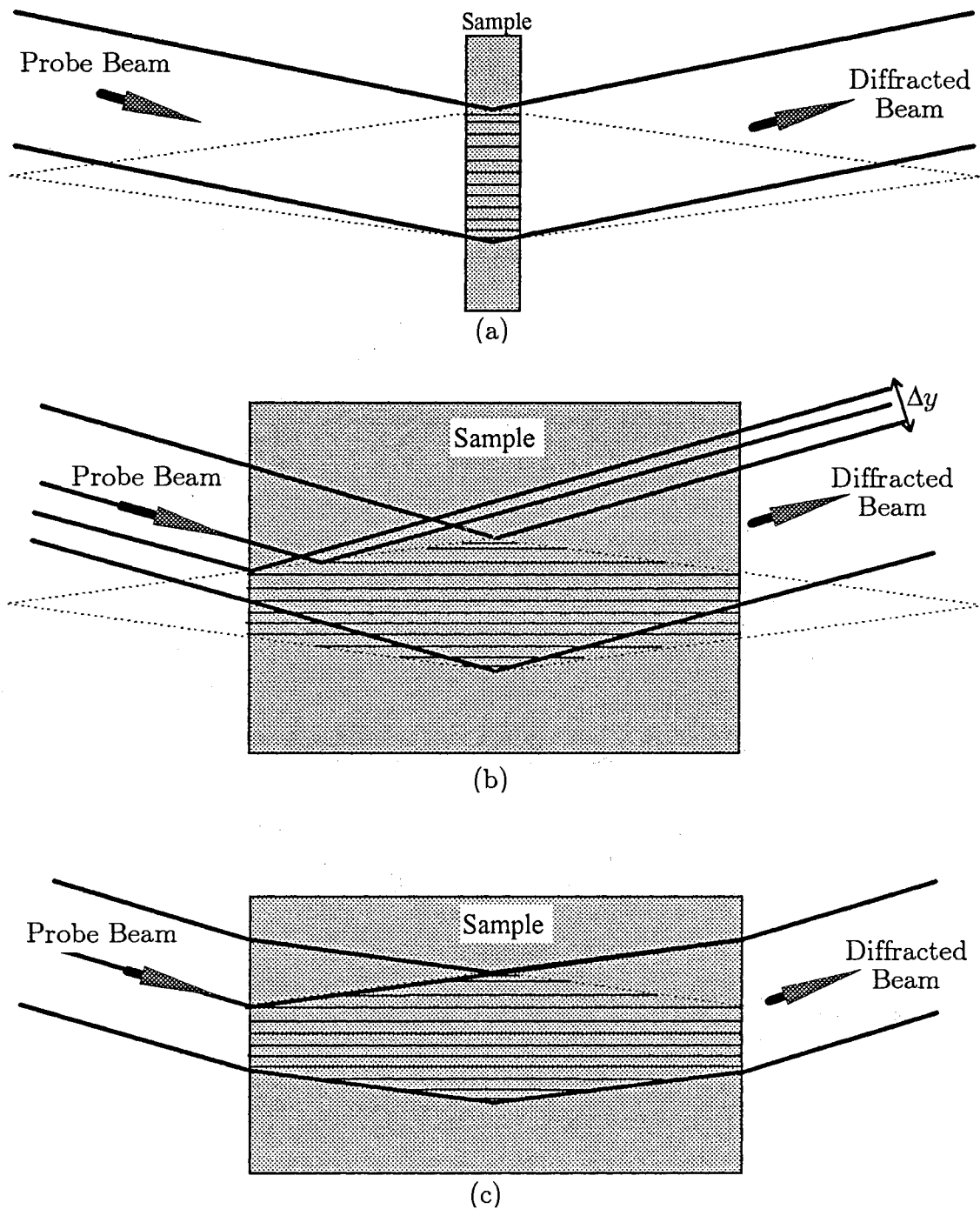


Figure IV.7. (a) The probe beam and the diffracted beam when  $L_S \ll L_G$ . (b) The probe beam and the scattered beam when  $L_S$  is comparable to  $L_G$ . (c) The probe beam and the diffracted beam when  $\lambda_w = \lambda_r$ .

samples and their composition are listed in Table IV.2. Some of the linear parameters for these samples are listed in Table IV.3. The indices of refraction were measured using the Brewster angle technique (see appendix c) and the absorption coefficients were measured using a Cary 05 spectrometer. Throughout the chapter we will refer to these samples by their ID's.

The scattered efficiency was investigated as a function of the write-beam power ( $P_w$ ),  $\theta_w$ , and different write-beam wavelength. The general procedure we used is as follows. The write-beams were kept on until the scattered signal power reached its maximum. Then both write-beams were blocked, over a period of 0.5 min to 2 min, in order to determine the transient component of the scattered signal. This was followed by unblocking one of the write-beams in order to start the erasing process. Most of the time, these steps were repeated twice during the same scan. A typical result is shown in Figure IV.8. In some other scans the write-beams were kept on for a long time after the scattered signal reached its maximum so that the evolution of the grating could be studied. When the writing process started, a scattered signal appeared immediately followed by a gradual increase in the signal intensity until it reached its maximum. The signal build-up usually occurred over a period of one to several minutes depending on the sample, the total power of the write-beams and the crossing angle. The scattered signal was observed to decay slowly if the write-beams were kept on after the signal reached its maximum, see Figure IV.9. The decay rate was different for different samples.

The build-up time ( $t_{bl}$ ) was found to decrease by increasing the write-beams power ( $P_w$ ). Also, by increasing the crossing angle,  $t_{bl}$  seems to decrease except at high  $P_w$  where it was constant. If we partially erase the grating after a

Table IV.2. Identity and Composition of the  $\text{Eu}^{3+}$ -doped Silicate Glasses.  
All Samples contain 2.5 mol%  $\text{Eu}_2\text{O}_3$ .

<i>Sample</i>	Composition (mol%)						
	<i>SiO<sub>2</sub></i>	<i>Al<sub>2</sub>O<sub>3</sub></i>	<i>Na<sub>2</sub>O</i>	MgO	<i>CaO</i>	<i>SrO</i>	<i>BaO</i>
B16	68.25	2.925	14.625	5.85	5.85	-----	-----
B18	68.25	2.925	14.625	5.85	-----	5.85	-----
B20	68.25	2.925	14.625	5.85	-----	-----	5.85
B22	68.25	2.925	14.625	10.53	1.17	-----	-----
B24	68.25	2.925	14.625	10.53	-----	1.17	-----
B26	68.25	2.925	14.625	10.53	-----	-----	1.17
B28	69.71	2.779	13.893	11.12	-----	-----	-----
B29	64.84	2.779	18.761	11.12	-----	-----	-----
B30	61.43	2.630	22.910	10.53	-----	-----	-----

Table IV.3. Some of the linear parameters for the samples used in the study.  
 $L_S$  is the sample thickness,  $n_w$  ( $n_r$ ) is the index of refraction, and  $\alpha_w$  ( $\alpha_r$ ) is the linear absorption coefficient. The subscripts  $w$  and  $r$  refer to the write-beam and read-beam, respectively.  $\lambda_w=465.8$  nm and  $\lambda_r=632.8$  nm.

Sample	$L_S$ (mm)	$n_w$	$n_r$	$\alpha_w$ ( $\text{cm}^{-1}$ )	$\alpha_r$ ( $\text{cm}^{-1}$ )
B16	6.52	1.57	1.55	0.650	0.096
B18	3.84	1.59	1.57	0.855	0.101
B20	3.43	1.58	1.57	1.450	0.370
B22	4.15	1.57	1.55	1.056	0.160
B24	7.24	1.58	1.55	0.914	0.140
B26	5.17	1.57	1.56	1.186	0.180
B28	4.68	1.57	1.56	1.156	0.141
B29	5.47	1.56	1.54	1.301	0.323
B30	4.52	1.54	1.52	1.521	0.461

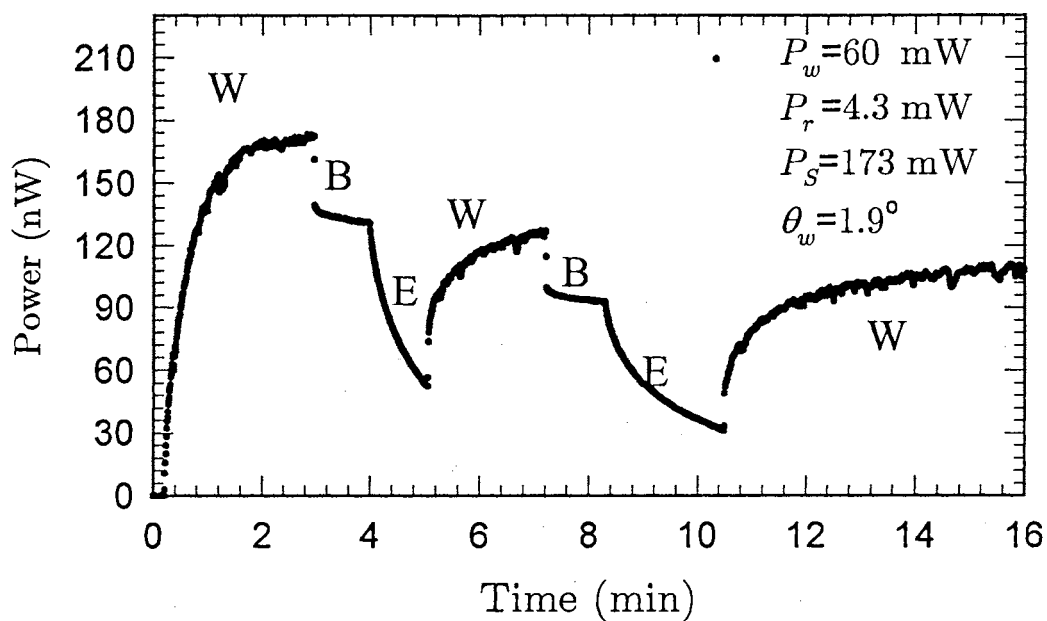


Figure IV. 8. Typical FWM scan using B29. W- writing, B- blocking, and E-erasing.

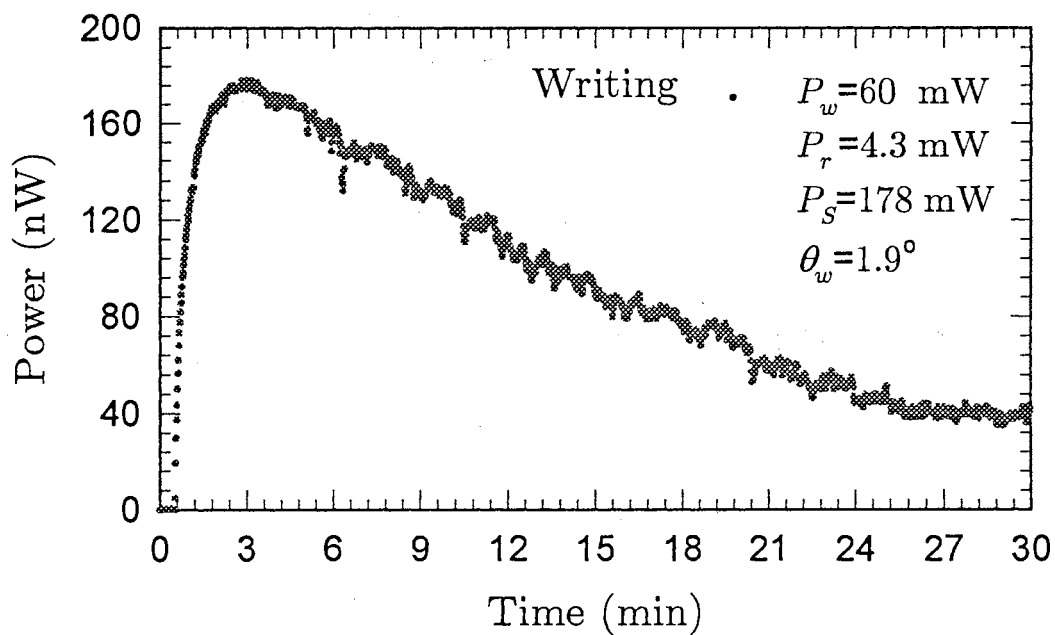


Figure IV.9. The time evolution of the diffracted signal. This result was taken using B29. The signal started to decrease after it reached its maximum when the write-beams were kept on.

maximum value is reached and start writing again, the signal will not go back to its previous maximum value as can be seen from Figure IV.8. However, if the erasing and writing processes took place during the signal build-up (before the signal reached its maximum) we found that the signal continued to grow until it reached its maximum, see Figure IV.10.

The erasing rate was found to be dependent on  $P_w$  and the stage of grating development i.e., the evolution of the grating. When  $P_w$  increased, the erasing rate increased as well. If the erasing process started during the signal building-up, we found that the erasing rate was faster than that when the erasing process started after the signal reached its maximum value, see Figure IV.11. In general, as the signal evolved in time its erasing rate became slower. For example, the rate of erasing the grating after 5 min of writing was faster than erasing it after 10 min. The erasing rate showed no appreciable dependence on the write-beam crossing angle.

When the write-beams were blocked, the signal intensity rapidly decayed to a value between 50% - 90% of the maximum value. Of course, this depends on the sample, the crossing angle and  $P_w$ . This fast reduction in the signal intensity is what we call the transient component of the signal which is in the range 10% - 50% of the maximum value of the scattered power. The transient decay is in the ms time scale and its decay time constant is the same as that of the fluorescence decay rate for the  ${}^5D_0 - {}^7F_0$  transition of the  $\text{Eu}^{3+}$  ion. This rapid decay is the same for all samples checked and is independent of  $P_w$ , see Figure IV.12. In some samples, this fast decay was followed by a slow increase of the scattered signal which leveled off at a final permanent value. However, in some other samples the fast decay was followed by a slow decrease of the signal

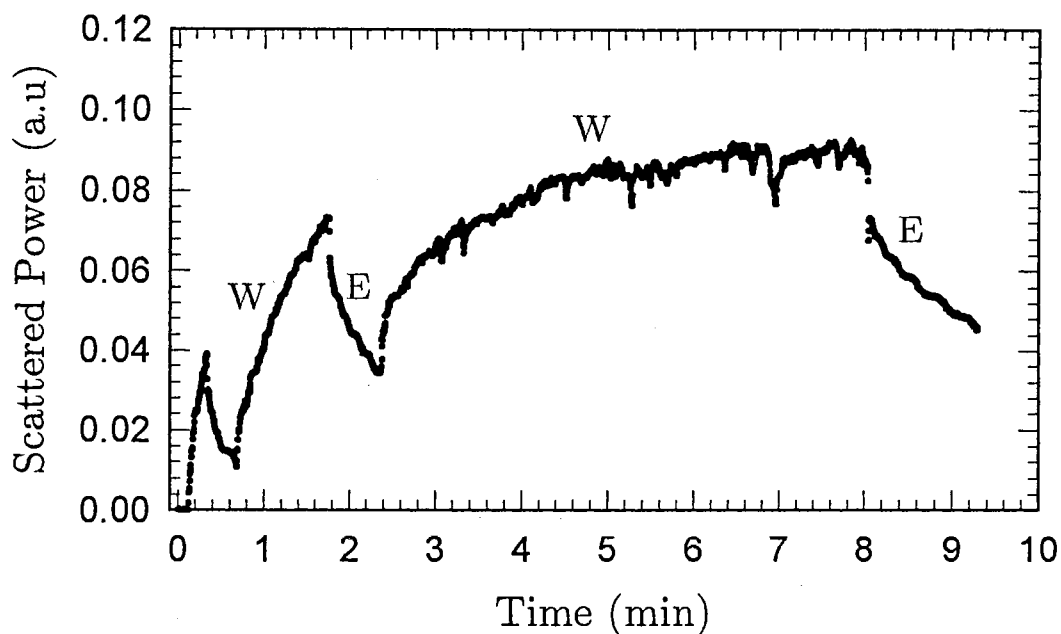


Figure IV.10. Writing-erasing procedure during signal build-up using B24. When writing after erasing, the signal kept growing to a level higher than the previous one until it reached its maximum.  $P_w=44$  mW,  $\theta_w=2.5^\circ$ .

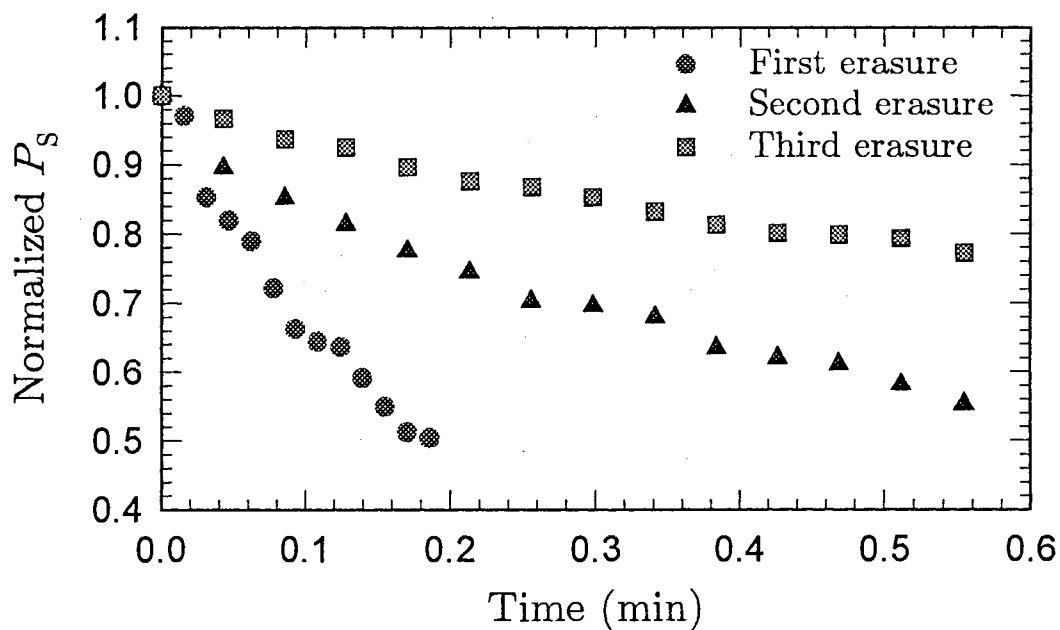


Figure IV.11. The erasing rates during the signal build-up. This data is taken from the previous figure. As the grating became stronger its erasing required more time.



over a period of 14 - 16 min after which the signal leveled off. For all samples, the transient signal was dependent on  $P_w$ ,  $\theta_w$ , and the writing time of the grating. The scattered power of the transient signal increased as  $P_w$  increased and  $\theta_w$  decreased. The dependency of the power of the transient component of the signal ( $P_{tr}$ ) on the grating evolution is different from that of the erasing rate. Figure IV.13 shows that during the signal build-up  $P_{tr}$  increases until it reaches its maximum value when the power of the total signal reaches its maximum.  $P_{tr}$  decreases as we keep the write-beams on after the total signal reached its maximum.

The wavelength of the laser write-beams was changed such that the  $\text{Eu}^{3+}$  ion could be excited with both on- and off-resonance radiation. The wavelengths used were 465.8 nm for on-resonant excitation and 472.7 nm, 488 nm, and 514.5 nm for off-resonant excitation. The signal build-up time was found to increase as the write-beam wavelength increased. The scattered power was maximized for the resonant excitation. Also, the erasing rate was faster when we used the 465.8 nm.

#### (i) The Effect of the Dual-Alkaline Ions

To study the role of the dual-alkaline modifiers in the formation of the LIG, we used 6 samples that have different alkaline ions with different concentrations. The composition of these samples is given in Table IV.2. The group of samples B16, B18, and B20 are members of the same family which we call the 16-family. In this family the concentration of both alkaline ions is the same, 5.85 mol%. Mg will be referred to as the first alkaline while Ca, Sr, and Ba will be referred to as the second alkaline. In these samples, we change the second

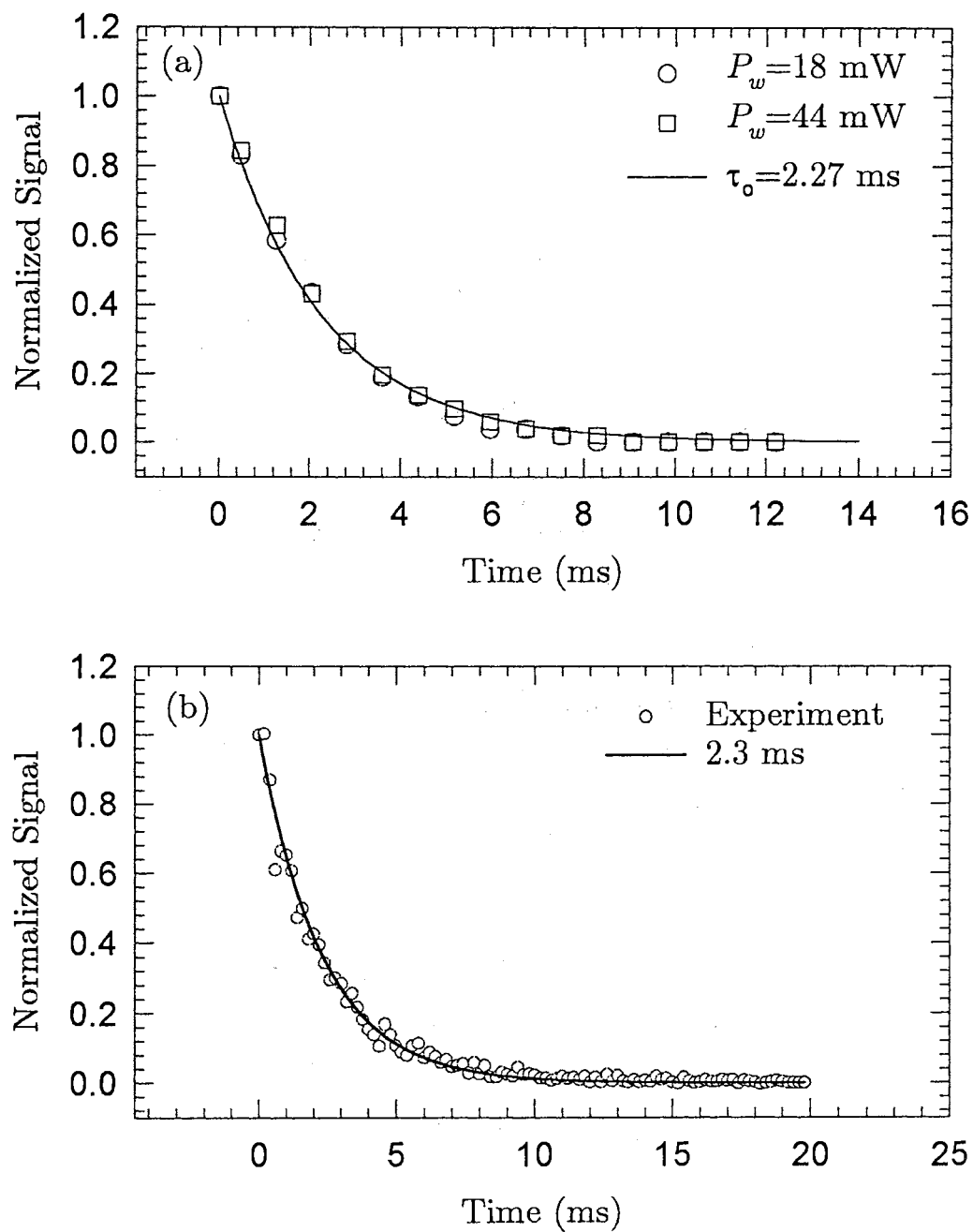


Figure IV.12. (a) Transient signal decay with time constant 2.27 ms. (b) The fluorescence decay with time constant 2.3 ms. This data was taken using B16.

alkaline modifier only.

The group of samples: B22, B24, and B26 will be called the 22-family. In all samples of this family the first alkaline (Mg) has a concentration of 11.14 mol%. The concentration of the second alkaline modifier (Ca, Sr, Ba) is 1.17 mol%. Using both families, we studied the effect of the dual-alkaline ions and their relative concentration on the grating formation. As we will see, the relative concentration of the first and second alkaline ions seems to play an important role in the formation of the grating and the scattering efficiency.

First I will present the experimental results for B18 as a representative sample of the 16-family. Then the experimental results of the B16, B18, and B20 will be presented for comparison purposes. The scattering efficiency of both the maximum and the transient components of the signal for different values of  $P_w$  and  $\theta_w$  is shown in Figure IV.14. Notice that both the transient and

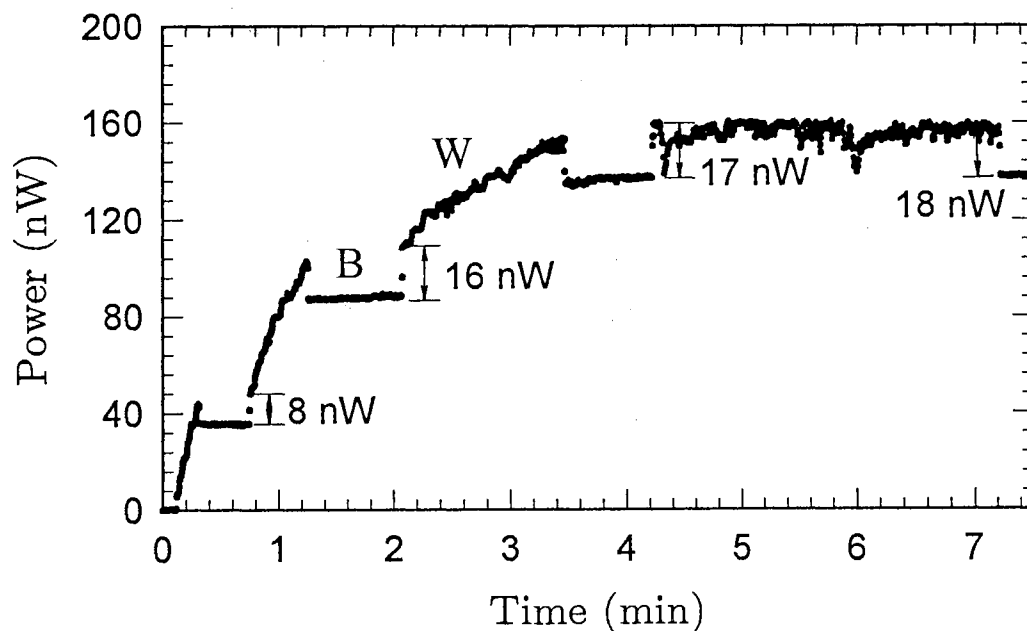


Figure IV.13. This figure shows how the transient component of the signal depends on the evolution of the permanent grating (B24).

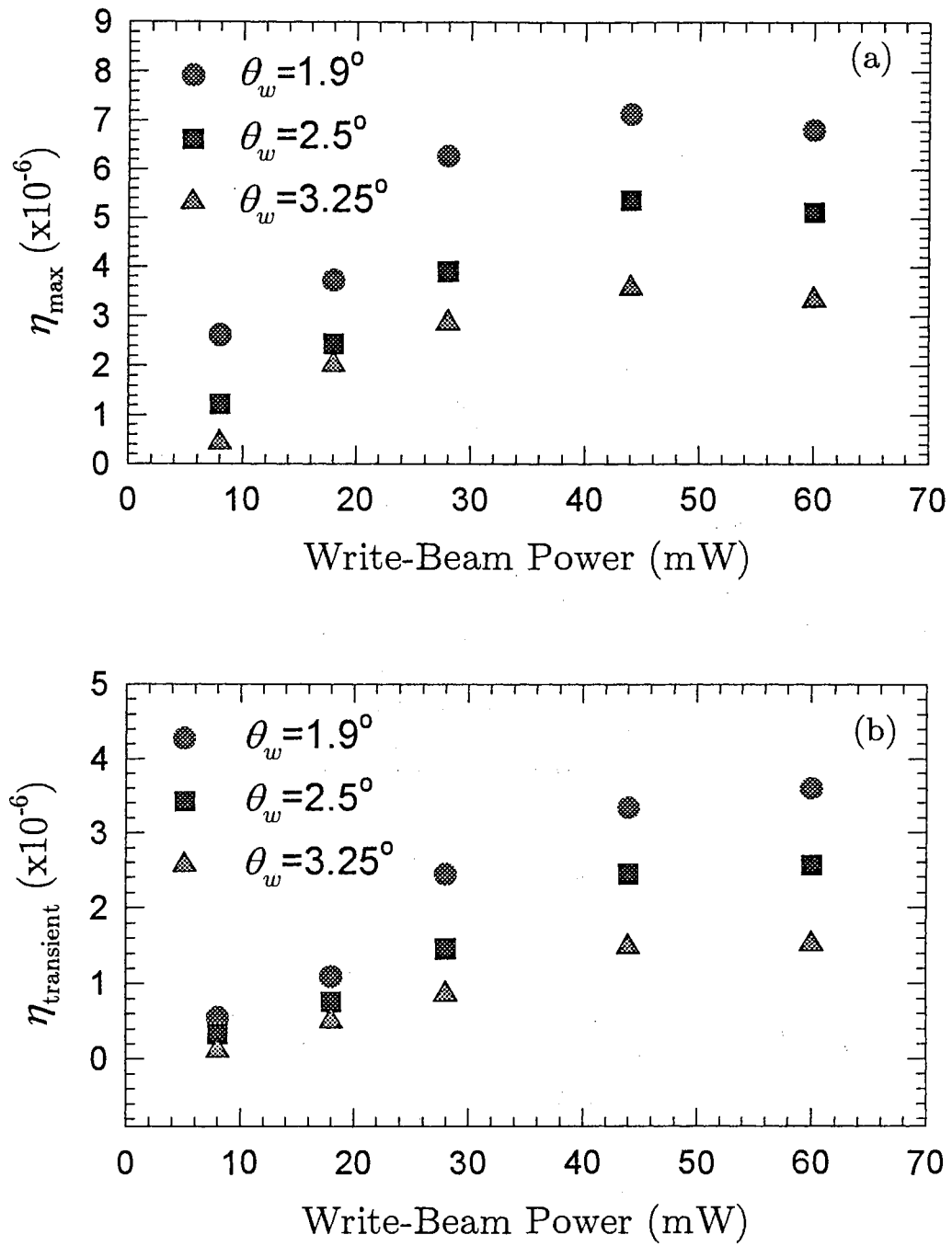


Figure IV.14. The scattered efficiency as a function of  $P_w$  for different values of  $\theta_w$  using B18. (a) The maximum scattered efficiency. (b) The transient efficiency.

the maximum scattered efficiencies start to level off at values of  $P_w$  larger than 28 mW. This behavior is true for all samples studied. The initial increase in the scattered efficiency is not clear as to whether it is linear or quadratic. The three data points we have are not enough to show a clear behavior. Figure IV.14 also shows that the scattered efficiency decreases as the crossing angle increases. This is a typical behavior of the FWM experiment. By increasing  $\theta_w$  the grating length becomes smaller and this in turn reduces the interaction region between the read-beam and the grating. The nonlinear change in the index of refraction  $\Delta n$  due to the structural change in the material can be deduced from the experimental value of the efficiency and the theoretical model discussed in the theory section. From the theoretical model we find  $(\eta/\Delta n^2)$  for each sample, see Table IV.4. The value of  $(\eta/\Delta n^2)$  depends on the sample thickness, the absorption coefficient, and the crossing angle,  $\theta_w$ . Then by knowing the experimental efficiency  $\eta$  we can deduce a value for  $\Delta n$ . Figure IV.15 shows  $\Delta n_{max}$

Table IV.4. Calculated values of  $(\eta/\Delta n^2)$  for  $\lambda_e=465.8$  nm and  $\lambda_p=632.8$  nm.

Sample	$(\eta/\Delta n^2)_{\theta_w=1.9^\circ}$ ( $\times 10^6$ )	$(\eta/\Delta n^2)_{\theta_w=2.5^\circ}$ ( $\times 10^6$ )	$(\eta/\Delta n^2)_{\theta_w=3.25^\circ}$ ( $\times 10^6$ )
B16	2.327	1.394	-----
B18	1.813	1.295	0.856
B20	1.325	0.983	-----
B22	1.798	1.242	-----
B24	1.877	1.098	-----
B26	1.727	1.101	0.667
B29	1.624	1.009	-----
B30	1.519	1.005	0.622

and  $\Delta n_{transient}$  as a function of  $P_w$  for B18. The decay of the scattered signal via the erasing process for different  $P_w$  values is shown in Figure IV.16(a). It is clear that the erasing rate increases as the write-beam power increases. Again this result is a typical behavior of the FWM experiment. However, the results shown in Figure IV.16(b) indicate that the decay rate has no appreciable dependence on the crossing angle,  $\theta_w$ .

The grating build-up time was found to decrease by increasing  $P_w$ , see Figure IV.17. In fact this was the case for all samples that were studied. The results of  $t_{bl}$  as a function of  $\theta_w$  showed that  $t_{bl}$  decreases by decreasing  $\theta_w$  for

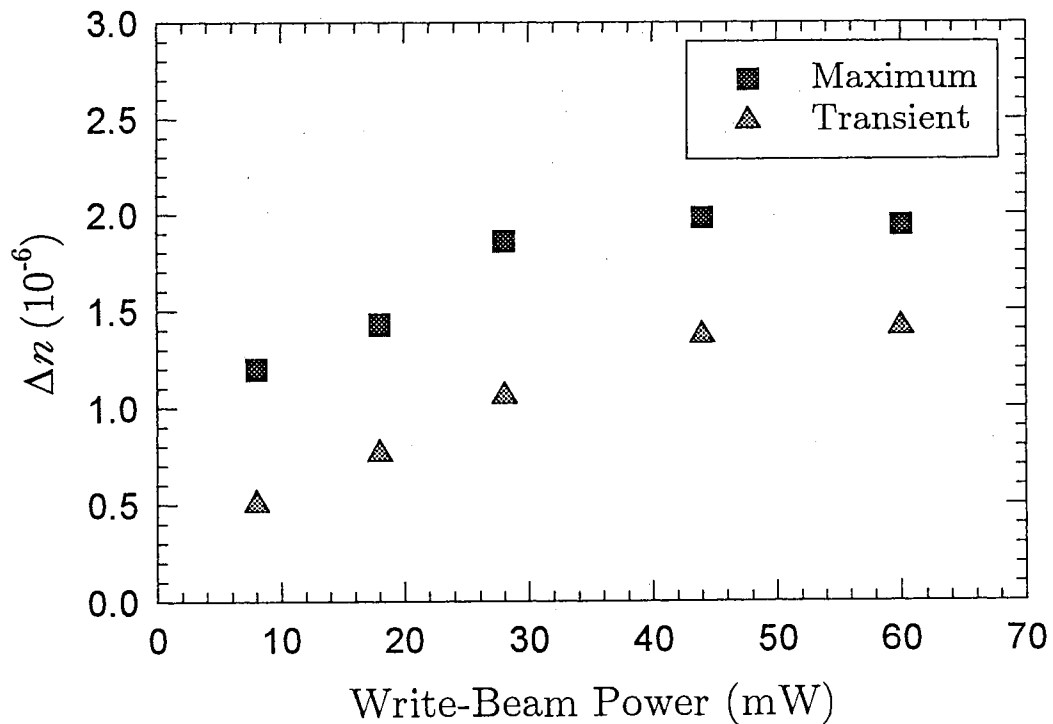


Figure IV.15. The maximum and the transient change in the index of refraction  $\Delta n$  vs  $P_w$  for B18.

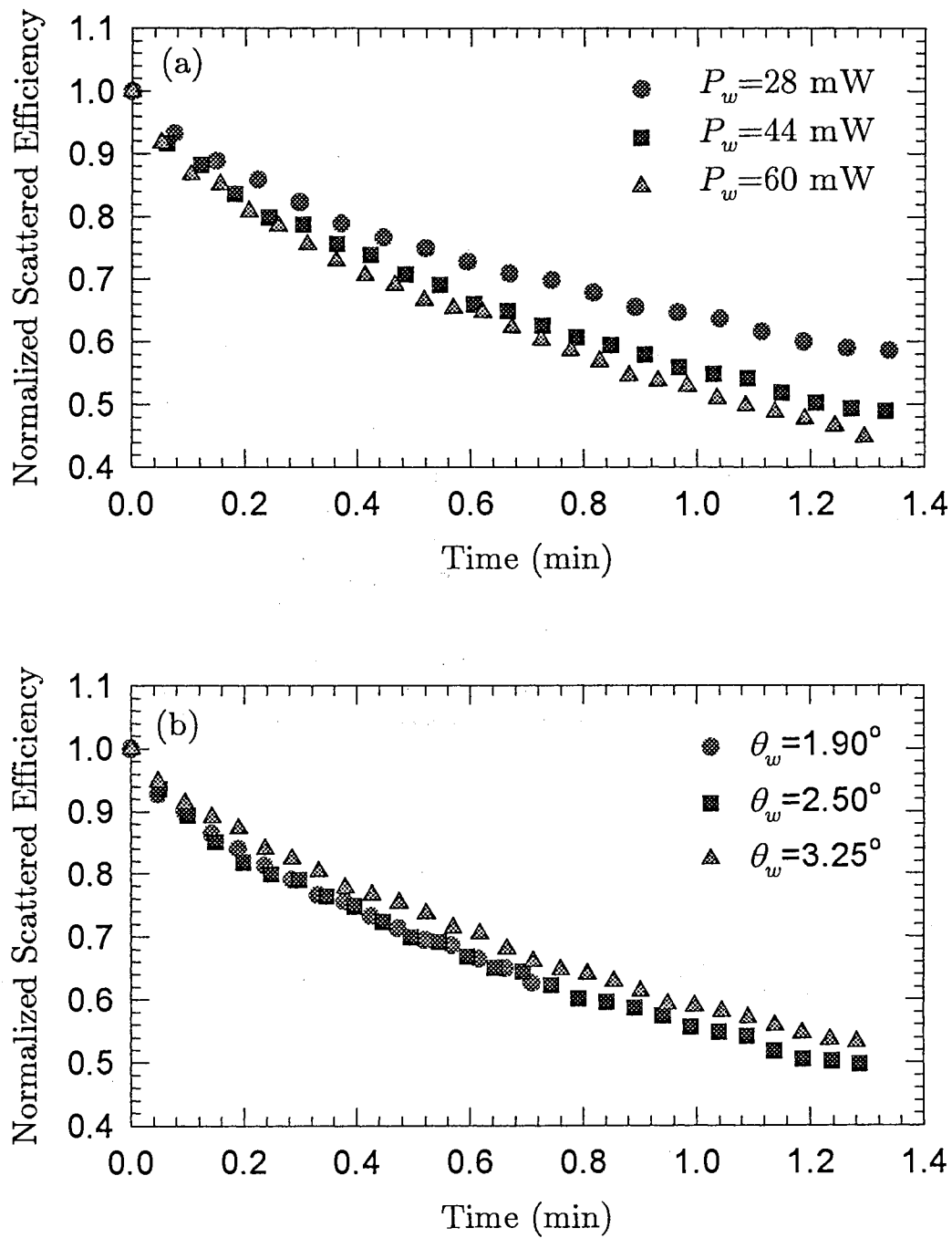


Figure IV.16. Erasing rates using B18 for (a) different  $P_w$  values and  $\theta_w = 2.5^\circ$  (b) different  $\theta_w$  values and  $P_w = 44$  mW.

small values of  $P_w$ . But for large values of  $P_w$ , the dependence of  $t_{bl}$  on  $\theta_w$  was not appreciable. For these samples the ratio of the transient component of the scattered power to the maximum scattered power was very high compared to the rest of the samples studied. This ratio could go as high as 50% of the maximum scattered power for large  $P_w$  values. However, this does not mean that the absolute value of the transient signal is higher than that for the rest of the samples. In fact, the samples of this family have the smallest transient power. Figure IV.18 shows the  $(P_{transient} / P_{max})$  as a function of  $P_w$  for B18.

In order to determine which sample gives the strongest scattered power, we need to compare the results of these samples according to their nonlinear change in the index of refraction,  $\Delta n$ , which is a direct measure of the grating strength. It is important that we make the comparison according to  $\Delta n$  rather than  $\eta$  because these samples have different thicknesses and absorption coefficients which affect both the strength of the grating and the scattered power. As mentioned above, we use the experimental results of  $\eta$  to deduce the nonlinear change in the index of refraction. The results of B16, B18, and B20 are plotted in Figure IV.19. From these results we see that as the mass of the second alkaline increases the value of  $\Delta n$  decreases i.e., the scattering efficiency decreases. This trend was also observed when different values of  $P_w$  and  $\theta_w$  were used. The difference in  $\Delta n$  for the sample which has Sr and that which has Ba is very small. In fact,  $\Delta n$  for B20 is a little larger than that of B18. The explanation of these results will be presented in the discussion section. Unfortunately, it is difficult to compare the erasing rates and the signal build-up times for these sample because they have different thicknesses. This affects the effective power that is responsible for the grating formation and the erasing process. In order to



justify the above statement, we used two samples with the same composition (same composition of B16) but different thicknesses. We found that the signal build-up and the erasing processes are faster for the thin sample despite the fact that both samples were exposed to the same write-beam power, see Figure IV.20. This clearly shows that samples with different constituents must have the same thickness in order to compare their signal build-up times and their erasing rates. The erasing rates for B18 and B20 were found to be the same. We should mention here that these two samples have comparable thicknesses, see Table IV.3. The experimental data for B16, B18, and B20 are listed in Tables IV.5 and IV.6.

B26 was used as a representative sample for the 22-family. The scattered powers of the samples in the 22-family are considerably higher than those of the 16-family. Figure IV.21 shows the scattered efficiency and the nonlinear change in the index of refraction as a function of  $P_w$ . Notice that these results have the same behavior reported for the B18 except that the scattered efficiency is larger in this case. To compare the samples of the 22-family we show the results of  $\Delta n$  in Figure IV.22. In this case the scattered efficiency increased by increasing the mass of the second alkaline modifier. The explanation of this result and its connection to the relative concentration of the two alkaline modifiers will be discussed in the discussion section. The signal build-up time results show no appreciable dependence on the mass of the second alkaline. This kind of observation might not be completely true because these samples have different thicknesses. By comparing the erasing rates of B22 and B26, we find that B26 has a faster decay rate than B22. This means that if the signal build-up is fast the erasure of the grating will be fast as well. Figure IV.23 shows the ratio of

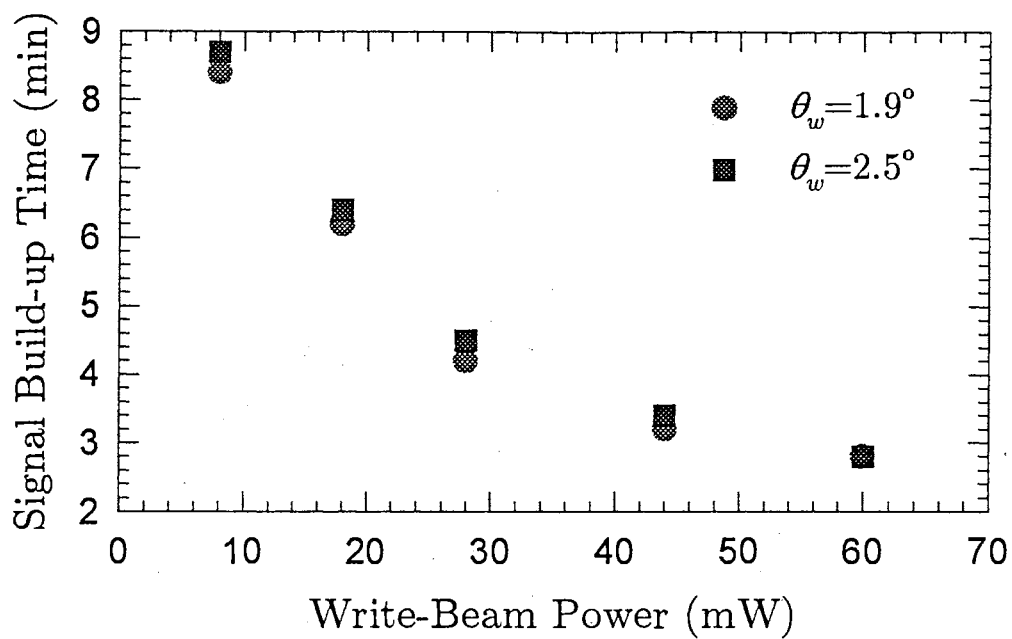


Figure IV.17. Signal build-up time as a function of  $P_w$  for different  $\theta_w$  values using B18.

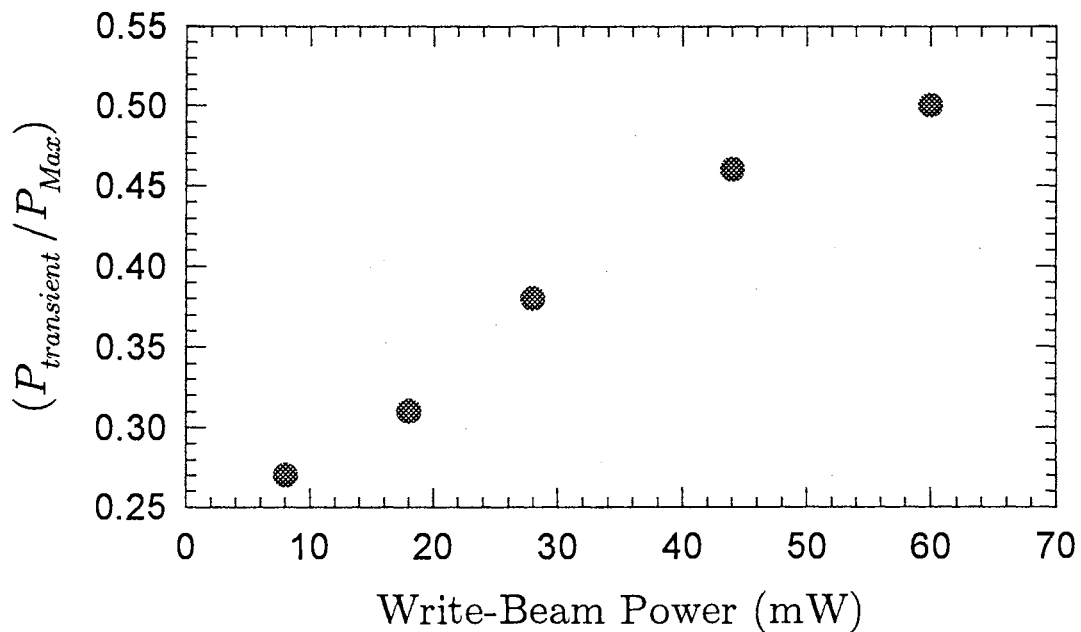


Figure IV.18. The ratio of the transient power to the maximum diffracted power vs  $P_w$  at  $\theta_w = 2.5^\circ$  using B18.

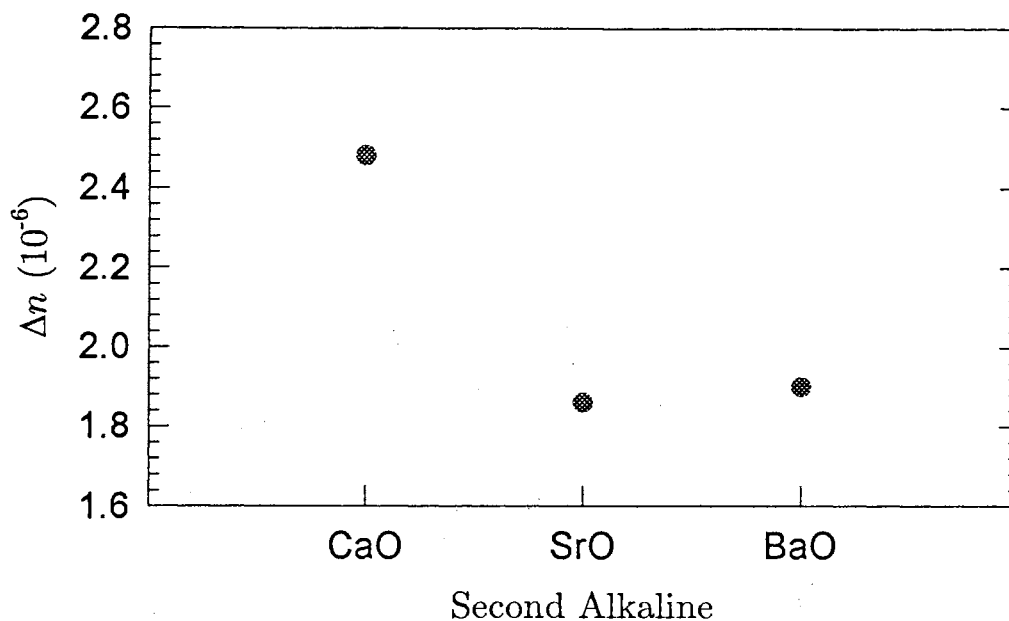


Figure IV.19. The change in the index of refraction  $\Delta n$  for the samples of the 16-family. This figure shows how the grating is affected by the mass of the second alkaline ion.

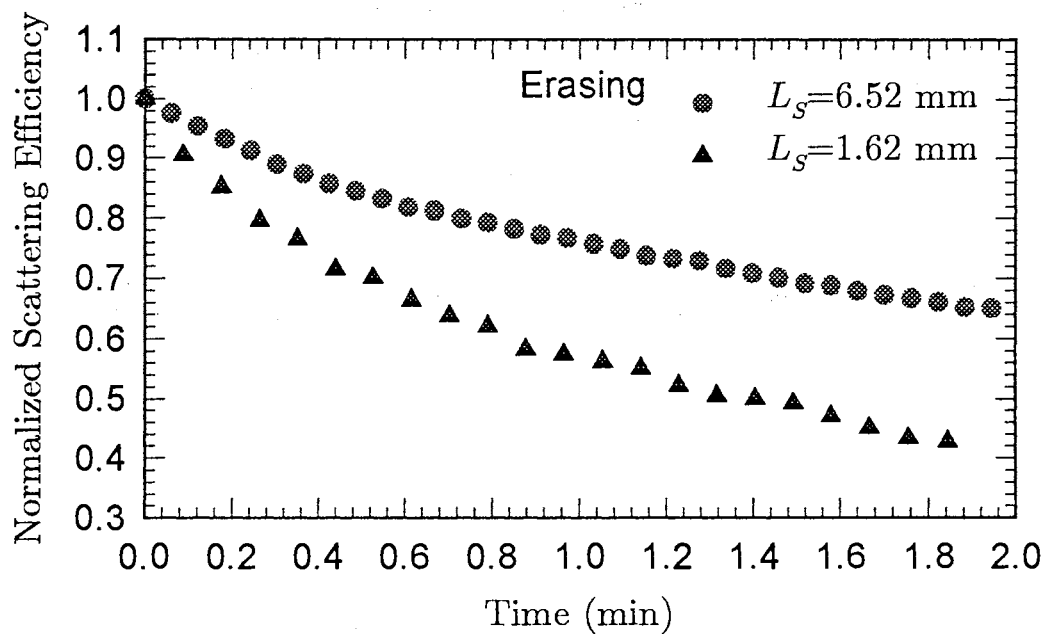


Figure IV.20. Erasing rates of the permanent grating for B16CS and B16SQ. This shows how the thickness of the sample affects the erasing rate.

Table IV.5. The maximum scattering efficiency and  $\Delta n$  for the 16-family.

B18						
$P_w$	$\eta_{\theta_w=1.9^\circ}$	$\Delta n_{\theta_w=1.9^\circ}$	$\eta_{\theta_w=2.5^\circ}$	$\Delta n_{\theta_w=2.5^\circ}$	$\eta_{\theta_w=3.25^\circ}$	$\Delta n_{\theta_w=3.25^\circ}$
(mW)	( $10^{-6}$ )	( $10^{-6}$ )	( $10^{-6}$ )	( $10^{-6}$ )	( $10^{-6}$ )	( $10^{-6}$ )
8	2.62	1.20	1.22	0.97	0.43	0.71
18	3.72	1.43	2.44	1.37	2.02	1.54
28	6.28	1.86	3.90	1.74	2.86	1.83
44	7.14	1.98	5.37	2.04	3.57	2.04
60	6.82	1.94	5.12	1.99	3.33	1.97
B16						
$P_w$	$\eta_{\theta_w=1.9^\circ}$	$\Delta n_{\theta_w=1.9^\circ}$	$\eta_{\theta_w=2.5^\circ}$	$\Delta n_{\theta_w=2.5^\circ}$	$\eta_{\theta_w=3.25^\circ}$	$\Delta n_{\theta_w=3.25^\circ}$
(mW)	( $10^{-6}$ )	( $10^{-6}$ )	( $10^{-6}$ )	( $10^{-6}$ )	( $10^{-6}$ )	( $10^{-6}$ )
8	3.90	1.30	----	----	----	----
28	14.3	2.48	8.37	2.45	----	----
44	14.3	2.48	----	----	----	----
B20						
$P_w$	$\eta_{\theta_w=1.9^\circ}$	$\Delta n_{\theta_w=1.9^\circ}$	$\eta_{\theta_w=2.5^\circ}$	$\Delta n_{\theta_w=2.5^\circ}$	$\eta_{\theta_w=3.25^\circ}$	$\Delta n_{\theta_w=3.25^\circ}$
(mW)	( $10^{-6}$ )	( $10^{-6}$ )	( $10^{-6}$ )	( $10^{-6}$ )	( $10^{-6}$ )	( $10^{-6}$ )
28	4.77	1.90	3.49	1.88	----	----

Table IV.6. The transient scattering efficiency and  $\Delta n$  for the 16-family.

B18						
$P_w$	$\eta_{\theta_w=1.9^\circ}$	$\Delta n_{\theta_w=1.9^\circ}$	$\eta_{\theta_w=2.5^\circ}$	$\Delta n_{\theta_w=2.5^\circ}$	$\eta_{\theta_w=3.25^\circ}$	$\Delta n_{\theta_w=3.25^\circ}$
(mW)	( $10^{-6}$ )	( $10^{-6}$ )	( $10^{-6}$ )	( $10^{-6}$ )	( $10^{-6}$ )	( $10^{-6}$ )
8	0.55	0.55	0.33	0.51	0.11	0.37
18	1.09	0.78	0.76	0.76	0.50	0.76
28	2.44	1.16	1.46	1.06	0.86	1.00
44	3.33	1.36	2.44	1.37	1.48	1.32
60	3.60	1.40	2.56	1.41	1.52	1.33
B16						
$P_w$	$\eta_{\theta_w=1.9^\circ}$	$\Delta n_{\theta_w=1.9^\circ}$	$\eta_{\theta_w=2.5^\circ}$	$\Delta n_{\theta_w=2.5^\circ}$	$\eta_{\theta_w=3.25^\circ}$	$\Delta n_{\theta_w=3.25^\circ}$
(mW)	( $10^{-6}$ )	( $10^{-6}$ )	( $10^{-6}$ )	( $10^{-6}$ )	( $10^{-6}$ )	( $10^{-6}$ )
8	0.33	0.37	----	----	----	----
28	1.98	0.92	1.86	1.16	----	----
44	3.57	1.24	----	----	----	----
B20						
$P_w$	$\eta_{\theta_w=1.9^\circ}$	$\Delta n_{\theta_w=1.9^\circ}$	$\eta_{\theta_w=2.5^\circ}$	$\Delta n_{\theta_w=2.5^\circ}$	$\eta_{\theta_w=3.25^\circ}$	$\Delta n_{\theta_w=3.25^\circ}$
(mW)	( $10^{-6}$ )	( $10^{-6}$ )	( $10^{-6}$ )	( $10^{-6}$ )	( $10^{-6}$ )	( $10^{-6}$ )
44	1.40	1.03	1.07	1.04	----	----

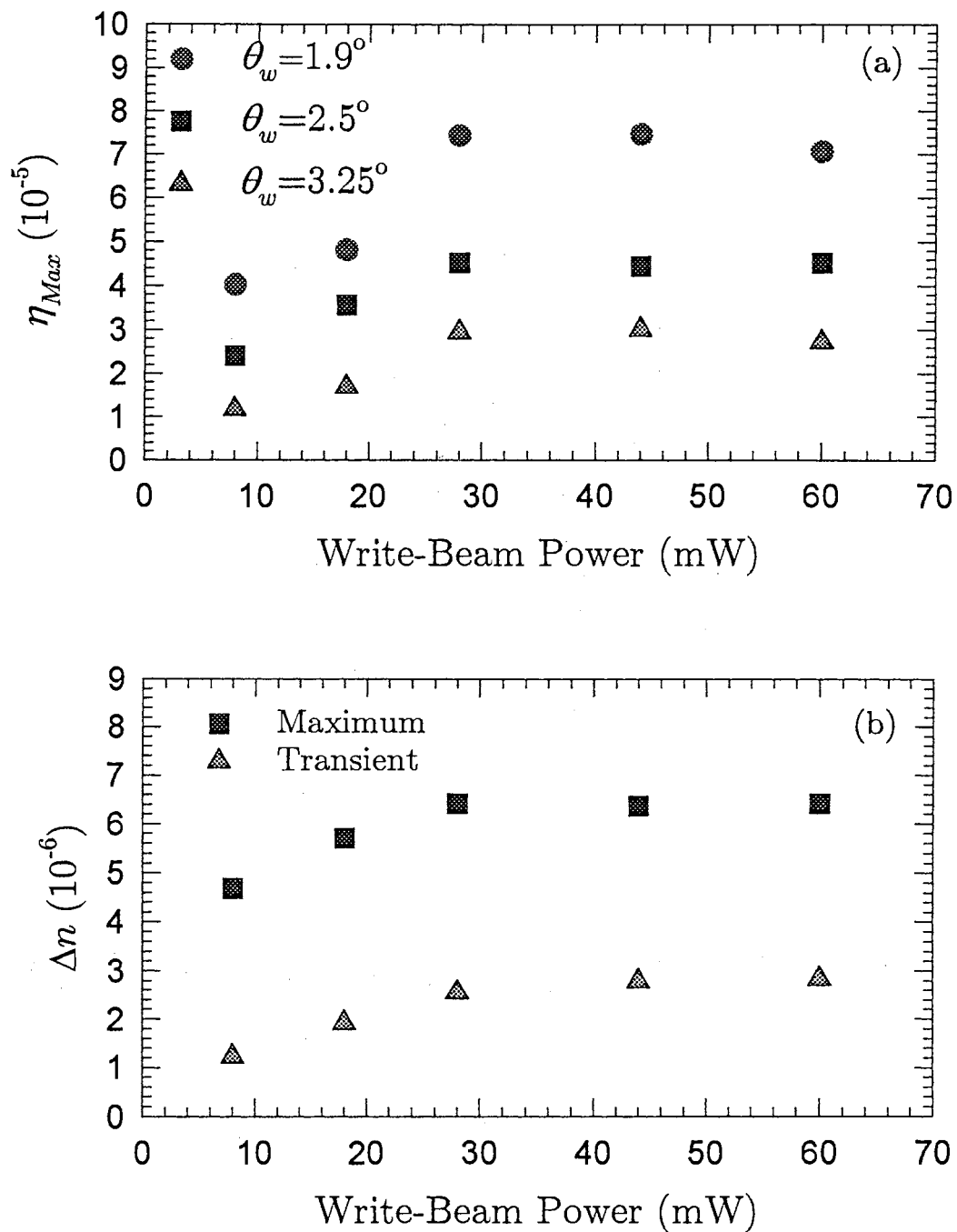


Figure IV.21. (a) The diffracted efficiency as a function of  $P_w$  for different  $\theta_w$  values using B26. (b) The corresponding change in the index of refraction vs  $P_w$ .

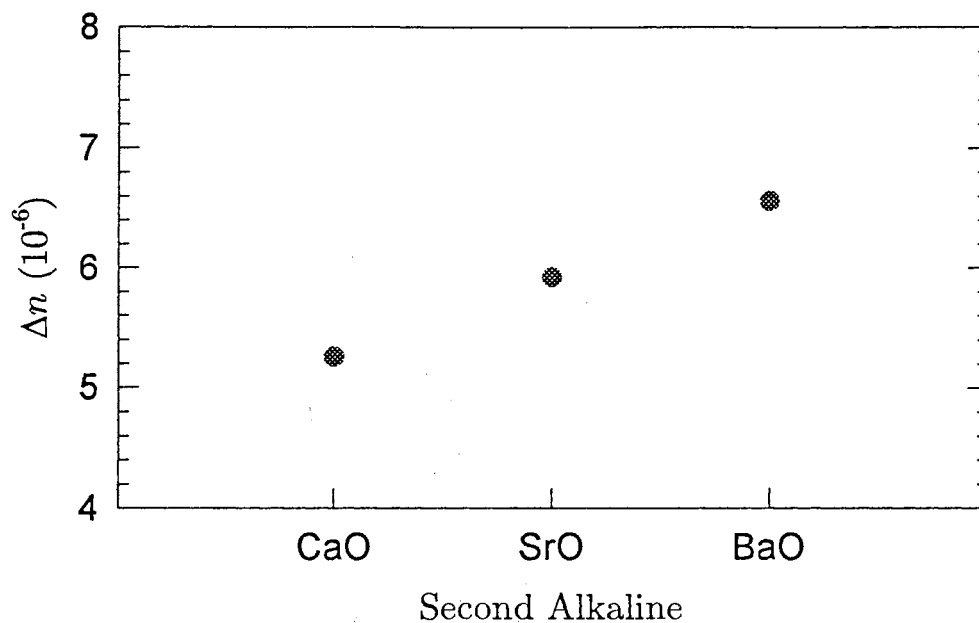


Figure IV.22. The change in the index of refraction for the samples of the 22-family.

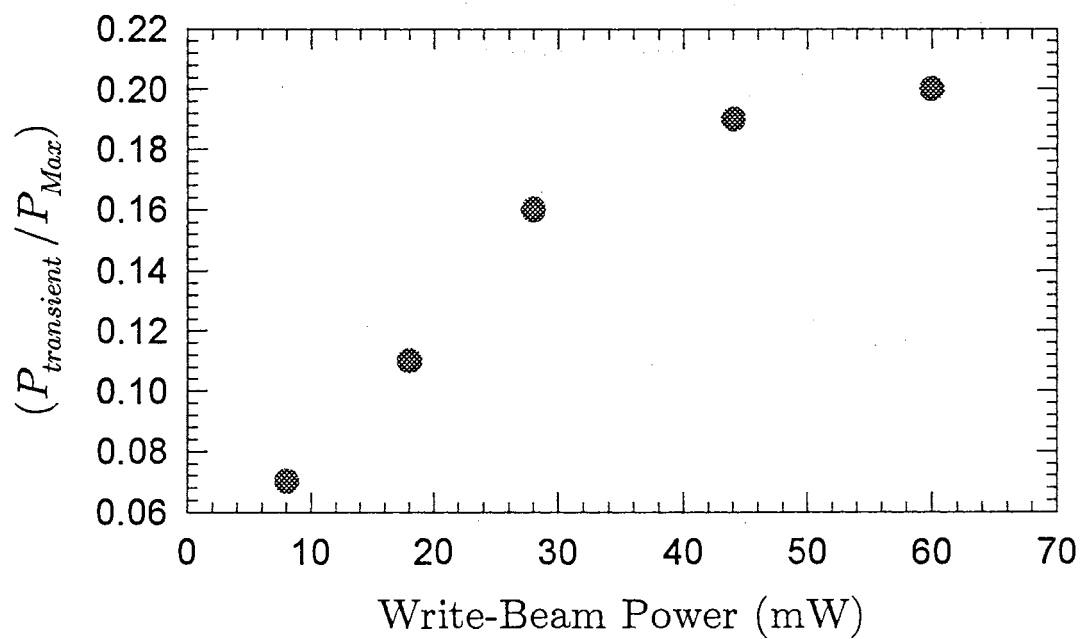


Figure IV.23. The ratio of the transient power to the maximum diffracted power vs  $P_w$  at  $\theta_w=2.5^\circ$  using B26.

$(P_{transient} / P_{max})$  as a function of  $P_w$  for B26. By comparing the results of Figures IV.18 and IV.23 we see that the transient component of the scattered power of B26 is smaller than that of B18. Although the absolute value of the transient power of B26 is higher than that of B18. The experimental results for the samples of the 22-family are listed in Tables IV.7 and IV.8.

In order to clearly see the dependency of  $\Delta n$  on the concentration and type of the second alkaline modifier, we plot the data of both families in Figure IV.24. From this Figure we see that for the 16-family the efficiency decreased as the mass of the second alkaline ion increased. However, the 22-family results show that the scattering efficiency increased when the mass of the second alkaline modifier was increased. Notice also that all samples of the 22-family yielded higher efficiencies than those of the 16-family. The interpretation of these results will be presented in the discussion section.

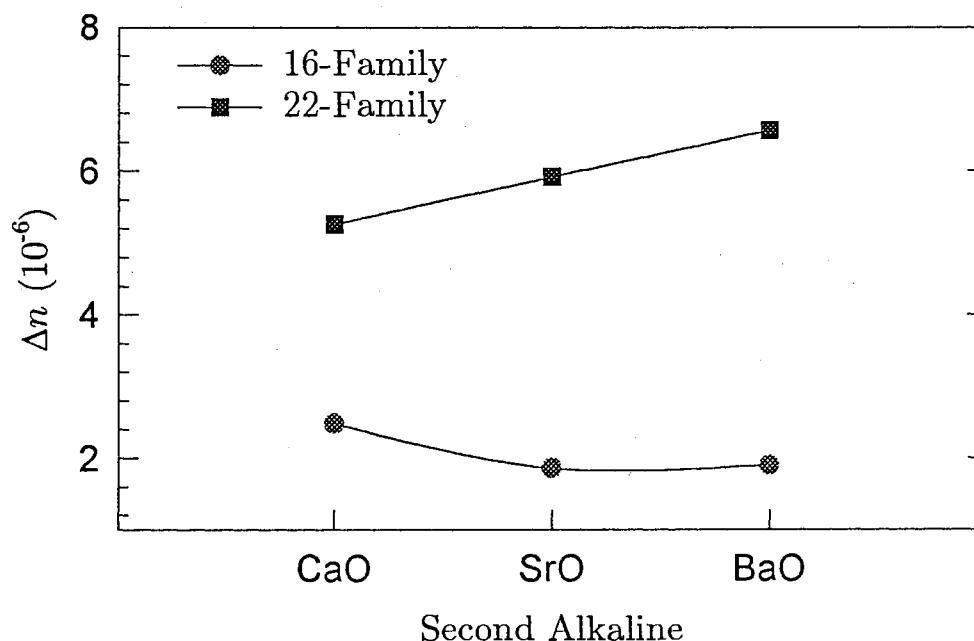


Figure IV.24. The change in the index of refraction  $\Delta n$  for the 16-family and the 22-family. Notice the difference in the behavior as the mass of the second alkaline ion increased.



Table IV.7. The maximum scattering efficiency and  $\Delta n$  for the 22-family.

B26						
$P_w$	$\eta_{\theta_w=1.9^\circ}$	$\Delta n_{\theta_w=1.9^\circ}$	$\eta_{\theta_w=2.5^\circ}$	$\Delta n_{\theta_w=2.5^\circ}$	$\eta_{\theta_w=3.25^\circ}$	$\Delta n_{\theta_w=3.25^\circ}$
(mW)	( $10^{-6}$ )	( $10^{-6}$ )	( $10^{-6}$ )	( $10^{-6}$ )	( $10^{-6}$ )	( $10^{-6}$ )
8	40.2	4.83	24.1	4.68	11.7	4.18
18	48.1	5.28	35.7	5.70	16.9	5.03
28	74.4	6.56	45.2	6.41	29.5	6.65
44	74.7	6.58	44.5	6.36	30.2	6.73
60	70.7	6.40	45.2	6.41	27.3	6.40
B22						
$P_w$	$\eta_{\theta_w=1.9^\circ}$	$\Delta n_{\theta_w=1.9^\circ}$	$\eta_{\theta_w=2.5^\circ}$	$\Delta n_{\theta_w=2.5^\circ}$	$\eta_{\theta_w=3.25^\circ}$	$\Delta n_{\theta_w=3.25^\circ}$
(mW)	( $10^{-6}$ )	( $10^{-6}$ )	( $10^{-6}$ )	( $10^{-6}$ )	( $10^{-6}$ )	( $10^{-6}$ )
8	34.0	4.35	----	----	----	----
28	49.8	5.26	35.0	5.31	----	----
44	43.5	4.92	----	----	----	----
B24						
$P_w$	$\eta_{\theta_w=1.9^\circ}$	$\Delta n_{\theta_w=1.9^\circ}$	$\eta_{\theta_w=2.5^\circ}$	$\Delta n_{\theta_w=2.5^\circ}$	$\eta_{\theta_w=3.25^\circ}$	$\Delta n_{\theta_w=3.25^\circ}$
(mW)	( $10^{-6}$ )	( $10^{-6}$ )	( $10^{-6}$ )	( $10^{-6}$ )	( $10^{-6}$ )	( $10^{-6}$ )
8	41.9	4.72	----	----	----	----
28	65.8	5.92	37.9	5.88	----	----
44	69.5	6.09	----	----	----	----

Table IV.8. The transient scattering efficiency and  $\Delta n$  for the 22-family.

B26						
$P_w$	$\eta_{\theta_w=1.9^\circ}$	$\Delta n_{\theta_w=1.9^\circ}$	$\eta_{\theta_w=2.5^\circ}$	$\Delta n_{\theta_w=2.5^\circ}$	$\eta_{\theta_w=3.25^\circ}$	$\Delta n_{\theta_w=3.25^\circ}$
(mW)	( $10^{-6}$ )	( $10^{-6}$ )	( $10^{-6}$ )	( $10^{-6}$ )	( $10^{-6}$ )	( $10^{-6}$ )
8	4.55	1.62	1.67	1.23	1.19	1.34
18	6.89	2.00	4.05	1.92	1.90	1.69
28	12.0	2.64	7.14	2.55	3.86	2.41
44	14.4	2.89	8.57	2.79	6.14	3.03
60	14.9	2.94	8.81	2.83	5.46	2.86
B22						
$P_w$	$\eta_{\theta_w=1.9^\circ}$	$\Delta n_{\theta_w=1.9^\circ}$	$\eta_{\theta_w=2.5^\circ}$	$\Delta n_{\theta_w=2.5^\circ}$	$\eta_{\theta_w=3.25^\circ}$	$\Delta n_{\theta_w=3.25^\circ}$
(mW)	( $10^{-6}$ )	( $10^{-6}$ )	( $10^{-6}$ )	( $10^{-6}$ )	( $10^{-6}$ )	( $10^{-6}$ )
8	3.72	1.44	----	----	----	----
28	7.73	2.07	4.55	1.91	----	----
44	9.30	2.27	----	----	----	----
B24						
$P_w$	$\eta_{\theta_w=1.9^\circ}$	$\Delta n_{\theta_w=1.9^\circ}$	$\eta_{\theta_w=2.5^\circ}$	$\Delta n_{\theta_w=2.5^\circ}$	$\eta_{\theta_w=3.25^\circ}$	$\Delta n_{\theta_w=3.25^\circ}$
(mW)	( $10^{-6}$ )	( $10^{-6}$ )	( $10^{-6}$ )	( $10^{-6}$ )	( $10^{-6}$ )	( $10^{-6}$ )
8	2.38	1.13	----	----	----	----
28	6.05	1.80	3.64	1.82	----	----
44	1.34	2.67	----	----	----	----

(ii) Sodium Enriched  $\text{Eu}^{3+}$  -Doped Silicate Glasses

The  $\text{Na}_2\text{O}$  enriched samples are B29 and B30. In these samples the concentration of  $\text{Na}_2\text{O}$  was increased mainly at the expense of the  $\text{SiO}_2$  concentration. The measurements done on these samples were like those performed on the rest of the samples. The scattered efficiency as a function of  $P_w$  and  $\theta_w$  has the same behavior observed with the rest of the samples. We found that by increasing the  $\text{Na}_2\text{O}$  concentration the scattered efficiency and the erasing rate were decreased and the signal build-up time was increased. Figure IV.25 shows the experimental results of the scattered efficiency for both samples. Again the scattered signal starts to saturate for  $P_w$  values larger than 28 mW. For these two samples the permanent signal was observed to decay slowly when both write-beams were blocked. This slow decay was taking place over a period of 14 - 16 min after which the signal levels off. The sample with the larger amount of  $\text{Na}_2\text{O}$  was found to have the larger decay rate. The decay of the permanent grating while both write-beams were blocked is shown in Figure IV.26(a). To erase the permanent grating, only one of the write-beams was incident on the sample. The erasing rates show that B29 can be erased faster than B30, see Figure IV.26(b). In Table IV.9 we list the experimental results for both samples.

(iii) The Dependence of the Grating Formation on the Write-Beam Wavelength

To study the role of the write-beam wavelength ( $\lambda_w$ ) on the LIG, we used B 28 because it has the best scattering efficiency among all the samples studied. The experimental configuration is the same as that shown in Figure IV.1.

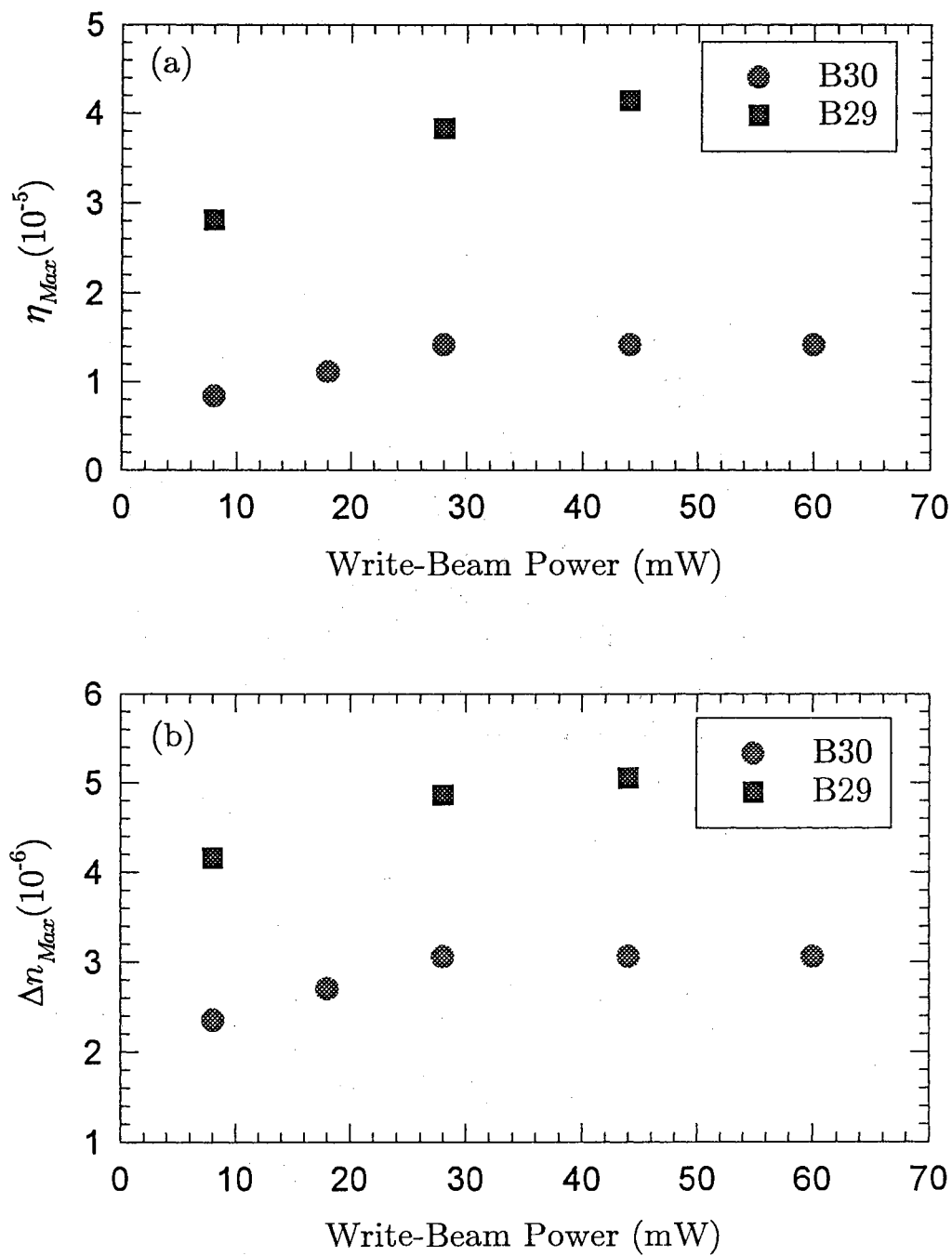


Figure IV.25. (a) The diffracted efficiency as a function of  $P_w$  for B29 and B30 at  $\theta_w=1.9^\circ$ . (b) The corresponding change in the index of refraction vs  $P_w$ .

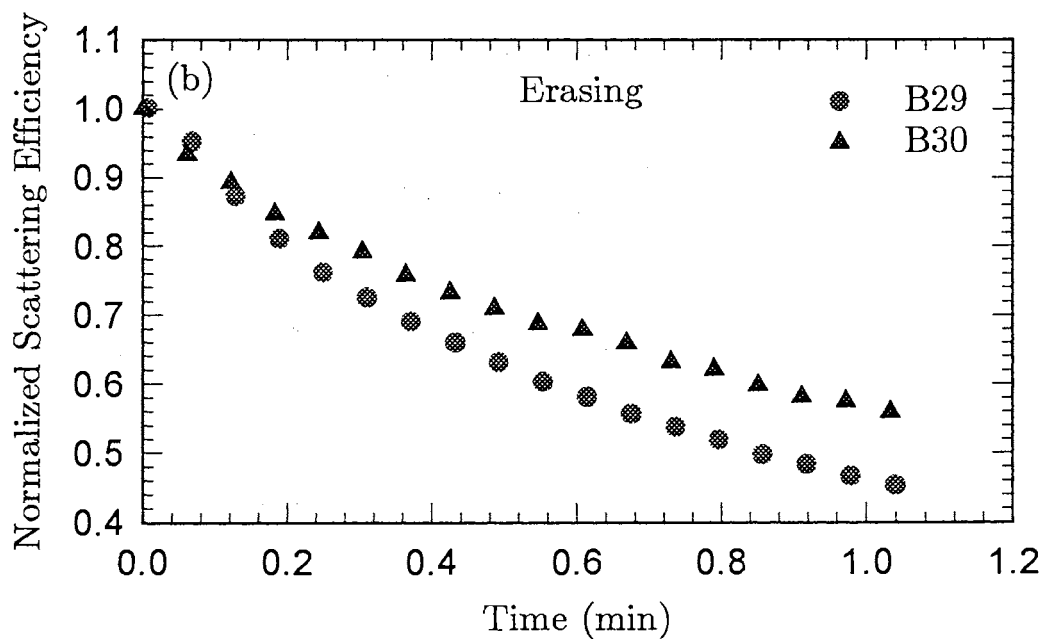
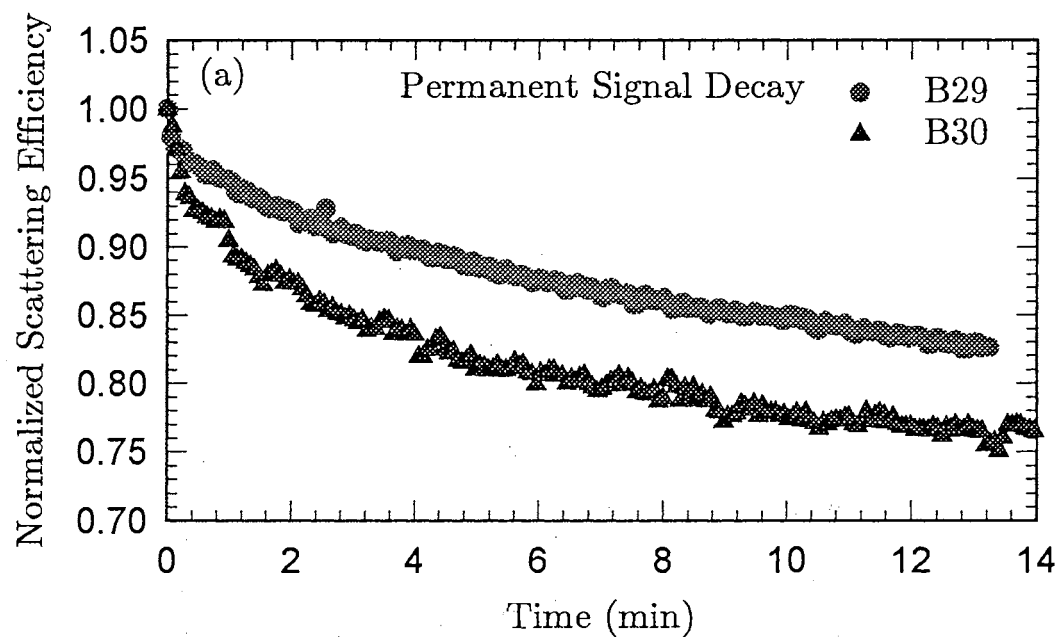


Figure IV.26. (a) The decay of the permanent grating of B29 and B30 while both write-beams were blocked. (b) The decay of the permanent signal using the erasing procedure.

Table IV.9. The maximum scattering efficiency and  $\Delta n$  for B29 and B30.

B30				
$P_w$	$\eta_{\theta_w=1.9^\circ}$	$\Delta n_{\theta_w=1.9^\circ}$	$\eta_{\theta_w=3.25^\circ}$	$\Delta n_{\theta_w=3.25^\circ}$
(mW)	( $10^{-6}$ )	( $10^{-6}$ )	( $10^{-6}$ )	( $10^{-6}$ )
8	8.37	2.35	3.57	2.40
18	11.1	2.70	4.52	2.70
28	14.2	3.06	6.51	3.24
44	14.2	3.06	6.28	3.18
60	14.2	3.06	6.67	3.28
B29				
$P_w$	$\eta_{\theta_w=1.9^\circ}$	$\Delta n_{\theta_w=1.9^\circ}$	$\eta_{\theta_w=2.50^\circ}$	$\Delta n_{\theta_w=2.50^\circ}$
(mW)	( $10^{-6}$ )	( $10^{-6}$ )	( $10^{-6}$ )	( $10^{-6}$ )
8	28.1	4.16	----	----
28	38.3	4.86	23.9	4.87
44	41.4	5.05	----	----

Throughout these measurements we kept  $P_w=44$  mW and  $\theta_w=2.5^\circ$  (measured in air). The wavelengths used were 465.8 nm for on-resonant excitation and 472.7 nm, 488 nm, and 514.5 nm for off-resonant excitation. In all cases, the laser beam has a Gaussian spatial profile. As in the previous experiments the spot sizes of both the write-beam and the read-beam were 100  $\mu\text{m}$ . In order to study the effect of the different wavelengths, we measured the signal build-up time, the maximum scattered efficiency, and the erasing rate of the grating. The signal build-up time ( $t_{bl}$ ) was found to increase with increasing  $\lambda_w$ . Figure IV.27 shows the build-up time as a function of  $\lambda_w$ . It was observed that the erasing rate decreased with increasing  $\lambda_w$ . Figure IV.28 shows the erasing rates as a function of time for all wavelengths used in this study. Notice the dramatic change in the erasing rate when  $\lambda_w$  was changed from 465.8 nm to 488 nm.

The experimental results of the scattered efficiency vs  $\lambda_w$  is shown in Figure IV.29. The scattered efficiency ( $\eta$ ) at  $\lambda_w=465.8$  nm is about 4 times larger than that at  $\lambda_w=472.7$  nm. The Figure shows that  $\eta$  decreases appreciably for values of  $\lambda_w$  larger than 465.8 nm and then it decreases slowly for large values of  $\lambda_w$ . The change in the index of refraction was deduced from the experimental value of  $\eta$  and the results of the theory presented in the theory section of this chapter. The transient component of the scattered signal decreased when  $\lambda_w$  increased. Table IV.10 shows the experimental values of the scattered power ( $P_s$ ), efficiency ( $\eta$ ), linear absorption ( $\alpha_w$ ), and the signal build-up time,  $t_{bl}$ . The calculated values of  $(\eta/\Delta n^2)$  and  $\Delta n$  are also shown.

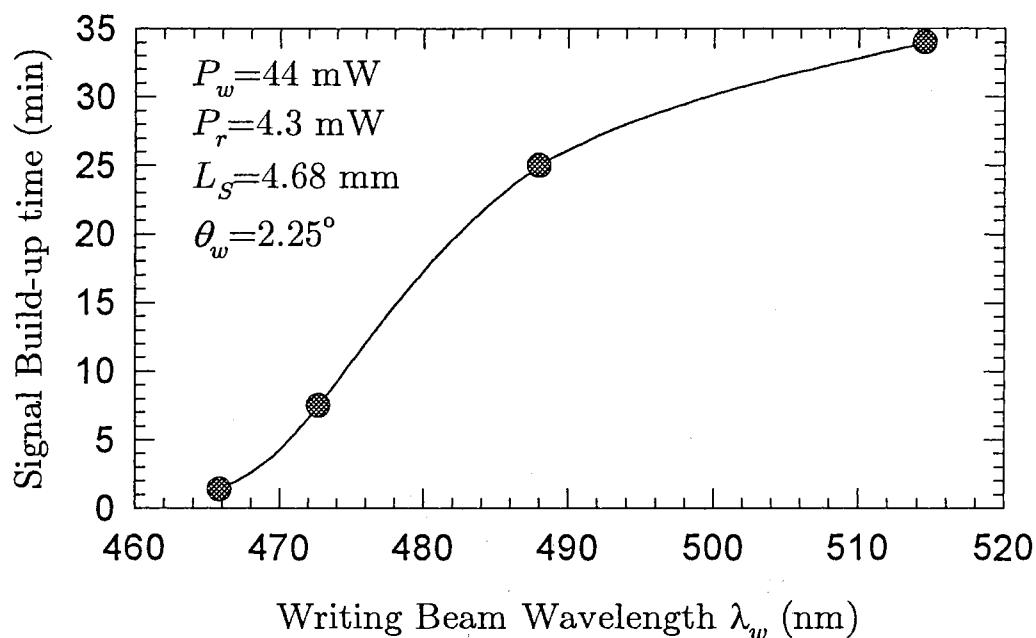


Figure IV.27. The signal build-up time as a function of the write-beam wavelength using B28. The solid line is guide to the eye.

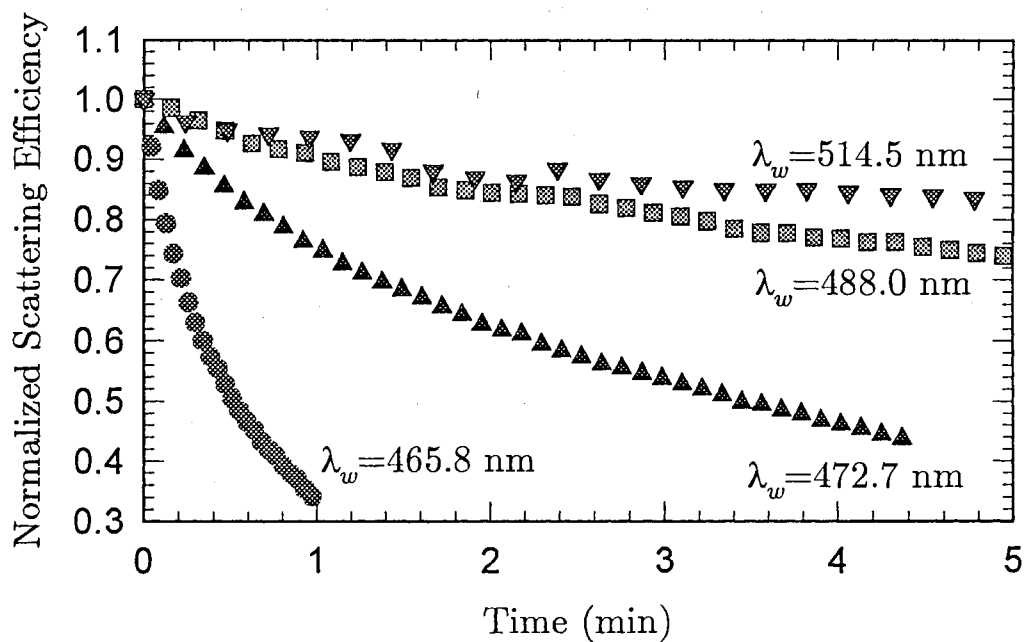


Figure IV.28. The erasing rates as a function of write-beam wavelength using B28. The normalization was done by dividing the data in each curve by the first data point.



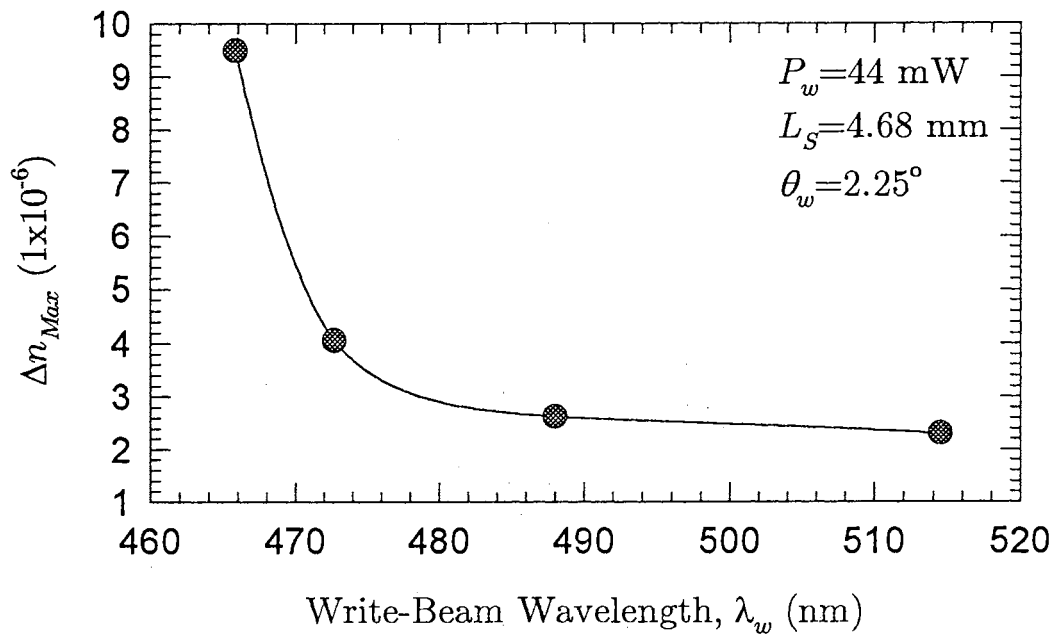


Figure IV.29. The scattered efficiency versus  $\lambda_w$  for B28 using  $\theta_w = 2.5^\circ$  and  $P_w = 44 \text{ mW}$ .

Table IV.10. Experimental results for B28 using  $P_w = 44 \text{ mW}$  and  $\theta_w = 2.5^\circ$ .

$\lambda_w$ (nm)	$\alpha_w$ ( $\text{cm}^{-1}$ )	$t_{bl}$ (min)	$P_s$ (nW)	$\eta$ ( $\times 10^{-5}$ )	$(\eta/\Delta n^2)$ ( $\times 10^{+6}$ )	$\Delta n$ ( $\times 10^{-6}$ )
465.8	1.16	1.4	450	10.5	1.16	9.49
472.7	0.38	7.5	118	2.74	1.67	4.06
488.0	0.29	25	52	1.24	1.80	2.63
514.5	0.21	34	19	0.45	1.96	2.31

## 5. Discussion

From previous [1] and recent [65] measurements it is clear that the rare-earth ions such as  $\text{Eu}^{3+}$  ions are essential elements in the grating formation in a variety of glass samples. Samples that contain  $< 1\%$  or  $0\%$   $\text{Eu}^{3+}$  do not produce any permanent grating. When exciting the  $\text{Eu}^{3+}$  ion to the  ${}^5\text{D}_2$  level, a decay to the lower  ${}^5\text{D}_J$  ( $J=0,1$ ) levels occurs via nonradiative decay processes [66,67]. The radiationless relaxation takes place through multiphonon emission of several high-energy phonons [67]. The energy level diagram for  $\text{Eu}^{3+}$  ion is shown in Figure IV.30. The high-energy phonons provide the thermal energy for some cations to hop to different sites in the glass network. These phonons can produce temperature changes on the order of  $\sim 10^3$  K [1]. The importance of these high-energy phonons appears from the results of the write-beam wavelength dependence. Moreover, if the  $\text{Eu}^{3+}$  ion is excited only to the  ${}^5\text{D}_0$  level, no permanent grating formation is detected [2]. In order to get the maximum number of phonons one needs to excite the  $\text{Eu}^{3+}$  ions resonantly using the 465.8 nm line from a cw Argon laser. The resonance excitation is important in obtaining a maximum Bragg diffracted power. However, the claim that permanent gratings cannot be formed and erased until the  $\text{Eu}^{3+}$  ions are resonantly excited [1-6] is not correct. Our results using different write-beam wavelength show that laser induced gratings can be written and erased using on- and off-resonance excitations. By pumping the  $\text{Eu}^{3+}$  ions with off-resonance radiation the number and the energy of the high-energy phonons decreases leading to a decrease in the number of cations having the potential to migrate. This in turn reduces the grating strength. Using off-resonance excitation causes the scattered power to

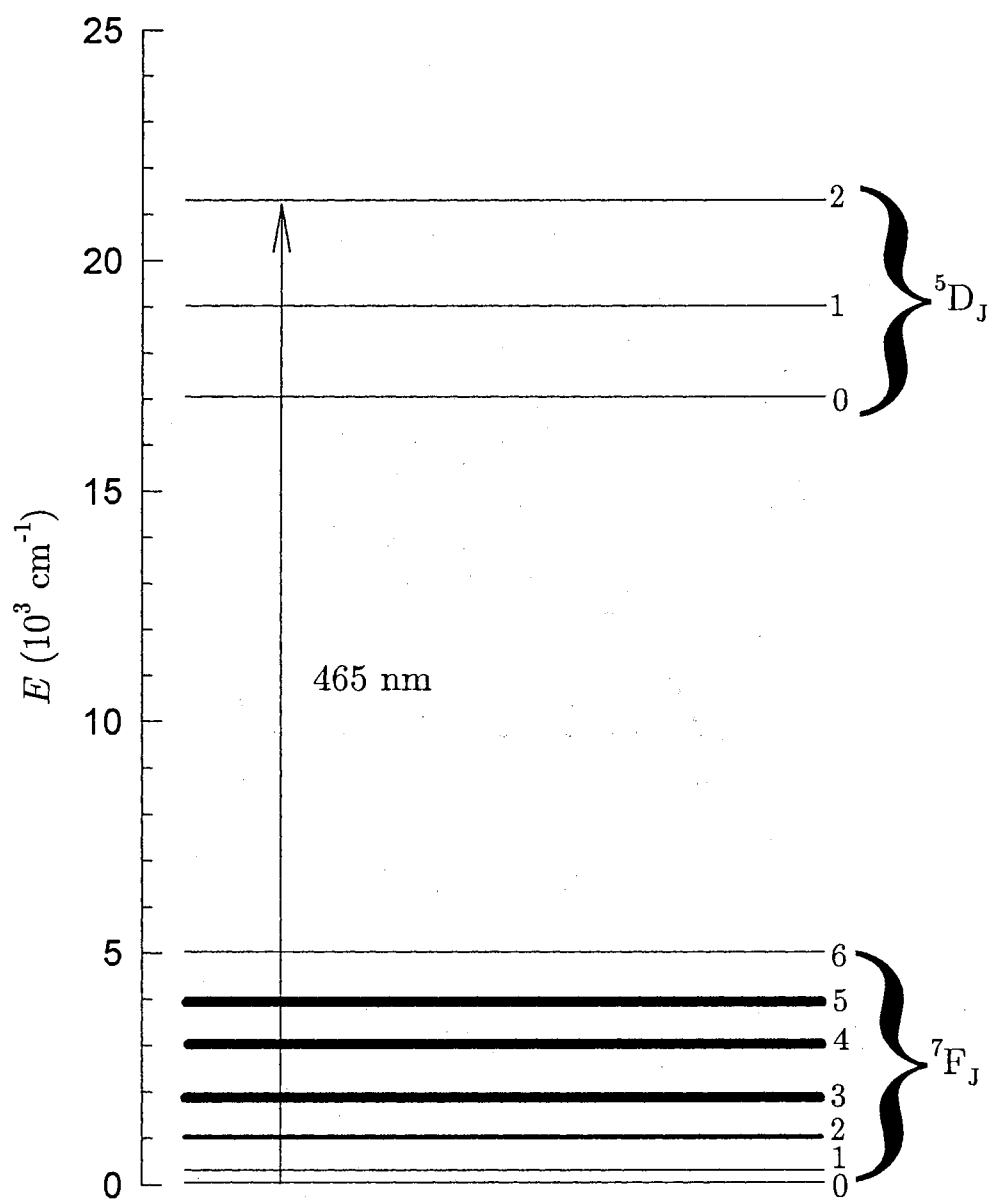


Figure IV.30. Partial energy level diagram for  $\text{Eu}^{3+}$  ion and the resonance transition to the  ${}^5\text{D}_2$  level.

decrease, the build-up time to increase, and the erasing rate to become slower.

Ionic conductivity measurements in some of these glasses [68] and the grating build-up time suggests that ionic migration from the bright regions towards the dark regions of the interference pattern is possible. It has been found that the activation energy of the ionic conduction of the alkali ions [69] decreases by adding Al to the glass composition. The scattered efficiency from samples that contain Al was found to be larger than the efficiency from samples that did not have Al [65]. The ionic migration will result in a structural change in the bright regions and in the region where these ions become trapped. This will affect the polarizability of both regions which in turn results in a change in the index of refraction. Photoionization of  $\text{Eu}^{3+}$  is not likely to be the mechanism responsible for the permanent grating formation because neither the exciting wavelength nor the pumping power is suitable to photoionize the  $\text{Eu}^{3+}$  ions.

Our results show that light cations ( $\text{Na}^+$ ,  $\text{Mg}^{2+}$ ,  $\text{Ca}^{2+}$ ) are the charges that are likely to migrate in the glass network. The fact that the diffracted power depends on the mass of the alkaline ions rules out the possibility that the electrons are the charges that move inside the glass.  $\text{Sr}^{2+}$  and  $\text{Ba}^{2+}$  cations seem not to participate in the migration process. This is to be expected, because these alkaline ions have large masses as compared to  $\text{Mg}^{2+}$  and  $\text{Ca}^{2+}$ . The results shown in Figure IV.19 suggests that  $\text{Ca}^{2+}$  ions participate in the migration process unlike  $\text{Sr}^{2+}$  and  $\text{Ba}^{2+}$  cations. If  $\text{Ca}^{2+}$  ions were not migrating from the bright regions then the efficiency of B16 should be similar to those of B18 and B20.

To explain our results and the role of the alkali and alkaline ions on the grating formation, we assume that the  $\text{Eu}^{3+}$  ion is responsible for creating the

high-energy phonons due to its radiationless transition from the  ${}^5D_2$  to  ${}^5D_0$  level. Since the thermal diffusion in glass is slow these high energy phonons will create nonthermalized vibrational energy around the  $\text{Eu}^{3+}$  ion which leads to a structural change in the local environment of the  $\text{Eu}^{3+}$ . As a result of the very high local temperature some of the cations (alkali and/or alkaline ions) will hop from the region of constructive interference (bright region) towards the region of destructive interference (dark regions). To help in explaining our results, we show a local region of the glass network including  $\text{Eu}^{3+}$ , alkali, and alkaline modifiers in Figure IV.31.

(a) Effect of the Second Alkaline Modifier

In general, we get strong grating formation (permanent and transient) if considerable number of cations are able to migrate from the bright regions towards the dark regions. This can be seen by comparing the efficiencies of the 16-family and the 22-family. The 16-family has a larger number of heavy alkalines as compared to the 22-family. This behavior is to be expected, because by increasing the number of the small-light ions like  $\text{Mg}^{2+}$  and, at the same time, decreasing the number of the heavier ions like  $\text{Ca}^{2+}$ , the system will have more mobile ions that can migrate.

To explain the effect of the second alkaline modifier we use the data of the 16-family. We noticed that the heavier these cations become, the smaller the scattering efficiency. When the concentration of the CaO is comparable to or exceeds that of the MgO, the efficiency will be affected in two ways:

(i) The number of cations that has the potential to migrate from the bright region is going to decrease because the  $\text{Ca}^{2+}$  ions are heavier, and thus, less mobile

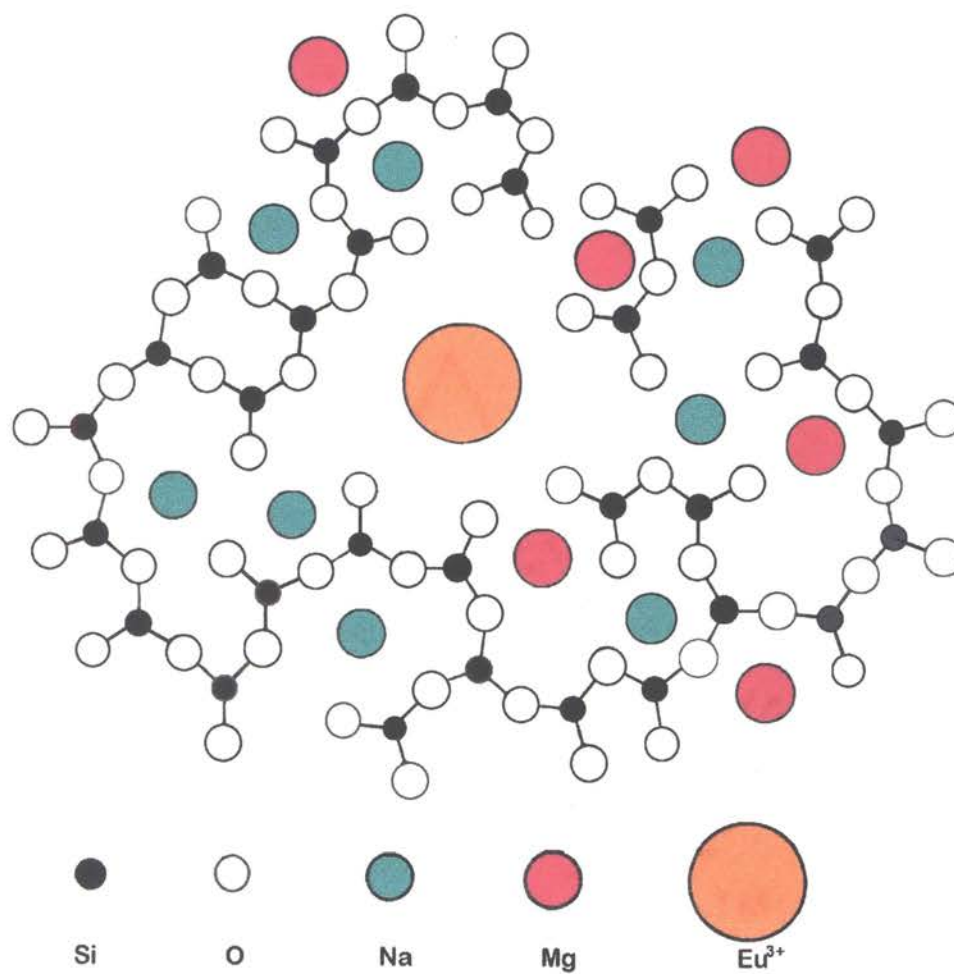


Figure IV.31. Schematic two-dimensional representation of the structure of silicate glass including Na, Mg, and Eu ions.

than the  $\text{Mg}^{2+}$  ions. In addition, the number of the  $\text{Mg}^{2+}$  ions has been reduced by the CaO substitution. Once again, it should be emphasized that  $\text{Sr}^{2+}$  and  $\text{Ba}^{2+}$  are too massive to undergo any appreciable hopping as can be seen from the results shown in Figure IV.19. The results of French *et al.* showed that the diffracted efficiency decreased as the mass of the alkaline ions increased [7].

(ii) The  $\text{Ca}^{2+}$  might occupy a significant number of sites near the  $\text{Eu}^{3+}$  ions which reduces the probability for the  $\text{Mg}^{2+}$  and/or  $\text{Na}^+$  ions to occupy these same sites. This reduces the number of  $\text{Mg}^{2+}$  and  $\text{Na}^+$  ions that might be able to migrate. Therefore, we should expect to see less diffracted power as the mass of the second alkaline ion increases. In one way or another the second alkaline modifier is competing with the  $\text{Mg}^{2+}$  and  $\text{Na}^+$  ions on the sites near the  $\text{Eu}^{3+}$ , especially when its concentration is equal or larger than that of the  $\text{Mg}^{2+}$  and  $\text{Na}^+$  ions.

For the 22-family which has 11.12% MgO and 1.17% CaO (SrO, BaO) the scattering efficiency was higher than that of the 16-family. This clearly shows the importance of the light ions like  $\text{Mg}^{2+}$  for the grating formation. For the 22-family the scattering efficiency was found to increase as the mass of the second alkaline ion increased, Figure IV.22. This seems to contradict what we just mentioned in the previous paragraph. However, by examining the situation carefully we find that there is no violation of what we just discussed. In the 22-family case we have larger number of the MgO than the second alkaline. This means that the main factor that affects the efficiency ( as far as the mobile ions) is the number of the  $\text{Mg}^{2+}$  ions. Then what is the role of the second alkaline ion? To answer this question we should recall the fact that when large cations are part of the glass network they stretch the structure [70-72] and the glass

structure becomes less rigid. This suggests that the  $\text{Mg}^{2+}$  and  $\text{Na}^+$  ions might move more easily as the second alkaline ion increases in size and mass. Also, notice that the number of the second alkaline ions is not as large as  $\text{Mg}^{2+}$  or  $\text{Na}^+$  ions. Therefore, the competition between the second alkaline ions and  $\text{Mg}^{2+}$  or  $\text{Na}^+$  for sites near the  $\text{Eu}^{3+}$  ions is not a major factor.

#### (b) Sodium Enriched Samples

When the sodium concentration was increased beyond 14.63% , the scattered power decreased. This increase in the number of  $\text{Na}_2\text{O}$  units was at the expense of the silicon concentration i.e., the number of  $\text{SiO}_2$  units decreased. The results of these samples seem to contradict what we stated in the beginning of this discussion ( the more mobile ions in the system, the more efficiency we get). That general statement is true but the relative concentration of these mobile ions has a limit after which the opposite behavior might be produced as in the case of sodium enriched samples. By increasing the concentration of  $\text{Na}_2\text{O}$ , the number of deep traps that are available for the ions that would migrate from the bright regions is smaller. Few of these available traps are deep, most are shallow. Therefore, many ions that migrate from the bright regions will be trapped in shallow traps. When the write-beams were blocked, the permanent grating for the sodium enriched samples decreased slowly over a period of 14 min, then leveled off. This observation seems to support the explanation discussed above since more ions can be thermally excited from the shallow traps. The fact that a strong electric field is created (because of the ion migration) some of the excited  $\text{Na}^+$  ions return to some sites in the previously bright regions. This means that the electrostatic attraction between the  $\text{Na}^+$  and the  $\text{O}^-$



will lead to a partial decay in the permanent grating. The results of B30, Figure IV.26(a), suggests that more shallow traps are available as the  $\text{Na}_2\text{O}$  concentration increased. The permanent decay of B30 is larger than that of B29. This means that more ions in the case of B30 were attracted to the negative charge in the bright regions. The results of B29 and B30 indicate that the number of empty traps (mainly deep traps) decreases as the  $\text{Na}_2\text{O}$  concentration increases. Therefore, larger numbers of the migrating ions will end up in shallow traps as can be seen from Figure IV.26(a). Our results suggest that the  $\text{Na}_2\text{O}$  concentration in the glass should be adjusted carefully.

### (c) Transient Grating

It is a fact that the transient diffracted power increases as the permanent grating strength increases. This means that the transient grating is coupled to the permanent grating. The fact that the transient decay time is the same as the fluorescence decay time ( as can be seen from Figure IV.12) of the  ${}^5\text{D}_0$ - ${}^7\text{F}_0$  of the  $\text{Eu}^{3+}$  ions suggests that the charge population of  ${}^5\text{D}_0$  state is responsible for creating the transient grating. However, the experimental results of the transient signal depends on the evolution of the permanent grating (see Figure IV.13). This might indicate that the transient grating is not due to a population grating because one expects the transient signal to be the same as long as the write-beam power is constant. However, we should keep in mind that the population grating in this case is not isolated from the effect of the permanent grating. Two contributions may be controlling the transient grating, the polarizability of the  $\text{O}^-$  ions and the local environment of the  $\text{Eu}^{3+}$  ions.

When the cations migrate towards the dark region they leave behind electrons attached to the nonbriding oxygens. If these electrons become perturbed, then the polarizability of the oxygen ions will change causing the index of refraction of the bright regions to change. A possible cause of perturbation is the fluorescence of the  $\text{Eu}^{3+}$  ion. This is consistent with the fact that the transient decay time is the same as that of the fluorescence (see Figure IV.12). Since the number of such nonbriding oxygen ions is proportional to the number of cations that migrate towards the dark regions, we expect the transient effect to increase as the permanent grating builds up. After blocking the write-beams the fluorescence of the  $\text{Eu}^{3+}$  vanishes as does the transient signal.

The local environment of the  $\text{Eu}^{3+}$  ions will change as a result of the ion migration. The interaction of the excited states of the  $\text{Eu}^{3+}$  ions with the environment controls the transient component of the index of refraction. The observed experimental results seem to support this explanation.

#### (d) Writing and Erasing the Grating

The results shown in Figure IV.11 clearly demonstrate that the erasing rate is dependent on the evolution of the permanent grating. As the permanent grating becomes stronger the erasing rate becomes slower. This can be understood in terms of ion migration. When one of the write-beams interacts with the grating region it excites both the bright and the dark regions. Both regions will be exposed to a uniform non-spatially modulated intensity. As a result, the high-energy phonons from the  $\text{Eu}^{3+}$  ions in the dark regions will provide the alkali and the alkaline ions, which have migrated to the dark regions, with the energy that enable them to hop back to sites in the bright regions. The attractive

electrostatic force between the positive ions and the negatively charged nonbriding oxygen's will help this kind of process to take place. However, it is not necessary that all ions go back to their original sites. This is probably the reason why the signal will not go back to its maximum value if the grating was erased after the signal reached its maximum as shown in Figure IV.8. When the erasing process takes place before the grating reaches its maximum value, two things might happen: First, the ions that start to migrate from the bright region toward the dark region have not migrated far away and this makes the return of those ions to the bright region easier and faster. Moreover, most likely these ions will return to their original sites because they are not far away from them. As the writing process continues, the ions move farther away from their original sites and may therefore end up in sites different from their original ones during the erasing process. In such a case the signal will not reach its previous level if we start to write again after erasing. Second, during the early stages of grating formation, the number of ions that start the migration process might not be the total possible number of ions that will migrate from the bright regions when the grating formation is completed. This picture explains how the grating strength affects both the erasing rate and the signal growth after erasing, provided the erasing took place during the signal build-up.

#### (e) Scattered Signal Saturation

In all samples we noticed that the scattered power started to saturate for  $P_w$  values larger than 28 mW. The concentration of the  $\text{Eu}^{3+}$  ions is the only common factor among all the samples studied via the FWM technique. This suggests that the saturation is related to the concentration of the  $\text{Eu}^{3+}$  ions.

When  $P_w=28$  mW almost all the  $\text{Eu}^{3+}$  ions in the bright regions are excited. This gives the maximum number of phonons which in turn leads to the maximum structural change possible. This is why the diffracted power did not change greatly for  $P_w > 28$  mW. The transient component of the scattered power showed a similar behavior, see Figures IV.15 and IV.21(b). These results support the previous explanation. If the all  $\text{Eu}^{3+}$  ions in the bright regions were excited then the population of the  ${}^5\text{D}_0$  levels should stay constant even if  $P_w$  is larger than 28 mW.

## CHAPTER V

### SUMMARY AND FUTURE WORK

In chapter II we presented experimental and theoretical results of self-defocusing and ring structure effects using CdTe single crystals. All experiments were performed at room temperature using nanosecond laser pulses at  $1.064 \mu\text{m}$ . The spatial and temporal profiles of the transmitted beam were found to be dependent on the input irradiance and the distance from the exit plane of the sample. Furthermore, the temporal profile results were dependent on the detected cross-sectional area of the transmitted laser beam. The transmitted spatial profile experienced broadening and ring structure formation while the temporal profile showed pulse compression and modulation. The nonlinear effects were attributed to the free carriers generated via two-photon absorption (TPA). We developed a theoretical model which successfully explained the experimental results. Moreover, we were able to deduce accurate values for the two-photon absorption coefficient, free carriers absorption cross section, the nonlinear refraction coefficient, and the recombination lifetime of the free carriers. Finally, we found that the effect of the sample is to encode a radially and temporally dependent phase shift which causes the reshaping as the pulse evolves in space and time.

In chapter III, we reported the results of optical switching including optical limiting and pulse compression using a CdTe etalon. The sample was

pumped with 11 ns pulses at  $1.064 \mu\text{m}$ . The input intensity required to achieve the switching was found to be dependent on the initial detuning of the etalon. In this study we only detected the on-axis transmission of the etalon such that a plane wave approximation could be used. For this purpose a pinhole was attached to the exit surface of the sample. To induce a nonlinear change in the index of refraction which controlled the transmission of the etalon was due to the free carriers generated by the two-photon absorption process. In the theoretical model we assumed that TPA took place during the first pass through the sample. This assumption is good, and accurately describes our results, since the sample surface reflectivity is small. If the sample reflectivity is 50% or more probably our model will not be able to predict the results accurately because TPA might take place during the second and the third passes through the sample. Therefore, it will be interesting to develop a model which considers TPA beyond the first pass through the sample.

We have investigated, via the four-wave mixing technique, the formation of the permanent and transient gratings in  $\text{Eu}^{3+}$ -doped silicate glasses. These measurements were performed using both on- and off-resonance frequencies from a cw argon-ion laser. The scattering efficiency, the grating build-up, and the grating erasure were investigated as a function of the write-beam wavelength, power, and crossing angle for several glass compositions. The diffracted power was found to be dependent on the concentration and the type of the alkaline ions. The decay time of the transient component of the scattered signal was found to be the same as the fluorescence decay time (2.3 ms). Therefore, we concluded that transient grating is attributed to the population grating of the excited  $\text{Eu}^{3+}$  ions. However, this population grating is controlled by the perma-

ment changes that occur around the  $\text{Eu}^{3+}$  ions as a result of the ion migration from the regions of constructive interference. The permanent grating was attributed to a structural change of the glass in the local environment of the  $\text{Eu}^{3+}$  ions. A theoretical model was developed to deduce the nonlinear change in the index of refraction from the experimental diffracted efficiency. The model considers the diffraction due to the incidence of a probe Gaussian beam on volume grating formed by two intersecting Gaussian beams.

The results of the 22-family showed that very small concentrations of the second alkaline ions increased the diffracted efficiency. Therefore, mixed alkaline ions should be adjusted carefully in order to improve the permanent grating formation. From the results of the sodium enriched samples we found that for a  $\text{Na}_2\text{O}$  concentration increased above 15%, the diffracted efficiency decreased. Moreover, the permanent grating was found to decay slowly. These results suggest that the sodium concentration should be adjusted carefully with respect to the rest of the glass constituents.

For future experiments, it is important to use samples with similar thicknesses in order to compare their grating build-up time and erasing rates. In addition, this will enable the researcher to compare the samples according to their experimental efficiency. The grating was observed to decay slowly if the write-beams were kept on after the diffracted signal reached its maximum. The explanation of this behavior is still unknown. More experimental work is needed in order to understand the physical origin of this decay.

## BIBLIOGRAPHY

1. F. M. Durville, E. G. Behrens, and R. C. Powell, Phys. Rev. B 34, 4213 (1986).
2. F. M. Durville, E. G. Behrens, and R. C. Powell, Phys. Rev. B 35, 4109 (1987).
3. E. G. Behrens, F. M. Durville, and R. C. Powell, Opt. Lett. 11, 653 (1986).
4. E. G. Behrens, F. M. Durville, and R. C. Powell, Phys. Rev. B 39, 6076 (1989).
5. E. G. Behrens, R. C. Powell, and D. H. Blackburn, Appl. Opt. 29, 1619 (1990).
6. E. G. Behrens, R. C. Powell, and D. H. Blackburn, J. Opt. Soc. Am. B 7, 1437 (1990).
7. V. A. French, R. C. Powell, D. H. Blackburn, and D. C. Cranmer, J. Appl. Phys. 69, 913 (1991).
8. H. M. Gibbs, *Optical Bistability: Controlling Light with Light* (Academic, New York, 1985).
9. V. V. Arsen'ev, V. S. Dneprovskii, D. N. Klyshko, and A. N. Penia, Sov. Phys. JETP 29, 413 (1969).
10. T. F. Boggess, S. C. Moss, I. W. Boyd, and A. L. Smirl, Opt. Lett. 9, 291 (1984).
11. D. Weaire, B. S. Wherrett, D. A. B. Miller, and S. D. Smith, Opt. Lett. 4, 331.
12. S. Guha, E. W. Van Stryland, and M. J. Soileau, Opt. Lett. 10, 285 (1985).
13. M. Sheik-Bahae, and H. Kwok, IEEE J. Quantum Electron. QE-23, 974 (1987).
14. J. R. Milward, W. Ji, A. K. Kar, C. R. Pidgeon, and B. S. Wherrett, J. Appl. Phys. 69, 7351 (1991).
15. W. Ji, A. K. Kukawadia, Z. C. Feng, and S.H. Tang, J. Appl. Phys. 75, 3340.



16. H. J. Eichler, F. Massmann, and Ch. Zaki, *Optics Commun.* 40, 302 (1982).
17. H. J. Eichler, J. P. Heritage, and F. A. Beisser, *IEEE J. Quantum Electron.* QE-2351 (1981).
18. E. W. Van Stryland, H. Vanherzeele, M. A. Woodall, A. L. Smirl, S. Guha, and F. Boggess, *Optical Engineering* 24, 613 (1985).
19. D. H. Auston, S. McAfee, C. V. Shank, E. P. Ippen, and O. Teschke, *Solid-State Electronics* 21, 147 (1978).
20. M. S. Petrovic, A. Suchocki, R. C. Powell, G. Cantwell, and J. Aldridge, *Appl. Phys. Lett.* 56, 1632 (1990).
21. S. A. Akhmanov, R. V. Khokhlov, and A. P. Sukhorukov, in *Laser Handbook*, edited by F. T. Arecchi and E. O. Shulz-Dubois (North-Holland, Amsterdam, 1972), p. 383.
22. P. Mukherjee, M. Sheik-Bahae, and H. S. Kwok, *Appl. Phys. Lett.* 46, 770 (1985).
23. B. Taheri, A. Munoz F., R. C. Powell, J. J. Song, and J. K. Furdyna, "Nonlinear Optical and Transport Properties of CdMnSe and CdMnTe", in *Nonlinear Optical Materials for Switching and limiting*, SPIE 2229, p.12 (1994).
24. C. F. Gerald, and P. O. Wheatley, *Applied Numerical Analysis*, 4<sup>th</sup> ed (Addison-Wesley, New York, 1989).
25. M. Born, and E. Wolf, *Principles of Optics*, 5<sup>th</sup> ed (Pergamon, Oxford, 1975), p. 383.
26. *Handbook of Mathematical Functions*, edited by Milton Abramowitz and Irene A. Stegun, Dover publications, Inc., New York, 1965.
27. M. Sparks, *J. Appl. Phys.* 42, 5029 (1971).
28. J. M. Grasyuk, I. G. Zubarev, A. B. Mironov, and I. A. Poluektov, *Sov. Phys. Semicond.*, 10, 159 (1976).
29. M. Bass, E. W. Van Stryland, and A. F. Stewart, *Appl. Phys. Lett.*, 34, 142 (1979).
30. A. A. Said, M. Sheik-Bahae, D. J. Hagan, T. H. Wei, J. Wang, J. Young, and E. W. Van Stryland, *J. Opt. Soc. Am. B* 9, 405 (1992).
31. B. S. Wherrett, A. C. Walker, and F. A. P. Tooley, in *Optical Nonlinearities and Instabilities in Semiconductors*, edited by H. Haug (Academic, New York, 1988 ), p. 239.
32. M. S. Petrovic, A. Suchocki, R. C. Powell, G. Cantwell, and J. Aldridge, *J. Appl. Phys.* 66, 1359 (1989).

33. J. H. Bechtel and W. L. Smith, Phys. Rev. B 13, 3515 (1976).
34. I. M. Catalano, A. Cingolani, M. Ferrara, and M. Lugara, Solid State Commun. 49, 597 (1984).
35. J. M. Ralston and R. K. Chang, Opto-electronics 1, 182 (1969).
36. A. Vaidyanathan, T. W. Walker, A. H. Guenther, S. S. Mitra, and L. M. Narducci, Phys. Rev. B 21, 743 (1980).
37. D. C. Hutchings and E. W. Van Stryland, J. Opt. Soc. Am. B 9, 2065 (1992).
38. M. H. Weiler, Solid State Commun. 39, 937 (1981).
39. N. G. Basov, A. Z. Grasyuk, I. G. Zubarev, V. A. Katulin, and O. N. Krokhin, Sov. Phys. JETP 23, 366 (1966).
40. A. Vaidyanathan, A. H. Guenther, and S. S. Mitra, Phys. Rev. B 24, 2259 (1981).
41. Gibbs, S. L. McCall, and T. N. C. Venkatesan, Phys. Rev. Lett., 36, 1135-2238, (1976).
42. See, *Optical Bistability*, edited by C. M. Bowden, H. M. Gibbs, and S. L. McCall, (Plenum, NY, 1984).
43. D. A. B. Miller, S. D. Smith, and A. Johnston, Appl. Phys. Lett., 35, 658-660, (1979).
44. H. M. Gibbs, S. L. McCall, T. N. C. Venkatesan, A. C. Gossard, A. Passner, and W. Wiegmann, Appl. Phys. Lett., 35, 451-453, (1979).
45. D. Craig, A. K. Kar, J. Gordon, H. Mathew, and A. Miller, IEEE J. Quantum Electron. QE-21, 1363, (1985).
46. F. Fidorra, M. Wegener, J. Y. Bigot, B. Honerlage, and C. Klingshirn, J. Lumin, 35, 43, (1986).
47. W. Ji, A. K. Kar, J. Gordon, H. Mathew, and A. C. Walker, IEEE J. Quantum Electron. QE-22, 369, (1986).
48. C. R. Paton, Z. Xie, and J. M. Hvam, J. Opt. Soc. Am. B., 7, 1225, (1990).
49. W. D. St. John, J. P. Wicksted and G. Cantwell, J. Appl. Phys. 73, 3013 (1993).
50. C. Klingshirn, K. Bohnert, and H. Kalt, "Optically nonlinear and bistable behavior of direct of direct gap semiconductors," AGARD

- workshop on " Digital optical circuit technology," Schliersee, West Germany, Sept. (1984).
51. Y. K. Park, "  $\text{Hg}_{1-x}\text{Cd}_x\text{Te}$  nonlinear Fabry-Perot filters for optical limiting at  $10.6 \mu\text{m}$ ," in *Conference on Laser and Electro-Optics, Technical Digest*, (IEEE, New York, 1984). p.178.
  52. W. Ji, J. R. Milward, A. K. Kar, B. S. Wherrett, and C. R. Pidgeon, *J. Opt. Soc. Am. B*, 7, 868, (1990).
  53. A. Miller, D. Craig, and G. Steward, " Room-temperature optical nonlinearities and bistability in  $\text{CdHgTe}$  and  $\text{CdTe}$ ," in *Optical Bistability III*. (Springer-Verlag, Berlin, Germany, 1986). p. 140.
  54. B. E. A. Saleh and M. C. Teich, *Fundamentals of Photonics*, (John Wiley & sons, INC, New York, 1991).
  55. A. E. Siegman, *Lasers*, (University Science Books, Mill Valley, California, 1986). p. 732.
  56. G. Hernandez, *Fabry-Perot Interferometers*, (Cambridge, London, 1986).
  57. In literature (see for example Refs. 6 and 8) authors define the total phase shift  $\Delta\phi(t)$  as the sum of the initial detuning of the etalon,  $\phi_o$ , plus the nonlinear phase shift,  $\phi(t)$ . However, the above approximated definition of  $\Delta\phi(t)$  is valid and is equivalent to the following expression 
$$\Delta\phi(t) = (4\pi / \lambda)L\sqrt{[n_o + \Delta\bar{n}(t)]^2 - \text{Sin}^2(\theta_i)}$$
 provided  $|\Delta\bar{n}(t)| \ll n_o$  and  $\theta_i$  is small. By expanding this expression one can show easily that  $\Delta\phi(t)$  is the sum of Eqs (2) and (3) in the text.
  58. A. Y. Hamad, J. P. Wicksted, S. Y. Wang, and G. Cantwell, *J. Appl. Phys.* 78, 2932 (1995).
  59. M. Sheik-Bahae, A. A. Said, T. H. Wei, D. J. Hagan, and E. W. Van Stryland, *IEEE J. Quantum Electron.* 25, 760, (1990).
  60. A. Munoz, R. J. Reenes, B. Taheri, and R. C. Powell, *J. Chem. Phys.* 98, 6083, (1993).
  61. M. M. Broer, A. J. Bruce, and W. H. Grodkiewicz, *J. Lumin.* 53, 15, (1992).
  62. M. M. Broer, A. J. Bruce, and W. H. Grodkiewicz, *Phys. Rev. B* 45, 7077 (1992).
  63. H. J. Eichler, P. Gunter, and D. W. Pohl, *Laser Induced Dynamic Grating* (Springer-Verlag, Berlin, 1986).
  64. A. E. Siegman, *J. Opt. Soc. Am.*, 67, 545, (1977).

65. C. Porter (private communication).
66. R. Reisfeld, *In Structure and Bonding*, edited by J. D. Dunitz (Springer-Verlag, Berlin, Germany, 1975), p. 123.
67. C. B. Layne, W. H. Lowdermilk, and M. J. Weber, *Phys. Rev. B* 16, 10 (1977).
68. G. S. Dixon (private communication).
69. C. H. Hsieh and H. Jain, *J. Non-Cryst. Solids*, 183, 1, (1995).
70. I. Yasui, H. Hasegawa, and M. Imaoka, *Phys. Chem. Glasses*, 24, 65, (1983).
71. I. Yasui, Y. Akasaka, H. Inoue, *J. Non-Cryst. Solids*, 177, 91, (1994).
72. G. H. Gangwere, "Brillouin Scattering in  $\text{Eu}^{3+}$  -Doped Alkali-Silicate Glasses," Dissertation, Department of Physics, Oklahoma State University (1990).

## APPENDICES

## APPENDIX A

### DERIVATION OF EQUATION (II.1)

The aim of this appendix is to derive Eq. (II.1) starting from the nonlinear equation in the following form

$$\nabla^2 \mathbf{E}(\vec{r}, t) = \mu_o \sigma \frac{\partial \mathbf{E}(\vec{r}, t)}{\partial t} + \mu_o \varepsilon \frac{\partial^2 \mathbf{E}(\vec{r}, t)}{\partial t^2} + \mu_o \frac{\partial^2 \mathbf{P}^{(NL)}(\vec{r}, t)}{\partial t^2}. \quad (\text{A.1})$$

$\mu_o$  is the permeability of free space,  $\varepsilon$  the dielectric constant of the material, and  $\sigma$  is the conductivity. The electric field and the nonlinear polarization are defined as

$$\mathbf{E}(\vec{r}, t) = E(\vec{r}, t) e^{-i(\omega t - kz)} + c.c \quad (\text{A.2})$$

$$\mathbf{P}^{(NL)}(\vec{r}, t) = P^{(NL)}(\vec{r}, t) e^{-i(\omega t - kz)} + c.c \quad (\text{A.3})$$

where  $E(\vec{r}, t)$  and  $P^{(NL)}(\vec{r}, t)$  are complex amplitudes. To simplify Eq. (A.1) we need to carry out the derivatives with respect to  $z$  and  $t$  using Eqs. (A.2) and (A.3). The derivatives with respect to  $x$  and  $y$  can be ignored for the case where the laser beam waist is approximately constant inside the sample i.e., thin sample approximation.

$$\frac{\partial \mathbf{E}}{\partial z} = \left( \frac{\partial E}{\partial z} + ikE \right) e^{-i(\omega t - kz)} \quad (\text{A.4})$$

$$\frac{\partial^2 \mathbf{E}}{\partial z^2} = \left( \frac{\partial^2 E}{\partial z^2} + i2k \frac{\partial E}{\partial z} - k^2 E \right) e^{-i(\omega t - kz)} \quad (\text{A.5})$$

The derivatives with respect to time will give

$$\frac{\partial \mathbf{E}}{\partial t} = \left( \frac{\partial E}{\partial t} - i\omega E \right) e^{-i(\omega t - kz)} \quad (\text{A.6})$$

$$\frac{\partial^2 \mathbf{E}}{\partial t^2} = \left( \frac{\partial^2 E}{\partial t^2} - i2\omega \frac{\partial E}{\partial t} - \omega^2 E \right) e^{-i(\omega t - kz)} \quad (\text{A.7})$$

By using the slowly varying amplitude approximation we can rewrite Eqs. (A.5) and (A.7) as

$$\frac{\partial^2 \mathbf{E}}{\partial z^2} = \left( i2k \frac{\partial E}{\partial z} - k^2 E \right) e^{-i(\omega t - kz)} \quad (\text{A.8})$$

$$\frac{\partial^2 \mathbf{E}}{\partial t^2} = \left( -i2\omega \frac{\partial E}{\partial t} - \omega^2 E \right) e^{-i(\omega t - kz)} \quad (\text{A.9})$$

In a similar manner the second time derivative of the polarization can be expressed as

$$\frac{\partial^2 \mathbf{P}}{\partial t^2} = \left( -i2\omega \frac{\partial P}{\partial t} - \omega^2 P \right) e^{-i(\omega t - kz)} \quad (\text{A.10})$$

By substituting Eqs. (A.6), (A.8), (A.9), and (A.10), in Eq. (A.1) we obtain

$$i2k \frac{\partial E}{\partial z} - k^2 E = -i\omega\mu_o\sigma E - \mu_o\varepsilon\omega^2 E - \mu_o\omega^2 P^{(NL)} \quad (\text{A.11})$$

Because  $k = \omega(\mu_o\varepsilon)^{1/2}$  the second term in both the right-hand side and the left-hand side of Eq. (A.11) are equal, hence cancel each other. The complex amplitude of the nonlinear polarization is define in term of the third order nonlinear susceptibility,  $\chi^{(3)}$ , as

$$P^{(NL)} = \frac{3}{4} \varepsilon_o \chi^{(3)} |E|^2 E \quad (\text{A.12})$$

Finally, by substituting Eq. (A.12) in Eq. (A.11) and replacing  $k$  by  $(\omega n_o/c_o)$  we obtain the desired result

$$\frac{\partial E}{\partial z} = \left( -\frac{\sigma \mu_o c_o}{2n_o} + i \frac{\omega}{4n_o c_o} \chi^{(3)} |E|^2 \right) E \quad (\text{A.13})$$



## APPENDIX B

### DERIVATION OF $I_{cr}$

In this Appendix we derive an expression to estimate the critical irradiance at which two-photon absorption (TPA) and free carriers a absorption (FCA) are equal. This means that the attenuation due to TPA is equal to that due to FCA. By substituting the relation

$$\beta I(1-R) = \sigma_{fc}N \quad (\text{B.1})$$

in Eq. (II. 8) we obtain

$$\frac{\partial N}{\partial t} = \beta \left( \frac{(1-R)^2}{2\hbar\omega} I^2 - \frac{(1-R)}{\sigma_{fc}\tau} I \right). \quad (\text{B.2})$$

Where R is the reflectivity of the sample. Assume that the laser pulse has a Gaussian temporal profile given by  $I=I_o \exp(-t/t_o)^2$  then Eq. (B.2) can be integrated to give

$$N_{\max} = \beta t_o I_{cr} \sqrt{\pi} (1-R) \left( \frac{(1-R)I_{cr}}{\sqrt{8\hbar\omega}} - \frac{1}{\sigma_{fc}\tau} \right) \quad (\text{B.3})$$

In Eq. (B.3) we used  $I_{cr}$  to denote the critical irradiance that is the maximum input irradiance at which TPA=FCA. Now, we find the desired expression by using Eq. (B.1) in the last result.

$$I_{cr} = \frac{\hbar\omega}{\sigma_{fc}t_o(1-R)} \sqrt{\frac{8}{\pi}} \left( 1 + \frac{t_o\sqrt{\pi}}{\tau} \right). \quad (\text{B.4})$$

From the last equation one can estimate the critical irradiance at which FCA=TPA. In our case  $\tau=12$  ns,  $t_o=6$  ns,  $\sigma_{fc}=25\times 10^{-18}$  cm<sup>3</sup>, and  $\hbar\omega=1.17$  eV which gives  $I_{cr}=5$  MW/cm<sup>2</sup>. This result is consistent with what we observe experimentally. Moreover, it supports the argument made in the theory section of chapter II that the FCA is important at all intensities that we have used. In fact, the FCA becomes the dominant mechanism of attenuation for intensities larger than 5 MW/cm<sup>2</sup>, see the figure bellow. For a shorter pulse duration, picosecond or femtosecond pulses, the critical irradiance can be reduced to,

$$I_{cr} = \frac{\hbar\omega}{\sigma_{fc} t_o} \sqrt{\frac{8}{\pi}} \quad (\text{B.5})$$

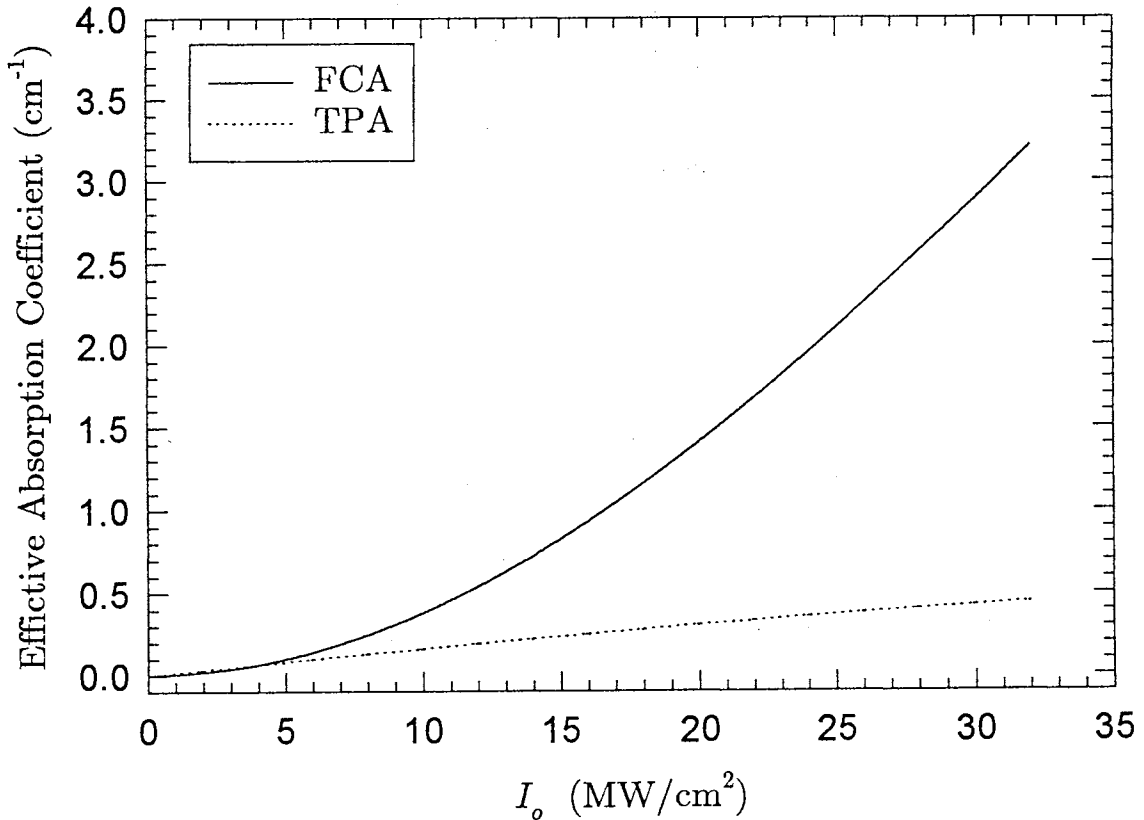


Figure B.1. The maximum effective absorption coefficients due to TPA ( $\beta I_{max}$ ) and FCA ( $\sigma_{fc} N_{max}$ ) as a function of peak input irradiance. This result was calculated using the theory presented in chapter II.

## APPENDIX C

### REFRACTIVE INDEX MEASUREMENTS USING A CCD

#### 1. Introduction

It is well known in optics that the refractive index of materials can be measured by the Brewster's angle experiment. It is usually performed to get a quick estimate of the refractive index to about one or two decimal places. The technique requires one polished surface and can be done on both transparent and opaque materials. At the Brewster's angle, the intensity of the reflected light is a minimum since only s-polarized light is reflected. This intensity change, as one rotates through the Brewster's angle, can be monitored by eye. We have found that by introducing a CCD camera with a laser beam profiler to monitor the intensity change, we can isolate the angle close to the resolution of the sample rotation stage. By using the relation  $n = \tan \theta_B$ , the refractive index is easily found. The uncertainty in the refractive index measurement is typically in the third decimal place.

#### 2. Procedure

The experimental setup is very simple and can be quickly assembled and is shown in figure C.1. Apart from the sample and laser source, the experiment requires the following: sample holder, rotation stage, CCD camera connected to a laser beam profiler, and neutral density filters to attenuate the beam going

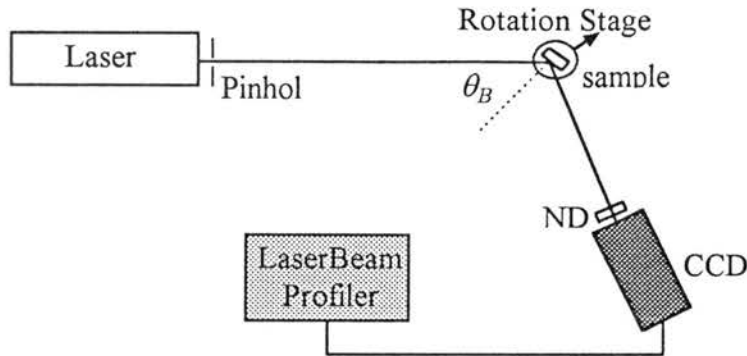


Figure C.1. Setup for measuring the refractive index using a CCD camera and laser beam profiler. The pinhole is used to align the back-reflected diffraction rings.

into the camera. It is very important to make sure the incident laser beam is perpendicular to the sample surface since the Brewster's angle is measured with respect to this normal. This can be easily accomplished by aligning the back-reflected beam with the incident one. However, to be more accurate, we place a pinhole concentric with the incident laser beam and close to the laser source. We align the back-reflected diffraction rings so that they are properly centered on the pinhole. The greater the distance between the sample and the pinhole the greater the assurance the beam is normal to the sample. We can therefore eliminate (or minimize) the uncertainty in our Brewster's angle measurements that comes from initially non-normal beams. The pinhole can subsequently be removed or a variable aperture can be used in its place.

We now carefully rotate the sample and place a card about 10 to 20 cm from it and monitor the change in the reflected intensity by eye. Once we approximately find this angle from the surface normal, we move the CCD camera in place. By making small rotational increments, we can see the intensity dip

through a minimum on the monitor of the laser beam profiler as we rotate through the Brewster's angle. This reflected intensity change can be observed on the monitor of the beam profiler as a change in the color of the cross-section of the beam and also the peak intensity of the beam profile. We can adjust the gain and background level on the camera and accurately find the angle close to the resolution of our rotation stage which is  $0.01^\circ$ .

### 3. Discussion

The introduction of the CCD camera along with the laser beam profiler makes the detection of the Brewster's angle simple to do. The fact that the CCD camera has a larger effective detection area than most photodiodes and PMT's and the fact that the reflected beam does not have to be centered on this area makes the CCD camera a better choice for this experiment. We can easily scan through the Brewster's angle without having to adjust the camera position. This is particularly advantageous since the reflectivity near the vicinity of the Brewster's angle is a very shallow function. In addition, we can adjust the gain and background level on the camera to better isolate the angle.

We have used this technique to measure the refractive indices of various materials. For example, we found the refractive index of a fused quartz sample with this method that had previously been measured with the minimum deviation technique. At 514.5 nm, the Brewster's angle was found to be  $55.63^\circ \pm 0.05^\circ$  giving a refractive index of  $n = 1.462 \pm 0.003$ . This compares quite well with the previously measured  $n = 1.462 \pm 0.001$ . The uncertainty reported is larger than that of the minimum deviation technique because we found it hard to accurately isolate the Brewster's angle any better than  $\pm 0.05^\circ$  due to laser

fluctuations. The reason for this is that the monitored reflected intensity change is the determining criteria for the Brewster's angle. With better laser stability, it should be possible to push the uncertainty to  $\pm 0.001$ .

#### 4. Conclusion

Although we found a slightly larger uncertainty in our refractive index measurements than the standard minimum deviation technique, we can perform the experiments relatively quickly. We also avoid the time-consuming sample preparation that is needed with the minimum deviation technique since only one polished surface is required with the Brewster's angle method. The ease, quickness and accuracy with which the experiment can be performed make this an attractive method for measuring the refractive index of materials.

## APPENDIX D

### PROGRAM FOR THE THEORY IN CHAPTER II

PROGRAM Spatial\_Temporal (INPUT,OUTPUT,INPUT1);

CONST

Y5=0;  
Ei=1.05;  
D=2.6781E+24;        {1/2hv}  
D1=0.136;  
No=2.84;  
Co=2.99E+10;  
Eo=8.8542E-16;  
N2=0;  
Sr=-6E-21;  
PI=3.1415927;  
Ro=0.0215;  
So=50;  
Tp=27E-12;  
Ne=4.3E+15;  
Cr=0;  
C=0;{8.3E+7;}  
Z=6;  
t0=0.17;  
t1=0.25;  
A=0.3;  
B=0.022;  
S=25E-18;  
Diff=0.06;  
Lam=1.064E-4;  
Ref1=0.23;  
Ref2=0.0025;

VAR

N:Array[0..902,0..905] OF Real;  
ph,Iout:Array [0..905,0..905] OF Real;  
Int: Array [1..7] OF Real;  
F:Array [1..7,0..1505] OF Real;  
N0,N01,I01,I02,I03,I04,I05,I06,

```

I11,I12,I13,I14,I15,I16,SUM,THICK,
P1,X1,Y1,Z1,L,h,h11,t,r1,r,A1,A2,A4,
B1,Io,Jo,h1,h2,h3,Z2,E,X,P,Y,Ere,Eim,
Isp,Theta,Y3,Fen:Real;
J,I,M,Q,Q1,Q3,L2,S1,S2,S3,S11:Integer;
input1:text;

```

```
{LOOP CONTROL VARI-
```

```
ABLS}
```

```
Procedure RUNGE_KUTTA_F ;
```

```
VAR
```

```
  K1,K2,K3,K4,K5,K6,G2,G3,G4,G5,G6:Real;
```

```
Begin
```

```
  K1:= h*(B * D* Sqr(I01) + Y5*2*D*A*I01 - C* (N01 - Ne)-
    Cr*SQR(N01))*1E-10;
```

```
  G2:= K1/4;
```

```
  K2:= h*(B*D*Sqr(I02) + 2*Y5*D*A*I02 - C*(N01+G2-Ne)-
    Cr*SQR(N01+G2))*1E-10;
```

```
  G3:= 3*K1/32 + 9*K2/32;
```

```
  K3:= h*(B*D*Sqr(I03) + 2*Y5*D*A*I03 - C*(N01+G3-Ne)-
    Cr*SQR(N01+G3))*1E-10;
```

```
  G4:= 1932*K1/2197-7200*K2/2197+7296*K3/2197;
```

```
  K4:= h*(B*D*Sqr(I04) + 2*Y5*D*A*I04 - C*(N01+G4-Ne)-
    Cr*SQR(N01+G4))*1E-10;
```

```
  G5:= 439*K1/216-8*K2+3680*K3/513-845*K4/4104;
```

```
  K5:= h*(B*D*Sqr(I05) + 2*Y5*D*A*I05 - C*(N01+G5-Ne)-
    Cr*SQR(N01+G5))*1E-10;
```

```
  G6:= 2*K2-8*K1/27-3544*K3/2565+1859*K4/4104-11*K5/40;
```

```
  K6:= h*(B*D*Sqr(I06) + 2*Y5*D*A*I06 - C*(N01 + G6-Ne)-
    Cr*SQR(N01+G6))*1E-10;
```

```
  N0:= N01+16*K1/135+6656*K3/12825 + 28561*K4/56430.0 - 9*K5/50 + 2*K6/55;
```

```
End;
```

```
PROCEDURE Bessel;
```

```
VAR A3,V,J1,J2:Integer;
```

```
  Fect,Cra:Real;
```

```
Begin
```

```
  IF ABS(2*A1*r1*r)< 5 Then
```

```
    Begin
```

```
      IF (r1=0) OR (r=0) Then
```

```
        Begin
```

```
          Jo:=1;
```

```
        End
```

```
      Else
```

```
        Begin
```

```
          Jo:=0;
```



```

For V:=0 To 10 Do
  Begin
    IF V=0 Then
      Begin
        Fect:=1;
      End
    Else
      Begin
        Fect:=1;
        For J1:=1 To V Do
          Begin
            Fect:=Fect*J1;
          End;
        End;
      IF Odd(V) Then
        Begin
          A3:=-1;
        End
      Else
        Begin
          A3:=1;
        End;
      IF V=0 Then
        Cra:=1
      Else
        Begin
          Cra:=1; {POWER}
          For J2:=1 To (2*V) Do
            Begin
              Cra:=(A1*r1*r)*Cra;
            End; {POWER}
          End;
          Jo:=Jo + (A3/SQR(Fect))*Cra;
        End;
      End;
    End
  End
Else
  Jo:=(SQRT(2/(PI*2*A1*r1*abs(r)))*Cos(2*A1*r1*r-(PI/4)));
End;

```

```
PROCEDURE SIMPSON;
```

```
VAR
```

```
G:Real;
```

```
L1,U:Integer;
```

```
G1:Array [1..1505] OF Real;
```

```

Begin
  G1[1]:=F[L2,1] + 3*F[L2,2] + 3*F[L2,3];
  L1:=3;
  For U:=2 To S11 Do
    Begin
      G1[U]:=2*F[L2,L1+1] + 3*F[L2,L1+2] + 3*F[L2,L1+3];
      L1:=L1 + 3;
    End;
  G:=0;
  For U:=1 To S11 Do
    Begin
      G:=G + G1[u];
    End;
  Int[L2]:=(3*h11/8)*(G + F[L2,3*S11+1]);
End;

```

```

Begin {Main}
{ Reset(input1);
  For i:=1 To 6 Do
    Begin}
  Y3:=1.22*PI/Diff;
t:=-0.6;
  S1:=50;
  S2:=50;
  S3:=50;
  r1:=0;
  h:=1.2/(3*So);
  h1:=Diff/(3*S1);
  h3:=PI/(3*S3);
  L:=D1/(3*S2);
  A1:=PI/(Lam*Z);
  A2:=(2*PI*Sr)/Lam;
  A4:=80*PI*PI*N2/(Co*No*1E+6*Lam);
  B1:=2*A1*SQR(2/(Eo*Co));
{ Readln(input1,Ei);}
  Io:=4*0.85*Ei/(PI*SQR(PI)*SQR(Ro)*(1.5*t0+0.5*t1));
  writeln(Io);
  N01:=0;
  For M:=0 To 3*S2 Do
    Begin
      N[M,0]:=N01;
    End;
  For Q1:=1 To 3*S1+1 Do
    Begin {r1}
    { If r1=0 Then

```

```

Begin
  P:=1;
End
Else
Begin
  Theta:=0;
  For Q3:=1 To 3*S3+1 Do
    Begin
      F[7,Q3]:=(1/PI)*cos(Theta - Y3*r1*sin(theta));
      Theta:=theta+h3;
    End;
  L2:=7;
  S11:=S3;
  h11:=h3;
  SIMPSON;
  P:=SQR(2*Int[7]/(Y3*r1));
End;
  Writeln(-r1:5,' ',r1:5,' ',P:15);}
t:=-0.6;
N01:=0;
For J:=1 TO 3*So+1 Do
Begin {TIME}
  P:=Exp(-2*SQR(r1/ro));
  I01:=(1-Ref1)*P*Io*Exp(-(Sqr(t/t0)));
  I02:=P*Io*Exp(-(Sqr((t+h/4)/t0)));
  I03:=P*Io*Exp(-(Sqr((t+3*h/8)/t0)));
  I04:=P*Io*Exp(-(Sqr((t+12*h/13)/t0)));
  I05:=P*Io*Exp(-(Sqr((t+h)/t0)));
  I06:=P*Io*Exp(-(Sqr((t+h/2)/t0)));
If t>=0 Then
Begin
  I01:=0.5*(I01+(p*Io*(1-Ref1)*Exp(-SQR(t/t1))));
  I02:=0.5*(I02+(P*Io*Exp(-SQR((t+h/4)/t1))));
  I03:=0.5*(I03+(P*Io*Exp(-SQR((t+3*h/8)/t1))));
  I04:=0.5*(I04+(P*Io*Exp(-SQR((t+12*h/13)/t1))));
  I05:=0.5*(I05+(P*Io*Exp(-SQR((t+h)/t1))));
  I06:=0.5*(I06+(P*Io*Exp(-SQR((t+h/2)/t1))));
End;
  RUNGE_KUTTA_F;
  N[1,J]:=N0;
  F[4,1]:=N[1,J];
  F[5,1]:=I01;

```

(\*\*\*\*\*)

```

For M:=1 To 3*S2 Do
  Begin {REGION}
    P1:=A+S*N[M,J-1];
    X1:=Exp(-(P1*L));
    Y1:=1 - X1;
    Z1:=B*Y1/P1;
    I11:=(X1*I01)/(1+Z1*I01);
    F[5,M]:=I11;
    I12:=(X1*I02)/(1+Z1*I02);
    I13:=(X1*I03)/(1+Z1*I03);
    I14:=(X1*I04)/(1+Z1*I04);
    I15:=(X1*I05)/(1+Z1*I05);
    I16:=(X1*I06)/(1+Z1*I06);
    I01:=I11;
    I02:=I12;
    I03:=I13;
    I04:=I14;
    I05:=I15;
    I06:=I16;
    N01:=N[M+1,J-1];
    RUNGE_KUTTA_F;
    N[M+1,J]:=N0;
    F[4,M+1]:=N[M+1,J];
  END; {REGION}
For L2:=4 To 4 Do
  Begin
    S11:=S2;
    h11:=L;
    SIMPSON;
  End;
  Fen:=(4*Ref1)/SQR(1-Ref1);
  ph[Q1,J]:=A2*Int[4] + A4*Int[5] + (2*PI/(Lam*35))*SQR(r1);
  Iout[Q1,J]:=(1-Ref2)*I11;{/((1+Fen*SQR(Sin(ph[Q1,J]/2)))};}
  F[6,J]:=I11;
  N01:=N[1,J];
{  WRITELN(output2,r1:5,' ',t:5,' ',cha_ph[Q1,J]:13);}
  t:=t + h;
End; {TIME}
{ Writeln(r1:5,' ',Iout[Q1,225]:13);}
{ S11:=So;
h11:=h*1E-10;
L2:=6;
SIMPSON;
Writeln(output2,r1:5,' ',Int[6]/(12E-9):13);}
r1:=r1 + h1;

```

End; {r1}

(\*\*\*\*\*)

```

r:=0;           {Spatial}
h2:=0.0015;
For Q:=1 To 50 Do
  Begin {r}
    For J:=1 To 3*So+1 Do
      Begin {TIME}
        r1:=0;
        For Q1:=1 To 3*S1+1 Do
          Begin {r1}
            X:=-A1*SQR(r1) - ph[Q1,J];
            Bessel;
            Z2:=Jo*r1*SQR(T(Iout[Q1,J]));
            F[1,Q1]:=Z2*COS(X);
            F[2,Q1]:=Z2*SIN(X);
            r1:=r1 + h1;
          End; {r1}
        For L2:=1 To 2 Do
          Begin
            h11:=h1;
            S11:=S1;
            SIMPSON;
          End;
          Y:=A1*SQR(r);
          Ere:=SIN(Y)*Int[1] - COS(Y)*Int[2];
          Eim:=SIN(Y)*Int[2] + COS(Y)*Int[1];
          F[3,J]:=(SQR(Ere) + SQR(Eim))*SQR(B1);
        End; {TIME}
      L2:=3;
      h11:=h*1E-10;
      S11:=So;
      SIMPSON;
      Isp:=Int[3]*(Eo*Co)/(2*Tp);
      Writeln(-1*r:5, ' ',r:11, ', ',Isp:13);
      r:=r + h2;
    End;
  End;

```

(\*\*\*\*\*)

```

(* r1:=0;           {Temporal}
t:=-2;
For J:=1 To 40 Do
  Begin
    for Q1:=1 to 40 do

```

```

begin
  F[7,Q1]:=2*PI*r1*Iout[Q1,J];
  r1:=r1+h1;
end;
L2:=7;
S11:=s1;
h11:=h1;
Simpson;
writeln(output1,Int[7]:13);
t:=t + h;
End;*)

t:=-2;
h2:=0.0050/60;
For J:=1 To 3*So+1 Do
  Begin {time}
    r:=0;
    For Q:=1 To 61 Do
      Begin {R}
        r1:=0;
        For Q1:=1 To 3*S1+1 Do
          Begin {r1}
            X:=-A1*SQR(r1) - ph[Q1,J];{1---->Q1}
            Bessel;
            Z2:=Jo*r1*SQR(Iout[Q1,J]);{1-->Q1}
            F[1,Q1]:=Z2*COS(X);
            F[2,Q1]:=Z2*SIN(X);
            r1:=r1 + h1;
          End; {r1}
        For L2:=1 To 2 Do
          Begin
            h11:=h1;
            S11:=S1;
            SIMPSON;
          End;
          Y:=A1*SQR(r);
          Ere:=SIN(Y)*Int[1] - COS(Y)*Int[2];
          Eim:=SIN(Y)*Int[2] + COS(Y)*Int[1];
          F[3,Q]:=(SQR(Ere) + SQR(Eim))*r*SQR(B1);
          {Writeln(r:13,' ',t*10:13,' ',F[3,Q]*(Eo*Co*0.5):13);}
          r:=r + h2;
        End; {R}
      End;
    L2:=3;
    h11:=h2;
    S11:=20;
  End;

```

```
SIMPSON;  
Itp:=Int[3]*(Eo*Co)/(SQR(0.005));  
Writeln(t*10:11,',',Itp:13);  
t:=t + h;  
End;  
{ End;}{file}  
End.
```

## APPENDIX E

### PROGRAM FOR THE THEORY IN CHAPTER III

```
PROGRAM Fab (INPUT,OUTPUT);
  (*****)
  (*This program calculates the output of a Fabry-Perot Etalon assuming the two-photon*)
  (* absorption and the generation of the free carriers took place during the first pass *)
  (*                                     through the sample.                                     *)
  (*                                     This Program is written in Pascal                               *)
  (*****)
CONST
  Y5=0;
  NG=2;
  D=2.6781E+24;      {10^6/2hv}
  D1=0.136;{0.13562065;}
  {angle=1.3;}
  Ei=2.3;
  t0=0.5;
  t1=0.8;
  No=2.84;
  Co=2.99E+10;
  Eo=8.8542E-16;
  N2=-20E-11;
  Sr=-6E-21;
  PI=3.1415927;
  Ro=0.0215;
  So=50;
  Tp=10E-9;
  Ne=4.3E+15;
  Cr=0;{5E-11;}
  C=8.3E+7;
  A=0.3;
  B=0.022;
  S=25E-18;
  Diff=0.06;
  Lam=1.064E-4;
  Ref1=0.23;
  Ref2=0.025;
```



VAR

N:Array[0..40,0..220] OF Real;  
 { ph:Array [0..40,0..200] OF Real;}  
 Int: Array [1..7] OF Real;  
 F:Array [1..7,0..220] OF real;  
 N0,N01,I01,I02,I03,I04,I05,I06,  
 I11,I12,I13,I14,I15,I16,SUM, THICK,  
 P1,X1,Z1,Y1,L,h,h11,t,r1,r,A2,A4,  
 h1,h2,h3,Z2,E,X,P,It,Fap,Alpha\_eff,Fen,  
 GAMA,CHA\_INDEX,Io,Y,Iin,Imax,Ae,Xe,R2,De,Dee,  
 Nav,wi,t2,Navr,ph,Fr,Ff,Fi,Angle:Real;  
 J,M,Q,Q1,Q3,L2,S1,S2,S11,S3,I1,K9:Integer;        {LOOP CONTROL VARIABLES}  
 output1:text;

Procedure RUNGE\_KUTTA\_F ;

VAR

K1,K2,K3,K4,K5,K6,G2,G3,G4,G5,G6:Real;

Begin

K1:= h \* (B \* D \* Sqr(I01) - C \* (N01 - Ne)- Cr \* (SQR(N01) +  
 N01\*Ne))\*1E-8;  
 G2:= K1/4;  
 K2:= h\*(B\*D\*Sqr(I02) - C\*(N01+G2- Ne)-Cr\*(SQR(N01+G2)+  
 (N01+G2)\*Ne))\*1E-8;  
 G3:= 3\*K1/32 + 9\*K2/32;  
 K3:= h\*(B\*D\*Sqr(I03) - C\*(N01+G3- Ne)-Cr\*(SQR(N01+G3)+  
 (N01+G3)\*Ne))\*1E-8;  
 G4:= 1932\*K1/2197-7200\*K2/2197+7296\*K3/2197;  
 K4:= h\*(B\*D\*Sqr(I04) - C\*(N01+G4- Ne)-Cr\*(SQR(N01+G4)+  
 (N01+G4)\*Ne))\*1E-8;  
 G5:= 439\*K1/216-8\*K2+3680\*K3/513-845\*K4/4104;  
 K5:= h\*(B\*D\*Sqr(I05) - C\*(N01+G5- Ne)-Cr\*(SQR(N01+G5)+  
 (N01+G5)\*Ne))\*1E-8;  
 G6:= 2\*K2-8\*K1/27-3544\*K3/2565+1859\*K4/4104-11\*K5/40;  
 K6:= h\*(B\*D\*Sqr(I06) - C\*(N01+G6- Ne)-Cr\*(SQR(N01+G6)+  
 (N01+G6)\*Ne))\*1E-8;  
 N0:= N01+16\*K1/135 + 6656\*K3/12825 + 28561\*K4/56430.0 -  
 9\*K5/50 + 2\*K6/55;

End;

PROCEDURE SIMPSON;

VAR

G:Real;

L1,U:Integer;

G1:Array [1..300] OF Real;

```

Begin
  G1[1]:=F[L2,1] + 3*F[L2,2] + 3*F[L2,3];
  L1:=3;
  For U:=2 To S11 Do
    Begin
      G1[U]:=2*F[L2,L1+1] + 3*F[L2,L1+2] + 3*F[L2,L1+3];
      L1:=L1 + 3;
    End;
  G:=0;
  For U:=1 To S11 Do
    Begin
      G:=G + G1[u];
    End;
  Int[L2]:=(3*h11/8)*(G + F[L2,3*S11+1]);
End;

Begin {Main}
  Assign(output1,'cd.dat');
  Rewrite(output1);
  Angle:=0;
  Io:=30;
  For K9:=1 To 1 do
    Begin

      {Dee:=2*PI*D1*SQRT(SQR(No)-SQR(Sin(PI*angle/180)))/Lam;
      De:=arctan(sin(Dee)/cos(Dee));
      writeln(De/PI); }
      { De:=0.23*PI; }

      t:=-2;
      S1:=26;
      S2:=13;      (*****<<<<<<<-----*****
      S3:=25;
      r1:=0.0;
      h:=4/(3*So);
      h1:=Diff(3*S1);
      h3:=PI/(3*S3);
      L:=D1/(3*S2);
      A2:=(2*PI*Sr)/Lam;
      GAMA:=4000*PI*N2/(Co*No);
      A4:=80*PI*PI*N2/(Co*No*1E-2*Lam);
      { Io:=4E-2*0.85*Ei/(PI*SQRT(PI)*SQR(ro)*((1+(1/NG))*t0+(1-(1/NG))*t1));
      Io:=15.4;
      writeln(Io);}
    End;
  End;

```

```

N01:=0.0;

For M:=0 To 3*S2 Do
  Begin
    N[M,0]:=N01;
  End;
For Q1:=1 To 1 do{3*S1+1 Do}
  Begin {r1}
    t:=-2;
    N01:=0;
    For J:=1 TO 3*So+1 Do
      Begin {TIME}
        P:=Exp(-2*SQR(r1/ro));
        I01:=(1-Ref1)*P*Io*Exp(-(Sqr(t/t0)));
        Iin:=I01;
        I02:=P*Io*Exp(-(Sqr((t+h/4)/t0)));
        I03:=P*Io*Exp(-(Sqr((t+3*h/8)/t0)));
        I04:=P*Io*Exp(-(Sqr((t+12*h/13)/t0)));
        I05:=P*Io*Exp(-(Sqr((t+h)/t0)));
        I06:=P*Io*Exp(-(Sqr((t+h/2)/t0)));
      If t>0 Then
        Begin
          I01:=(1/NG)*(I01+(NG-1)*(P*Io*(1-Ref1)*Exp(-SQR(t/t1))));
          Iin:=I01;
          I02:=(1/NG)*(I02+(NG-1)*(P*Io*Exp(-SQR((t+h/4)/t1))));
          I03:=(1/NG)*(I03+(NG-1)*(P*Io*Exp(-SQR((t+3*h/8)/t1))));
          I04:=(1/NG)*(I04+(NG-1)*(P*Io*Exp(-SQR((t+12*h/13)/t1))));
          I05:=(1/NG)*(I05+(NG-1)*(P*Io*Exp(-SQR((t+h)/t1))));
          I06:=(1/NG)*(I06+(NG-1)*(P*Io*Exp(-SQR((t+h/2)/t1))));
        End;
        RUNGE_KUTTA_F;
        N[1,J]:=N0;
        F[4,1]:=N[1,J];
        F[5,1]:=I01;
        {Writeln(F[5,1]);}
      End;
    End;
  End;

```

(\*\*\*\*\*)

```

For M:=1 To 3*S2 Do
  Begin {REGION}
    P1:=A+S*N[M,J-1];
    X1:=Exp(-(P1*L));
    Y1:=1 - X1;
    Z1:=B*Y1/P1;
    I11:=(X1*I01)/(1+Z1*I01);
    F[5,M+1]:=I11;
  End;

```

```

I12:=(X1*I02)/(1+Z1*I02);
I13:=(X1*I03)/(1+Z1*I03);
I14:=(X1*I04)/(1+Z1*I04);
I15:=(X1*I05)/(1+Z1*I05);
I16:=(X1*I06)/(1+Z1*I06);
I01:=I11;
I02:=I12;
I03:=I13;
I04:=I14;
I05:=I15;
I06:=I16;
N01:=N[M+1,J-1];
RUNGE_KUTTA_F;
N[M+1,J]:=N0;
F[4,M+1]:=N[M+1,J];
{F[7,M+1]:=SQR(F[5,M+1]);}
END; {REGION}
For L2:=4 To 5 Do
Begin
S11:=S2;
h11:=L;
SIMPSON;
End;
{ph:=A2*Int[4] + A4*Int[5]+De;}
{ Iout[Q1,J]=(1-Ref2)*I11;}
Nav:=Int[4]/D1;
ph:=2*PI*D1*SQR(SQR(No+(Sr*Nav))-SQR(Sin(PI*angle/180)))/Lam;
R2:=SQR(Ref1*Ref2)*Exp(-(A+S*Nav)*D1);
Ae:=1/SQR(1-R2);
Fr:=(PI*SQR(R2))/(1-R2);
Ff:=1;
Fi:=(Fr*Ff)/SQR(SQR(Ff)+SQR(Fr));
Fen:=(4/SQR(PI))*SQR(Fi);
Fap:=Ae/(1+Fen*SQR(Sin(ph)));
It:=(1-Ref2)*I11*Fap;
CHA_INDEX:=GAMA*Int[5]/D1+Sr*Nav;
Alpha_eff:=B*Int[5]/D1+S*Nav;
F[6,J]:=I11;
N01:=N[1,J];
Wi:=A2*(B*D*Int[5]-c*Int[4]);{when do this we should have SQR(F[5,j])}
{ If j=76 then
Begin}
WRITELN(output1,t*10,' ',F[4,1]:15);
{ end;}
t:=t + h;

```

```
End; {TIME}  
{ WRITELN(output1,r1:10,' ',It/lin:13,' ',Nav:13);}  
r1:=r1 + h1;  
End; {r1}  
Io:=Io+2;  
End;  
Close(output1);  
END.
```

## APPENDIX F

### PROGRAM FOR THE THEORY IN CHAPTER IV

```

PROGRAM Efficiency_Grating (INPUT,OUTPUT);
(*****)
(* This program calculates the Scattering Efficiency of a Gaussian beam from a volume *)
  (* grating formed by two Crossed Gaussian Beams. *)
  (* This Program is written in Pascal *)
(*****)

CONST
  Thickness=0.1;           { Sample thickness in cm }
  We=0.01;                 { Waist Of The Write-Beam }
  Wp=0.01;                 { Waist Of The Read-Beam }
  Lam_e=465.8E-7;         { Wavelength Of The Write-Beam }
  Lam_p=465.8E-7;         { Wavelength Of The Read-Beam }
  Th_e=2;                  { Half The Crossing Angle In Air }
  Ne=1.57;                 { Index Of Refraction For Lam_e }
  Np=1.57;                 { Index Of Refraction For Lam_p }
  Alpha_p=0.0;            { Absorption coefficient of the probe beam }
  Alpha_e=0.0;            { Absorption coefficient of the pump beam }
  Si=15;                   { Number of panels in the y-direction }
  Sj=30;                   { Number of panels in the x-direction }
  Sk=100;                  { Number of panels in the z-direction }

VAR
  Int: Array [1..10] OF Extended;
  F:Array [1..10,1..600] OF Extended;
  {I_S:Array [1..100,1..100] OF Real;}
  eff,Ke,Kp,Th_p,A,A1,A2,A3,B,B1,B2,C,C1,D,h,h1,
  h_z,h_x1,h_y,Le,Lp,S,S1,S2,S3,S4,S5,S6,S10,Te,Tp,X,X1,Y,Z,Z1,Alpha:Extended;
  I,J,K,M,L2,S11:Integer;
  Output1:text;

(*****)
PROCEDURE SIMPSON; {This procedure uses Simpson 3/8 rule to calculate Integrals}
VAR
  G:Real;

```

```

L1,U:Integer;
G1:Array [1..1200] OF Extended;
Begin
  G1[1]:=F[L2,1] + 3*F[L2,2] + 3*F[L2,3];
  L1:=3;
  For U:=2 To S11 Do
    Begin
      G1[U]:=2*F[L2,L1+1] + 3*F[L2,L1+2] + 3*F[L2,L1+3];
      L1:=L1 + 3;
    End;
  G:=0;
  For U:=1 To S11 Do
    Begin
      G:=G + G1[u];
    End;
  Int[L2]:=(3*h11/8)*(G + F[L2,3*S11+1]);
End;
(*****)

Begin {Main}
  Assign(output1,'cd.dat');
  Rewrite(output1);
  Alpha:=Alpha_e;
  S6:=Alpha_e + (Alpha_p/2);
  Z1:=(Thickness/2)+0.0000000001;
  Le:=Lam_e/Ne;
  Lp:=Lam_p/Np;
  Te:=Th_e*PI/(Ne*180);
  Tp:=Te*(Lp/Le);
  {writeln(Tp);}
  Ke:=2*PI/Le;
  Kp:=2*PI/Lp;
  A:=(2/SQR(We)) + (1/SQR(Wp));
  C1:=2*Ke*Te - Kp*Tp;
  S:=(2*SQR(Te)/SQR(We)) + (SQR(Tp)/SQR(Wp));
  S3:=0.5*Kp*SQR(Tp);
  h_z:=Thickness/(3*Sk);
  h_x1:=2*(1.2*Wp)/(3*Sj);
  h_y:=2*(1.2*Wp)/(3*Si);
  Y:=-1.2*Wp;
  For I:=1 To 3*Si+1 Do
    Begin {LOOP OVER Y}
      X1:=-1.2*Wp;
      For J:=1 To 3*Sj+1 Do
        Begin {LOOP OVER X}

```

```

X:=(X1-Z1*Tp)/(1-0.5*SQR(Tp));
Z:=-Thickness/2;
For K:=1 To 3*Sk+1 Do
  Begin {LOOP OVER Z}
    B:=PI/(Lp*(Z-Z1));
    A1:=SQR(A) + SQR(B);
    A2:=SQR(B)*A*SQR(Y)/A1;
    A3:=SQR(A)*B*SQR(Y)/A1;
    D:=(2*Tp*Z/SQR(Wp))-(0.5*Tp*Alpha_p);
    C:=C1 - 2*B*X;
    B1:=(B*SQR(X))+(2*A*C*D+B*(SQR(D)-SQR(C)))/(4*A1);
    B2:=(A*(SQR(D)-SQR(C)) - (2*B*C*D))/(4*A1);
    S4:=B1+A3+S3*Z;
    IF Z > (We/Te) Then {To ignore the pump beam absorption if the sample}
      Begin {thickness is larger than that of the grating}
        Alpha:=0;
      End;
    S1:=(0.5*Alpha*(2-SQR(Te))) + (0.25*Alpha_p*(2-SQR(Tp)));
    S5:=B2-A2-S*SQR(Z)-S1*Z;
    F[1,K]:=(A*Cos(S4) - B*Sin(S4))*(Exp(S5)/A1)*(1/(Z-Z1));
    F[2,K]:=(B*Cos(S4) + A*Sin(S4))*(Exp(S5)/A1)*(1/(Z-Z1));
    { Writeln(output1,Z:13,' ',F[2,k]:20);}
    Z:=Z+h_z;
  End; {LOOP OVER Z}
  (*****

For L2:=1 To 2 Do {Start integration over z}
  Begin
    h11:=h_z;
    S11:=Sk;
    SIMPSON;
  END;
  F[3,J]:=(SQR(Int[1]) + SQR(Int[2]));
  Writeln(output1,Y:13,' ',X1:13,' ',F[3,J]:20);
  X1:=X1 + h_x1;
END; {LOOP OVER X}
(*****

L2:=3; {Start integration over x}
h11:=h_x1;
S11:=Sj;
SIMPSON;
F[4,I]:=Int[3];
writeln(output1,Y:13,' ',Int[3]:19);}
Y:=Y + h_y;

```



```
END; {LOOP OVER Y}
(*****)
  L2:=4;           {Start integration over y}
  h11:=h_y;
  S11:=Si;
  SIMPSON;
  S10:=2*SQR(Lam_p)*SQR(Lam_p*Np*Wp);
  Eff:=(PI*SQR(PI)*2*Int[4]*Exp(-S6*Thickness))/S10;
  writeln('The eff/SQR(index-change) is----> ',Eff:19);
  Close(output1);

END.
```

2

VITA

ABDULLATIF Y. HAMAD

Candidate for the Degree of

Doctor of Philosophy

Thesis: NONLINEAR OPTICAL PROPERTIES OF CdTe AND LASER INDUCED GRATING IN  $\text{Eu}^{3+}$  -DOPED SILICATE GLASSES

Major Field: Physics

Biographical:

Personal data: Born in Bazaryah/Nablus, West Bank, February 20 1966, the son of Yousef and Fayzah Hamad.

Education: Received Bachelor of science Degree in Physics/Math-minor from Oklahoma State University, Stillwater, Oklahoma, in May 1990; completed the requirements for the Doctor of Philosophy Degree at Oklahoma State University, Stillwater, Oklahoma, in July 1996.